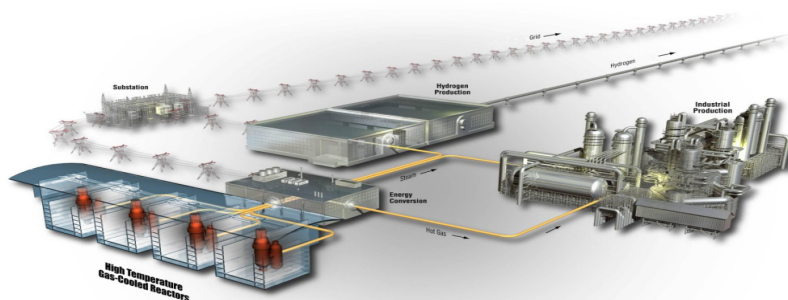# Experimental and Analytic Study on the Core Bypass Flow in a Very High Temperature Reactor

R. R. Schultz
M-H. Kim
R. Vilim
C. G. Park
Y. Hassan

April 2012

Idaho National
Laboratory

Experimental and Analytic Study on the Core Bypass Flow in a Very High Temperature Reactor

R. R. Schultz
M-H. Kim[1]
R. Vilim[2]
C. G. Park [3]
Y. Hassan[4]

[1]**KAERI**
[2]**ANL**
[3]**SNU**
[4]**TAMU**

April 2012

Idaho National Laboratory
Next Generation Nuclear Plant Project
Idaho Falls, Idaho 83415
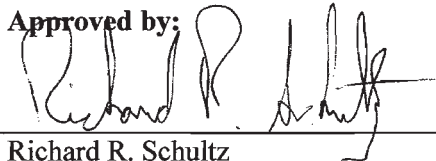
http://www.inl.gov

Next Generation Nuclear Plant Project

Experimental and Analytic Study on the Core Bypass Flow in a Very High Temperature Reactor

INL/EXT-12-24603
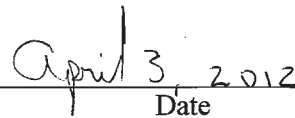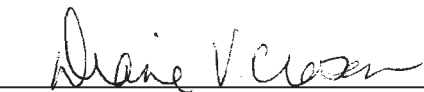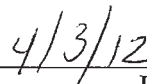
April 2012

Approved by:

_____
Richard R. Schultz
INL Principle Investigator

April 3, 2012
_____
Date

_____
Diane Croson
VHTD TDO Deputy Director

4/3/12
_____
Date

SUMMARY

Core bypass flow has been one of key issues in the very high temperature reactor (VHTR) design for securing core thermal margins and achieving target temperatures at the core exit. The bypass flow in a prismatic VHTR core occurs through the control element holes and the radial and axial gaps between the graphite blocks for manufacturing and refueling tolerances. These gaps vary with the core life cycles because of the irradiation swelling/shrinkage characteristic of the graphite blocks such as fuel and reflector blocks, which are main components of a core's structure. Thus, the core bypass flow occurs in a complicated multidimensional way. The accurate prediction of this bypass flow and counter-measures to minimize it are thus of major importance in assuring core thermal margins and securing higher core efficiency. Even with this importance, there has not been much effort in quantifying and accurately modeling the effect of the core bypass flow.

The main objectives of this project were to generate experimental data for validating the software to be used to calculate the bypass flow in a prismatic VHTR core, validate thermofluid analysis tools and their model improvements, and identify and assess measures for reducing the bypass flow. To achieve these objectives, tasks were defined to (1) design and construct experiments to generate validation data for software analysis tools, (2) determine the experimental conditions and define the measurement requirements and techniques, (3) generate and analyze the experimental data, (4) validate and improve the thermofluid analysis tools, and (5) identify measures to control the bypass flow and assess its performance in the experiment.

Design and construction of experimental facilities: The experimental designs, which consist of the air test led by the Korean Atomic Energy Institute (KAERI) at Seoul National University (SNU) and the matched-index-of-refraction (MIR) and air tests led by Idaho National Laboratory (INL) at Texas A&M University (TAMU), were completed in FY 2008. The air tests use air as a working fluid to obtain data for the validation of core thermofluid analysis codes; the MIR experiments are designed to produce data for the validation of computational fluid dynamics (CFD) codes. Based on the experimental designs, the construction of the multiblock air test facility and the MIR test facility were completed in FY 2009. A considerable portion of the experimental design efforts were directed at precisely controlling the bypass gap sizes and also the laser diagnostics designed to produce the validation data.

Determination of experimental conditions and development of measurement techniques: A methodology for estimating gap size distribution in the prismatic cores was developed by KAERI in FY 2008 and applied to a reference prismatic core. The results were used in selecting the gap size and distribution in the test matrix. The influence of core restraint mechanism and replacement of side reflector on bypass gap distribution and hot spot fuel temperature was investigated in FY 2010.

Preliminary analyses of the SNU air test facility were performed by KAERI to investigate major phenomena in the bypass flow by using GAMMA+ code and CFD code as well. Major findings are: (i) high dependence of bypass flow on the gap size, (ii) increase of bypass flow by the presence of reflector blocks, (iii) little effect of cross-flow gap change on the bypass flow distribution, (iv) local variant bypass flow by non-uniform gap distribution, and (v) nearly uniform flow distribution at each block column outlet.

Pretest calculations were performed to evaluate the anticipated behavior of both the INL and TAMU MIR experiments and to identify the diagnostic instrumentation measurement protocol. These CFD calculations indicate that: the bypass gap flow prefers to proceed down the vertex region of the bypass, since this region has the least frictional resistance to flow; minimal gap widths lead to laminar flow in the gap and cross-flow regions, whereas larger bypass gaps lead to either transition or turbulent flow; and the bypass region clearly has larger frictional resistance than the cooling channels.

The SNU air test designed a special concept of test block to install a total of 448 pressure taps in the test section for measuring static pressure of coolant holes within the fuel block and bypass gaps of the

block periphery. A guide pipe was introduced to secure the space for connection of the pressure tubes from the pressure taps to the pressure transmitters. The bypass flow rate was determined indirectly by subtracting the flow rate at the outlet from that at the inlet; both were measured by flow-meter using average pitot tubes.

Testing and Interpretation of Experimental Data: The air test was performed for both uniform and nonuniform gap distributions. The uniform gap test was useful for the investigation of bypass flow itself while the nonuniform one was for a detailed survey of the influence of cross flow on bypass flow. The bypass gap size was measured at the top of each block layer after installation to provide test data with detailed gap distribution. The measured data were interpreted by comparing them with the results of CFD calculations, which showed that the data is valid enough to be used as the benchmark data for the core thermofluid analysis code.

Even though the INL MIR experiment encountered considerable alignment difficulties, it produced a reference data set consisting stereo particle image velocimeter images along the coolant channel centerlines of three coolant channels at the downstream location at the midlevel Reynolds number flow rate. The ongoing INL MIR experiments are scheduled to produce the first data set by to the end of 2011, which will then be available to KAERI for numeric model validation.

Because of the corrosive nature of p-cymene (the working fluid), the TAMU MIR experiment was terminated and the experimental effort modified to use air as the working fluid. A series of 36 data sets were recorded with bypass gap widths of 6.1, 4.66, and 3.21 mm. These data will be used for future validation studies.

Validation and Improvement of Thermofluid Analysis Tools: Benchmark calculations were performed through all fiscal years to investigate the performance of the system codes GAMMA+ and GAS-NET and of CFD codes. Based on the results, code and model improvement has been accomplished.

Code-to-code comparison between GAMMA+ and CFD codes for a simple multiblock experiment showed deficiency of the GAMMA+ model, suggesting that a blockage effect at the region where cross and bypass flows merge be considered in the model for more accurate prediction of bypass flow. A correlation of Y-type cross junction was introduced in the GAMMA+ code, improving the results of pressure drop and bypass flow predictions. The multichannel model was also improved by adding 2-D (2-D) advection term and viscous term into both the normal junction momentum for axial flow and the cross junction momentum for lateral flow in bypass gaps.

The channel loss correlation in GAS-NET was extended from a single Blasius-type model for all channels to a model specific to each of the four channel types and at each block level. The channel types are block coolant hole, axial flow in intercolumn gap, lateral flow in intercolumn gap, and lateral leakage flow between two stacked blocks. A fit of the Darcy friction factor to the Zigrang-Sylvetser correlation at a given surface roughness can be selected for each of these channels and at each axial level. Additional heat transfer capability was also added to the GAS-NET code to accommodate (a) fueled blocks where the dominant heat transfer phenomena are internal heat generation and conduction of this heat to the block outer surface, and (b) nonfueled blocks where the dominant phenomenon is conduction of heat through the block in the radial direction.

Validation studies were performed on the GAS-NET code to examine the fluid flow and heat transfer models. The first study compared code predictions of bypass flow rates with data for an isothermal experiment performed in the Multi-Block Air Test Facility at SNU. An important phenomenon in this experiment was stacked-block-gap leakage driven by axial pressure gradients related to bypass gap size that varied by block axial elevation. The second study compared GAS-NET code predictions with RELAP results for temperatures in the MHTGR core at full power conditions.

Blind benchmark calculations for the MIR test were carried out by both KAERI and INL to investigate the ability of their CFD codes to predict the bypass flow prediction. The results were

compared in detail for pressure drop across the model, velocity profiles in the coolant channel, flow and pressure distribution at the upper plenum, and cross-flow gap. Although different turbulence and a wall treatment model were used, both results predicted similar bypass flow fractions. A little difference in total pressure drop and flow distribution in the cross-flow gap was observed, so the mean and turbulent data set obtained from the MIR test will be useful in clarifying this difference.

Identification of bypass flow reduction measures and their performance test: Three measures were identified to reduce the bypass flow. Based a literature survey, seal elements on the bottom core blocks were considered the first measure. Staggering the arrangement of two transition blocks to make the bypass flow from the upper transition blocks blocked by the top surface of the second transition blocks is the second measure. Grooved reflector blocks to increase the flow resistance and reduce the bypass flow is the third measure.

These identified measures were realized by designing and modifying the air test section. The seal elements were modeled by simply blocking the entire bypass gap at the bottom. For the staggered arrangement of transition blocks, 3-D CAD models were developed to verify that the blocks could be arranged in a zigzag pattern while maintaining coolant flow path. The grooved reflector was designed, which required optimizing the shape of groove to maximize the flow resistance and at the same time maintain manufacturability.

These counter-measures were carried out in the Air Test Facility. The staggered transition blocks performed equivalent to the seal elements by blocking and directing most of the bypass flow into the coolant channels. The grooved reflectors also showed good performance, reducing the bypass flow from 22 to 14% at the exit.

CONTENTS

FIGURES

xiv

TABLES

ACRONYMS

ANL	Argonne National Laboratory
BG	bypass gap
BOC	beginning of cycle
CF	cross-flow gap
CFD	computational fluid dynamics
CR	control rod
CRM	core restraint mechanism
CTE	coefficient of thermal expansion
EC	equilibration core
EOC	end of cycle
HF	high flow
GA	General Atomics
IC	initial core
INL	Idaho National Laboratory
KAERI	Korean Atomic Energy Research Institute
LF	low flow
MHTGR	Modular High-Temperature Gas-cooled Reactor
MIR	matched index of refraction
NTP	normal temperature and pressure
PMR	prismatic modular reactor
R&D	research and development
ROK	Republic of Korea
RSC	reserve shutdown coolant
SNL	Seoul National University
TAMU	Texas A&M University
TRISO	tristructural isotropic
VHTR	very high temperature reactor
XLF	extra low flow

Experimental and Analytic Study on the Core Bypass Flow in a Very High Temperature Reactor

1. PROJECT ORGANIZATION

Idaho National Laboratory (INL) led the project for the United States and the Korea Atomic Energy Research Institute (KAERI) on the Republic of Korea (ROK) side. Argonne National Laboratory (ANL), Texas A&M University (TAMU), and Seoul National University (SNU) were partners in the research and development (R&D) collaboration. This collaboration exploited unique capabilities and resources available at these organizations to achieve the objectives of the proposed project as shown in the project organizational chart below.

INL tasks focused on the experiments of the scaled model built in the matched-index-of-refraction (MIR) test section and computing the computational fluid dynamics (CFD) for validating and improving the model. ANL tasks focused on the validating and improving the GAS-NET network code for the integrated system-level analysis of the bypass flow margins in the prismatic modular reactor (PMR) designs. TAMU was originally tasked to construct a small MIR model for a section resembling the bypass flow through various gap configurations of the block elements. However it was changed to use air as working fluid after encountering difficulties with toxic working fluids. KAERI tasks focused on coordinating and supporting the activity of the air test in parallel with CFD computation for validating and developing the model for the GAMMA+ system analysis code. SNU tasks focused on the multiblock air test to generate data for assessing the system-level codes and improving their models. The test for the bypass flow reduction measure was also carried out at SNU in support of U.S. efforts.
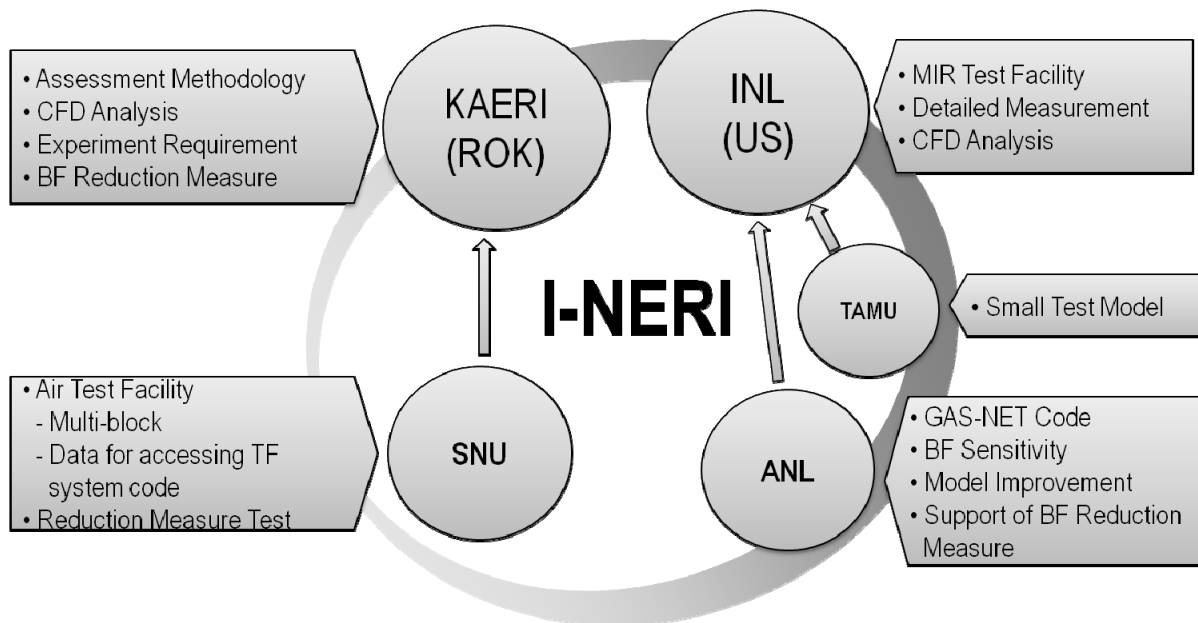
Figure 1-1. Project organization.

2. TASK 1

1. Task title and responsible lead:

   Design and Construction of Experimental Facility, KAERI/INL.

2. Brief description of objectives:

   Design and construct bypass flow models and facilities to provide data for assessing the thermal-fluid analysis tools. Construct the experimental facilities for the air test led by KAERI/SNU and for the MIR tests led by INL and located both at INL and TAMU.

3. Task technical status overview

2.1 Construction of Multiblock Air Test Facility (SNU/KAERI)

The Multiblock Air Test Facility is designed to obtain the experimental data for assessing the thermal-fluid analysis tools such as GAMMA+ and GAS-NET by measuring the flow rate of fuel block columns and the local pressure distribution. Experimental parameters to be measured in the multiblock air test facility are the flow rates at the inlet and outlet of the block columns and the local static pressure in coolant holes and bypass gaps.

The design of the experimental facility was based on the PMR200 developed by KAERI. The facility was open-loop system, and the working fluid was air at normal temperature and pressure (NTP). Figures 1-1 and 1-2 show the experimental facility, which has an overall height of 5.4 m. The facility was comprised of a flow supply system, test section (including test blocks), and flow measuring system consisting of average pitot-tube flow-meters and differential pressure transmitters. The test section included the core and lower plenum. The test block was divided into fuel and reflector types. The core part of the test section consisted of seven block columns by four blocks high, forming a honeycomb shaped cross-section. Block layers were divided into the active core and transition regions. The lowest two block layers were included in the transition region where the installed transition blocks served to not only support the core blocks but also to gather the flow from coolant holes into a single channel to measure the outlet flow rate of the block column. As shown in Figure 1-2, the pipe for measuring the flow rate is attached to the top core block and the bottom transition block. This pipe is 0.4 m in diameter and 1.0 m long. Sixteen static pressure taps were axially installed on a side of the test section to measure the static pressure distribution in the bypass gap. Since the pressure variation across the cross-flow gap was expected to be large, three static pressure taps near the gap were installed to measure the pressure distribution in detail. Since the pressure distribution in the fuel side and the reflector side bypass gap was different from each other in the fuel-reflector block combination, the pressure taps were installed on the opposite side of the test section to measure the local pressure distribution in the outside bypass gap as shown in Figure 1-2. Thus, a total of 32 static pressure taps are installed on the side of the test section.

Figure 2-3 shows pictures of manufactured test blocks of acryl. In order to manufacture the fuel block, acrylic pipes were installed inside hollow hexagonal blocks instead of drilling holes in compacted block. The upper and lower sides of the transition block were matched up with fuel block and lower plenum block, respectively. Pressure tubes of core block moved downward through the guide pipe. When the pressure tubes were reached the lower plenum block, those were extended to the lower plenum block and were connected to the pressure tube connector. Bypass gap size was controlled by the wall thickness of the gap control block. As the fuel block was combined with the gap control block, the flat-to-flat width of the block increased, changing the size of the interstitial gap between the blocks. Wall thicknesses of the gap control block were 3, 4 and 5 mm.
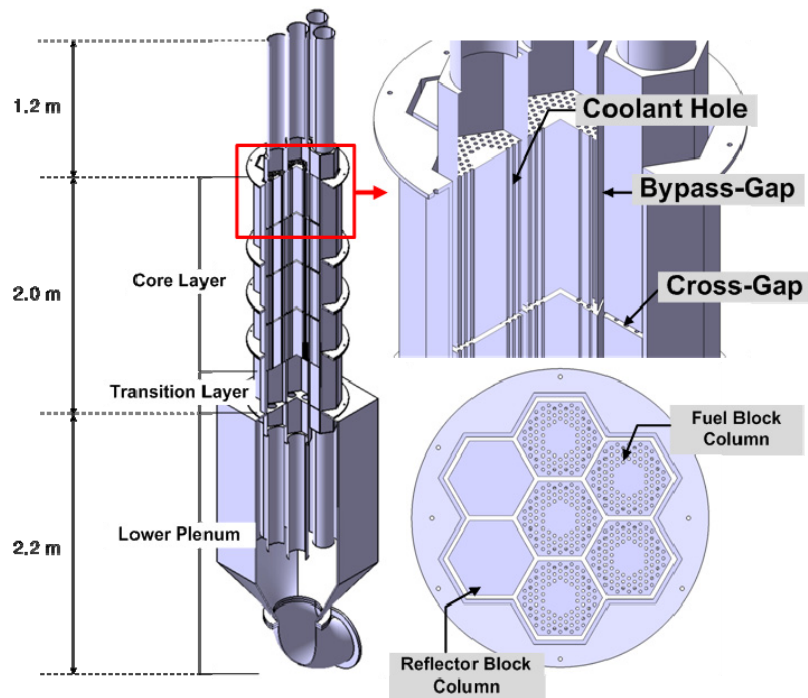
Figure 2-1. Schematic diagram of multiblock air test facility.
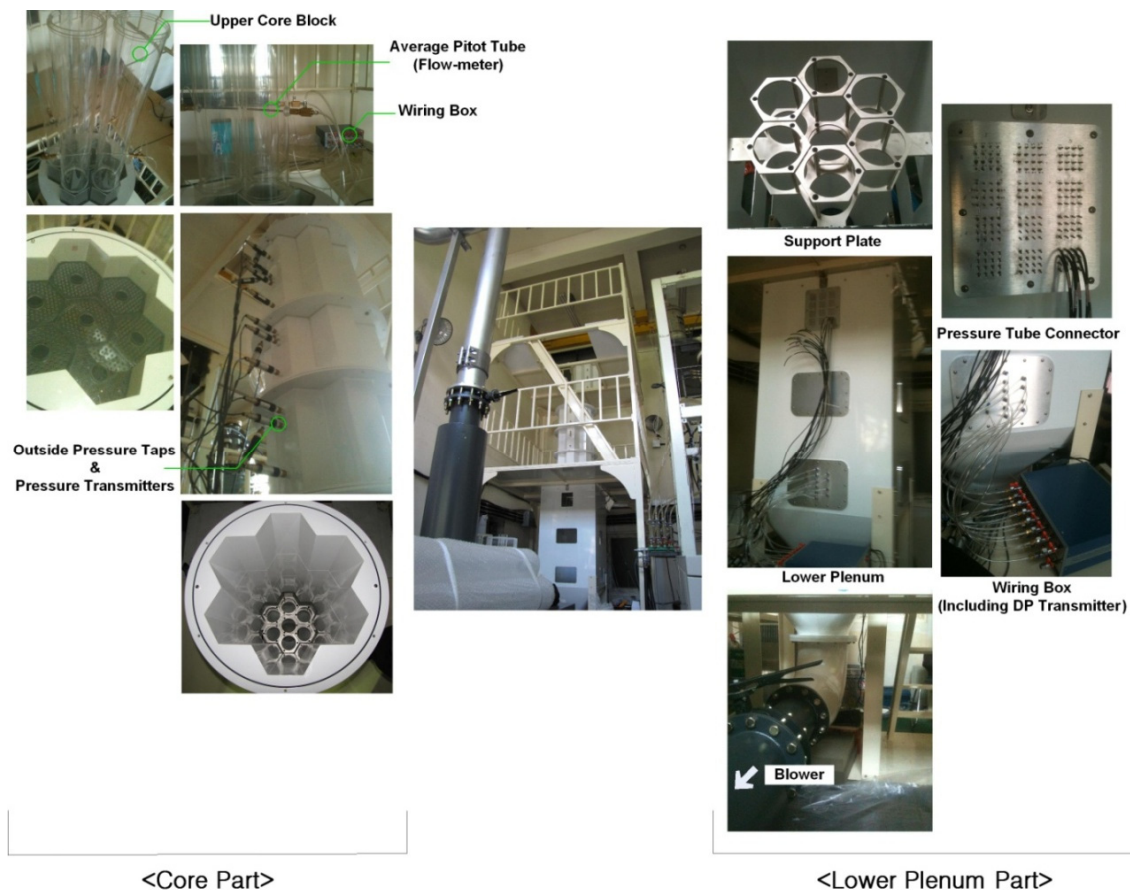
Figure 2-2. Construction of multiblock air test facility.

Fuel block

Reflector block

Transition block

Wall thickness of gap control block

Fuel block combined with gap control block
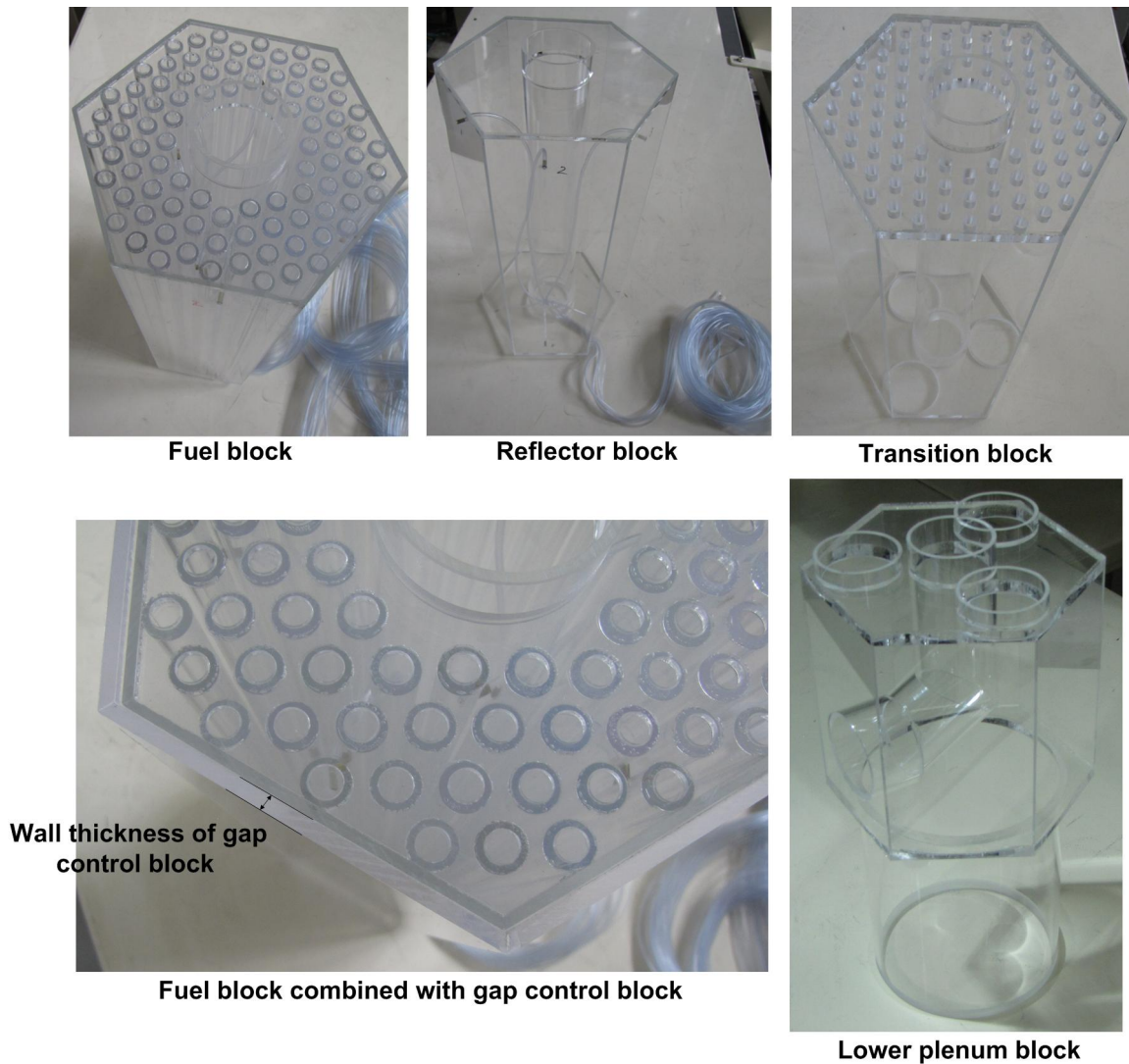
Lower plenum block

Figure 2-3. Pictures of fuel, reflector, transition, lower plenum and gap control block.

2.2   Construction of MIR Experiments (INL/TAMU)

A scaled model was developed for installation in INL's MIR test facility during the second year. Facility construction was also completed and construction of the model continued from the second year into the third year.

The scale of the INL model is a factor of 2.016 greater than the actual geometry. The model is based on the General Atomics (GA) Modular High-Temperature Gas-Cooled Reactor (MHTGR) (GA Technologies 1992)[1] prismatic reactor. Figure 2-4 is a sketch of three adjacent prismatic blocks from a GA MHTGR. Because the focus of the standard problem is the gap flow, the model was chosen to center on the gap region between three blocks. The scaled model geometry is bound by the thick red line in the figure. Only three standard coolant channels are included from each block in the model. The junction of the three gaps is the center of the scaled model.
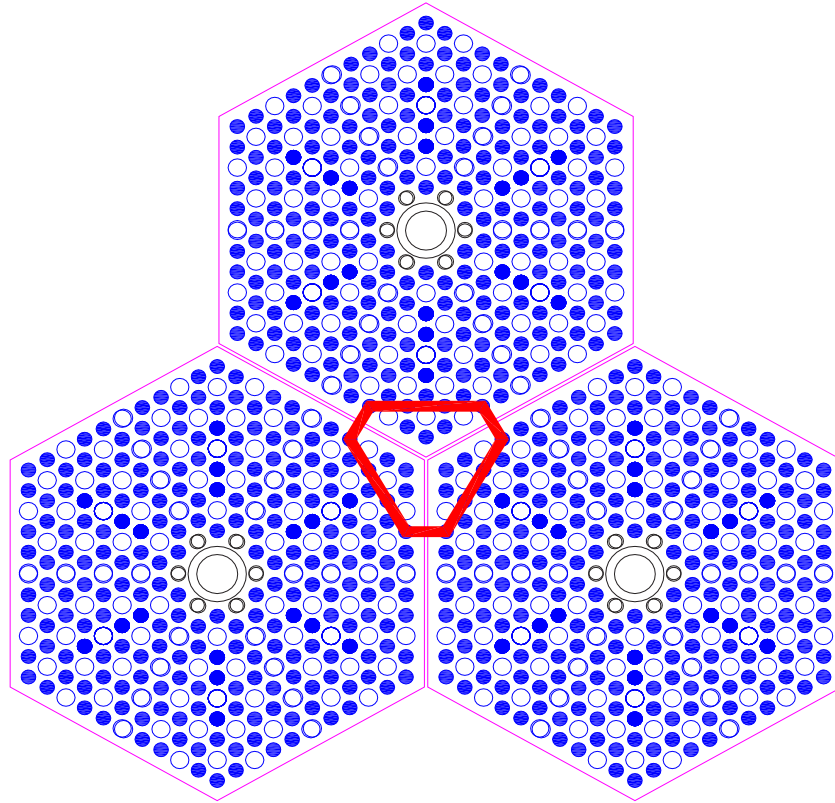
Figure 2-4. Three prismatic blocks from the MHTGR reactor and outline of test model geometry.

Figure 2-5 shows a close-up view of the source of the model geometry and a view that eliminates those things that are extraneous to the bypass model geometry. The lines parallel to the gap edges represent bevels machined in the graphite in the original MHTGR prismatic blocks. Three coolant channels are present for each block. Note that the flow in the bypass scaled model will be isothermal.
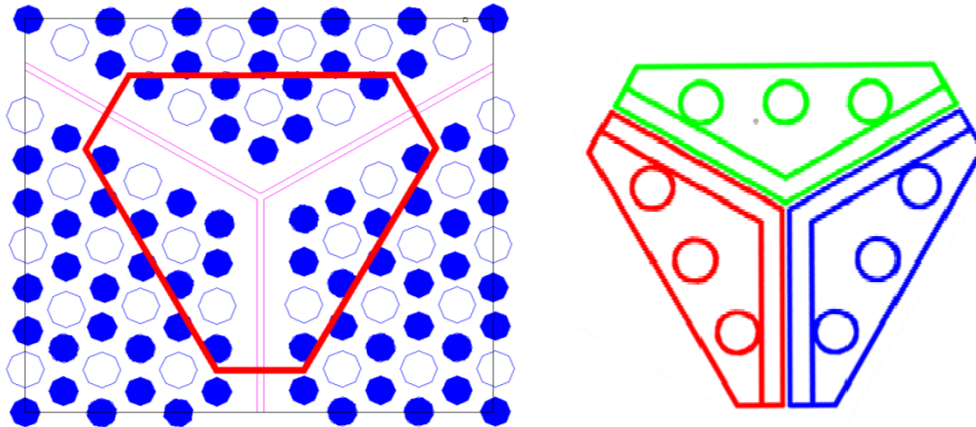
Figure 2-5. Close-up view of the origin of the bypass flow model and a cross-section view of the model.

Figure 2-6 illustrates the primary components of the bypass flow model. These include the inlet annulus where the working liquid (mineral oil) enters and is directed to the hemisphere which was designed to give uniform distribution to the bypass test section; the hemisphere directs the flow uniformly into the test section, an upper plenum, an upper fuel block, an adjustable horizontal gap, a lower fuel block, and two orifice plates that enclose screens in the channel and gap flow paths. The screens are intended to increase the pressure drop over the shorter lower fuel block to the same value as the upper fuel block. Also shown are the flow paths of the mineral oil along with the layout of the supported model as it will sit in the working section of the MIR test facility. The bypass model is designed to have adjustable gap widths. The vertical gaps visible in Figure 2-5 are adjustable from 2, to 6, to 10 mm, representing 1, 3, and 5 mm in the actual block size. The horizontal gap can be set to widths of either 2 or 10 mm.
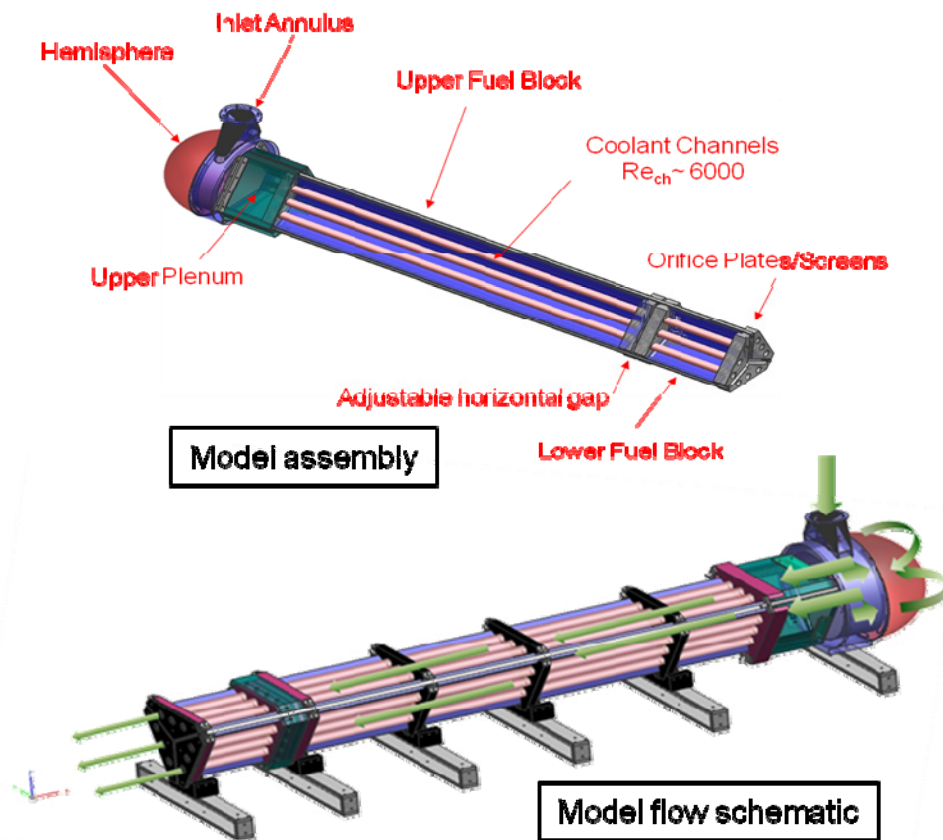
Figure 2-6. Schematics of the bypass model showing components and flow paths.

Following completion and assembly of the MIR hardware, a reference data set was recorded—however, considerable alignment difficulties have prevented a comprehensive data set to be generated to date. The first data set will be completed by the end of FY 2011.

Construction of the MIR facility and test section at TAMU was completed and shakedown tests have begun. The model inserted into the facility is shown in Figure 2-7. An isometric drawing of the test section is shown in Figure 2-8. The TAMU MIR test section allows a wide variety of bypass gap sizes to be investigated.
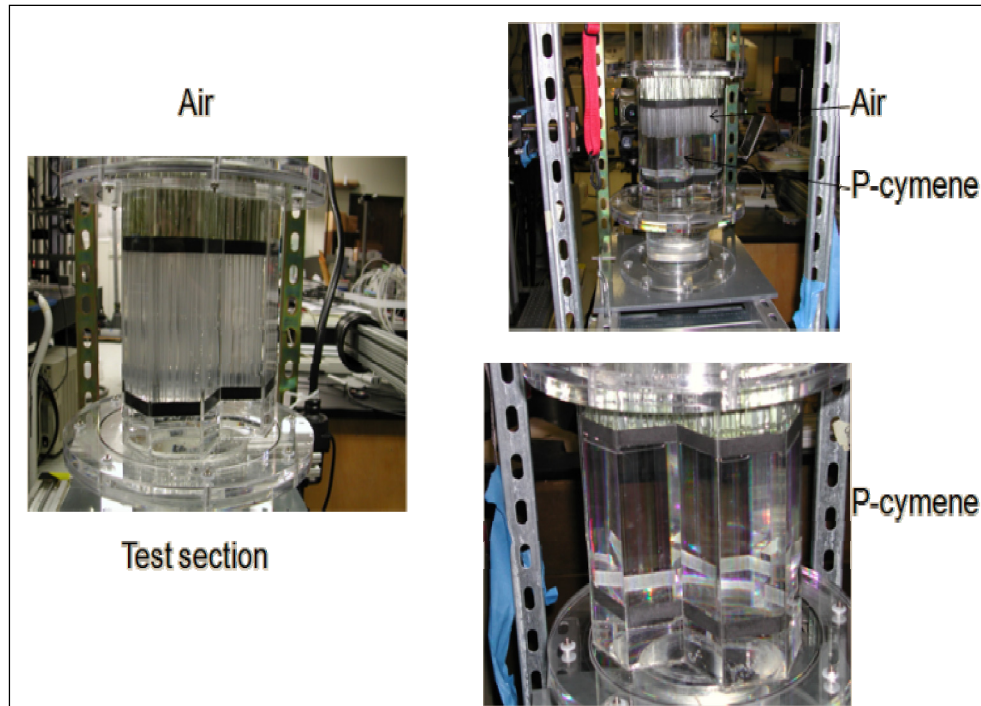
Figure 2-7. Photographs of test section with P-cymene as the working fluid and air.
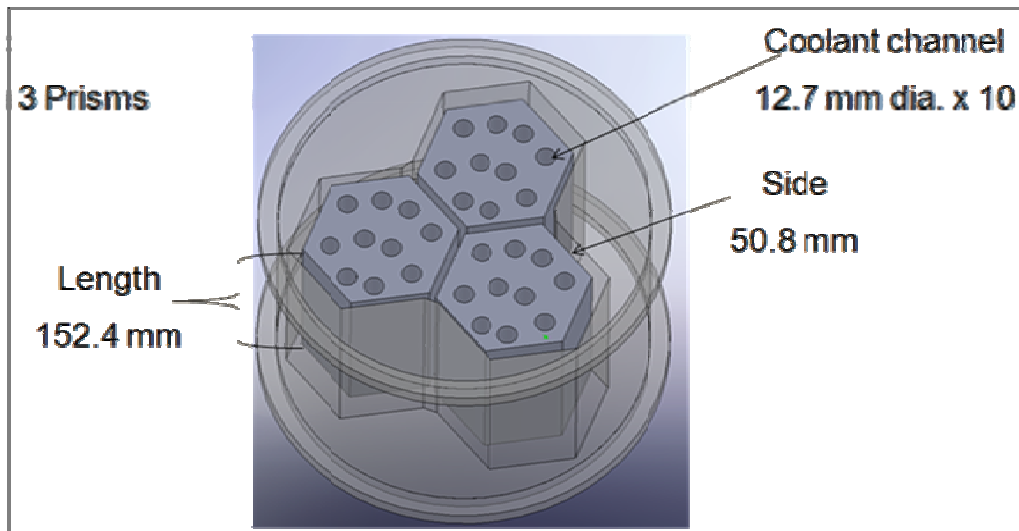
Figure 2-8. Isometric drawing of three prismatic blocks, each with 10 coolant channels and a typical bypass gap between each block with the three block assemblies mounted in their flow housing.

4. Planned activities

   None

5. Issues/concerns

   None

3.   TASK 2

1.   Task title and responsible lead:

Determination of experimental conditions and development of measurement requirements and techniques (KAERI/SNU)

2.   Brief description of objectives:

Determine experimental conditions and measurement requirements for providing sufficient data sets for the assessment of thermofluid analysis tools with consideration of various combinations of the block elements and the gap size.

3.   Task Technical Status Overview:

3.1   Preliminary Estimation of Bypass Flow Gap Sizes for a Prismatic Core Very High Temperature Reactor (KAERI)

The core bypass flow in the prismatic very high temperature reactor (VHTR) varies with the core life because of the irradiation shrinkage/swelling and thermal expansion of the graphite blocks. This has been a well-known fact but the detailed gap distribution in the core has not been evaluated. This work focused on the evaluation of the gap size distribution to give an idea or insight for the bypass flow experiment.

3.1.1   Modeling of Dimensional Changes of Graphite Blocks

The amount of dimensional change of the graphite can be assumed to be a function of the irradiation fluence and the irradiation temperature. Since the data accrued from the reactor operation and experiments are scattered, to simplify the evaluation procedure in the present study, it is assumed that the graphite is isotropic and a dimensional change at a fixed irradiation temperature is represented by a single curve as shown in Figure 3-1. For a given fluence and temperature, therefore, the dimensional changes of the graphite can be determined by a linear interpolation between the curves.[2,3]
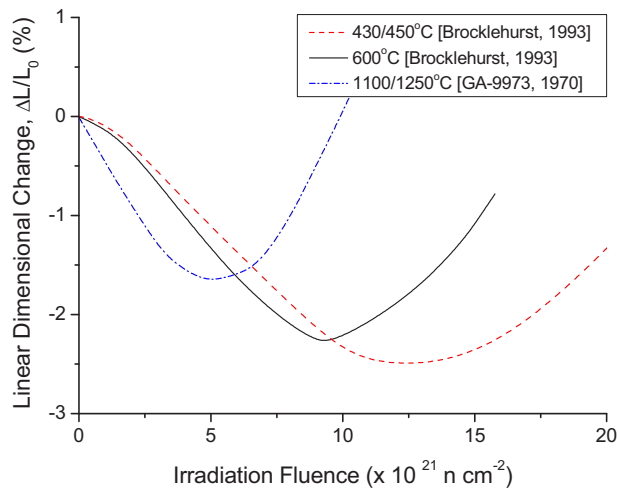
Figure 3-1. Dimensional change of the graphite with irradiation fluence.

Another major factor affecting the core bypass flow is the coefficient of thermal expansion (CTE), which also depends on the neutron irradiation and temperature. A linear relationship of between the mean CTE in the range of 20 to120°C and the CTE in the range 20-T°C is proposed by Tsang et al.[4] as follows:

$$\alpha_{(20-T)} = \overline{\alpha}_{(20-120^{o}C)} + \overline{B}(T)$$

(2-1)

where $\overline{B}(T)$ is a polynomial fitted for temperature up to 1500°C. A study by Marsden et al.[5] showed that their measured data compared well with the values predicted by Tsang's linear relationship. Thus, Equation (2-1) is adopted for the CTE calculation.

Four factors considered for evaluating the local gap size are the installation tolerance of graphite blocks, thermal expansion of metallic core support plate, thermal expansion of graphite blocks, and irradiation shrinkage/swelling of graphite blocks.

The first and second factors result in constant gaps distributed uniformly between the blocks. A gap of 1 mm between the blocks is assumed for the installation tolerance. The thermal expansion of core support plate increases relative distances between graphite blocks and results in an increase of bypass flow gaps being calculated from an average temperature rise, CTE of the core support plate, and its dimension along the diameter. The constant gap can be minimized or eliminated by adopting a so-called core restraint mechanism (CRM), which prevents radial outward movement of the permanent reflector by using material that has a low thermal expansion coefficient. The third and fourth factors have effects on the local variation of the gap size determined from Figure 3-1 and Equation (2-1) for a given radiation dose and temperature of each block. A tool for computing gap size distribution is prepared.

3.1.2 Estimation of Bypass Flow Gap Sizes in a Prismatic Core

The Nuclear Hydrogen Development and Demonstration PMR200 is selected as a reference reactor for the gap size evaluation, the core of which consists of 66 columns and 6 layers of fuel blocks. The core inlet and outlet temperatures are 490 and 950°C respectively. A three-batch axial shuffling scheme is used for core cycles, and the core reaches an equilibrium state at the 7th cycle from the initial core (IC). Figure 3-2 shows the one-sixth core model and its block numbering order.
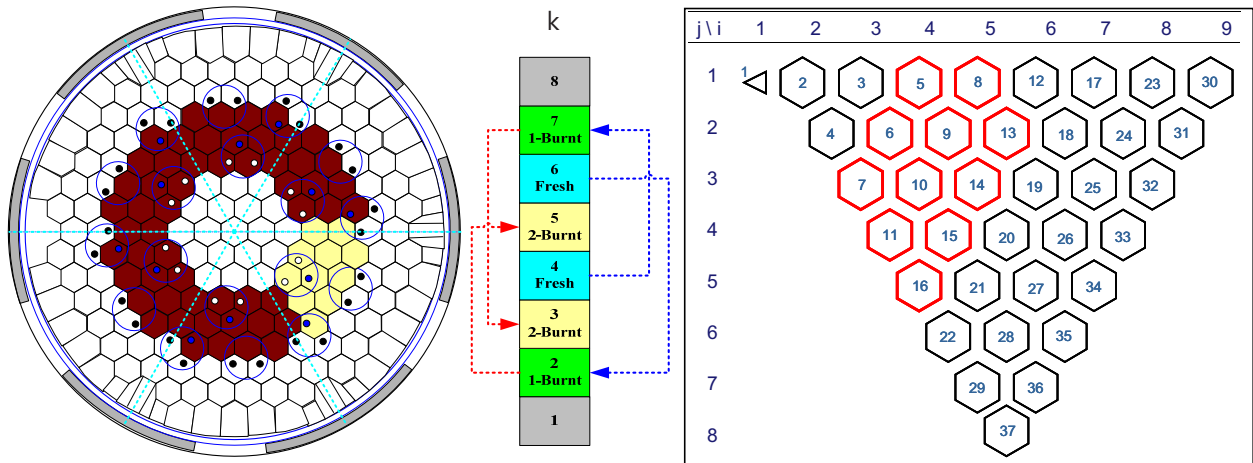
Figure 3-2. The one-sixth core model of Nuclear Hydrogen Development and Demonstration PMR200 and block numbering order.

The gap distributions were calculated based on neutron fluence and temperature distributions obtained from the core analysis for the one-sixth core model,. The core conditions investigated were the IC and the equilibrium cores (EC) from the 7th cycle, first EC, to the 14th one after for which the replacement of side reflectors is expected because of their lifetime.

Figure 3-3 shows total gap size distributions for the IC at end of cycle (EOC). Without CRM, there are some gaps because of the installation tolerance and both thermal expansion of core support plate and the graphite blocks at hot condition of beginning of cycle (BOC). The irradiation shrinkage at EOC increases the gaps, but the result, considering CRM, shows no gaps at the BOC condition. The gap distribution at EOC is nearly similar to the case without CRM, but the total size is much smaller. Maximum gap sizes and their locations are compared in Table 3-1. The gap sizes are bigger in EC than in IC because of the shrinkage of once or twice burnt fuel blocks. The CRM eliminates the gaps of IC at BOC, which is maintained during the whole core cycles. But the CRM do not change the location of maximum gap. Similar gap sizes are repeated during the EC cycles but the gap size of reflector starts to exceed the fuel blocks at EC5 because of the accumulated irradiation shrinkage. The biggest gap size is 12.5 mm for the case without CRM. With CRM, it reduces to 8.8 mm, which is still big enough to influence core flow distribution.
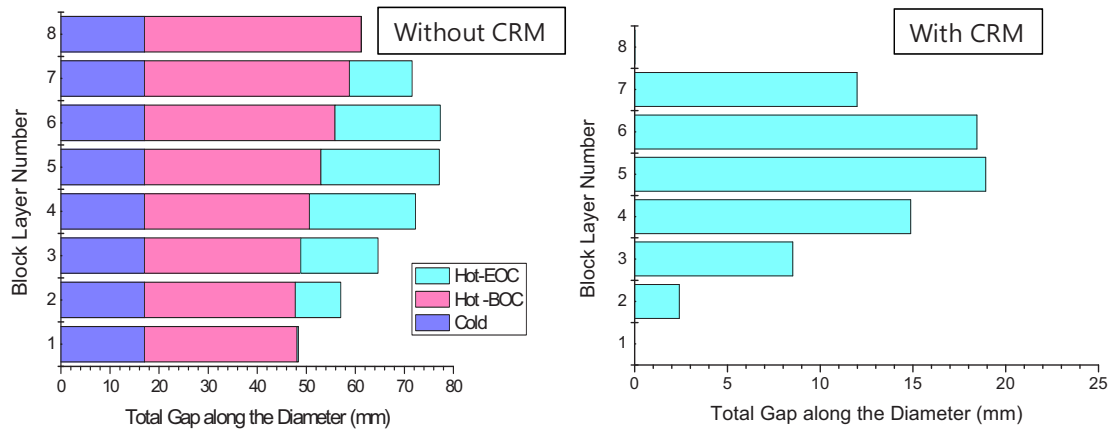
Figure 3-3. Total gap size distributions for the IC with and without CRM.

Table 3-1. Maximum gap sizes for each core cycle and their location.

| | Maximum gap size (mm) | | | | | | location of maximum gap: i, j, k (Figure 3-1) | | |
| | With CRM | | | Without CRM | | | | | |
Core Cycle	BOC	MOC	EOC	BOC	MOC	EOC	BOC	MOC	EOC
IC(Cy01)	3.9	4.9	7.3	0.2	1.2	3.6	9,1,2	4,1,5	4,1,5
EC1(Cy07)	9.5	9.9	11.4	5.8	6.2	7.6	5,3,5	5,3,5	5,3,7
EC2(Cy08)	9.5	9.9	11.4	5.8	6.2	7.6	5,3,5	5,3,5	5,3,7
EC3(Cy09)	9.5	9.9	11.4	5.8	6.2	7.6	5,3,5	5,3,5	5,3,7
EC4(Cy10)	9.5	9.9	11.4	5.8	6.2	7.6	5,3,5	5,3,5	5,3,7
EC5(Cy11)	10.0	10.9	11.7	6.3	7.2	7.9	3,1,6	3,1,7	3,1,7
EC6(Cy12)	10.9	11.8	12.5	7.2	8.1	8.7	3,1,7	3,1,7	3,1,7
EC7(Cy13)	11.3	11.9	12.5	7.5	8.2	8.8	6,1,7	6,1,7	6,1,7
EC8(Cy14)	11.4	11.9	12.4	7.7	8.2	8.7	6,1,7	6,1,7	6,1,7

Detailed gap distributions for EC1 and EC8 at EOC are shown in Figure 3-4 and 3-5. The gap distribution along block layers is irregular because of axial shuffling. The layer loaded with fresh fuel blocks gives smaller gap sizes. The top layer of EC1 reveals bigger gap distribution than others loaded with twice-burnt fuel blocks, meaning twice-burnt fuels have passed a turn-around from shrinkage to

swelling. The gap distribution in EC8 is different from EC1. The reflectors near fuel blocks irradiated by fast neutron throughout the EC cycles reveal bigger irradiation shrinkage than the fuel blocks.
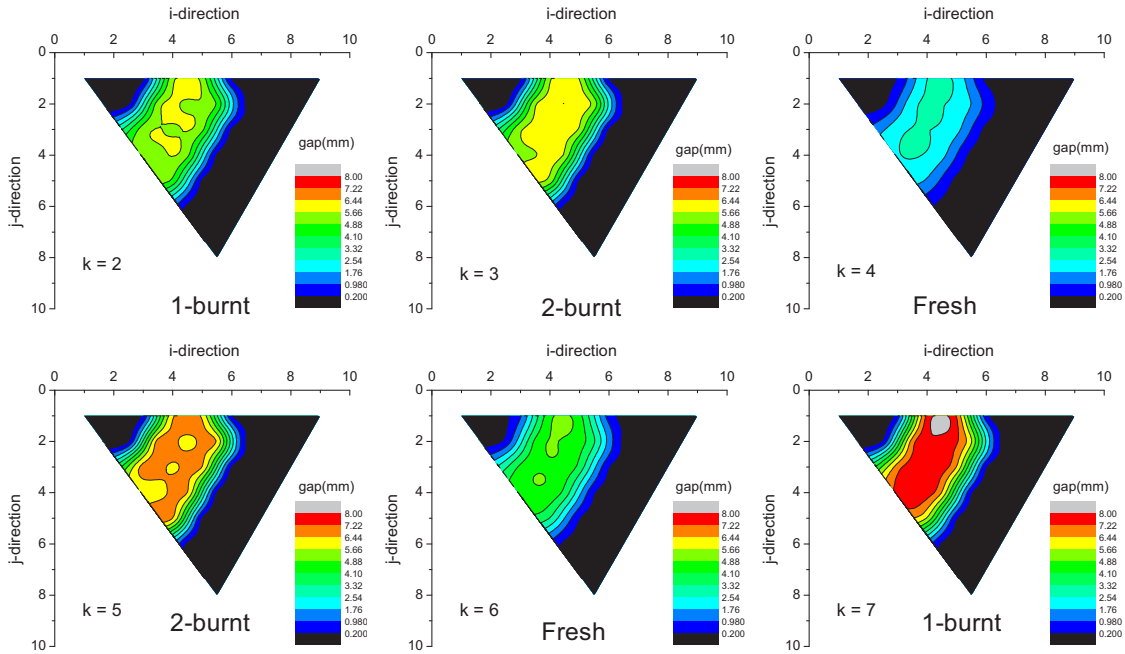
Figure 3-4. Gap distributions of EC1(Cy07) at EOC.
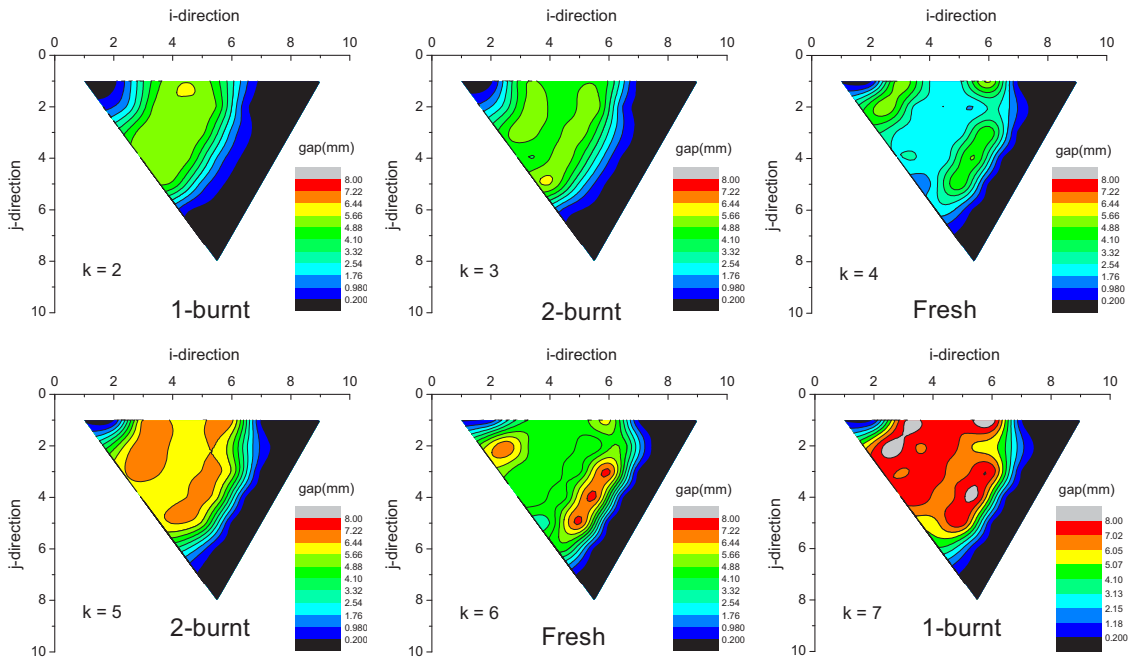
Figure 3-5. Gap distributions at EC8(Cy14) at EOC.

The above gap size distribution was calculated with the assumption that the side reflector was not replaced during eight core cycles, which results in larger gaps in the region between the side reflector blocks and fuel blocks. To investigate a sensitivity of the bypass gap distribution to the replacement

period of side reflector, the gap size distribution was recalculated for the same PMR200 core with the assumption that the reflector blocks were replaced every two core cycles.

Figure 3-6 shows the results for the case with the replacement of side reflectors. Gap distribution for the first EC is not shown because it is the same as the case without the replacement of side reflectors. The difference is observed when comparing two results for the 8th EC at the EOC. Without the side reflector replacement shown in Figure 3-5, the larger gap occurs in the side reflector because the irradiation during 8 cycles make the reflector blocks shrink more than some fuel blocks. However, the gap size in the side reflector region decreases as the reflectors are replaced in every two cycles. The large gaps are localized in the fuel region.
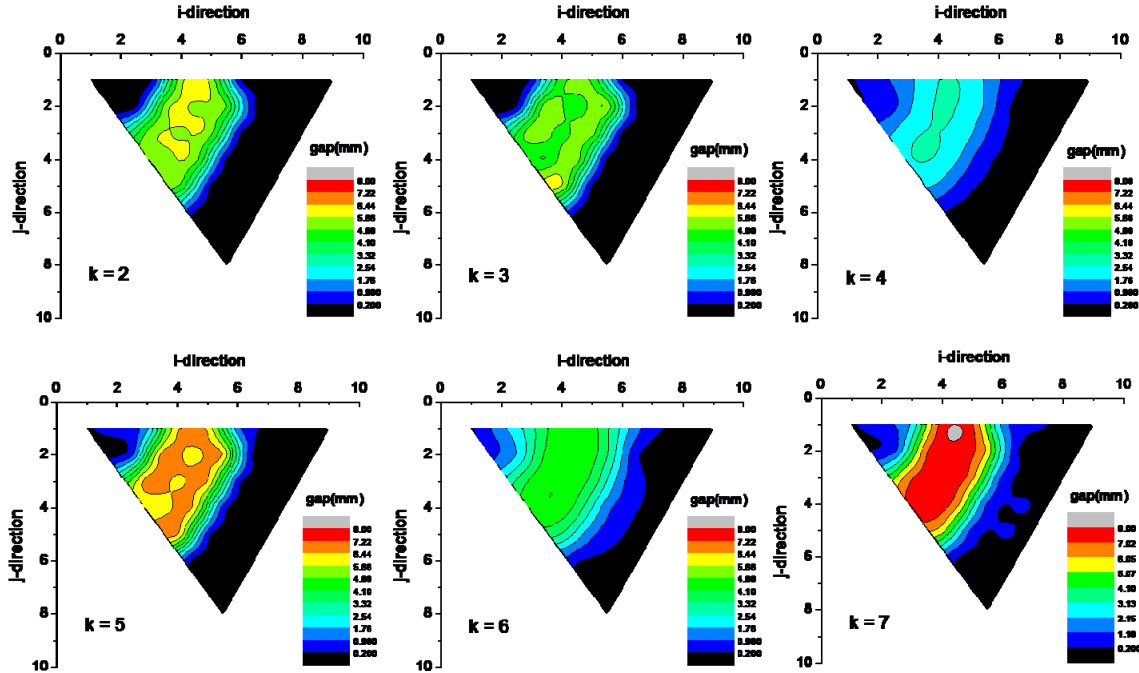
Figure 3-6. Gap distributions for the cases with replacement of reflector blocks at EC8(Cy14) at EOC.

3.2   Scaling Analysis of Air Test Facility (SNU)

In order to determine the experimental conditions and the measurement requirements, the similitude analysis and preliminary CFD simulation are carried out. The total coolant flow rate of PMR200 (the reference reactor of the experimental facility) is 82.79 kg/s. The active core consists of 66 fuel columns 6 blocks high. The similitude analysis for the Reynolds number of the coolant hole and the bypass gap is carried out to determine the total mass flow rate of the experimental facility. Assuming that the bypass gap size is 2 mm and the bypass flow is 5%, Reynolds numbers of the coolant hole and the bypass gap of the PMR200 are ~20,000 and ~2,000 respectively. Considering the change of the working fluid from the helium gas at 7 MPa and high temperature (500–900°C) to the air at NTP and the scale-down of the facility, the flow rate of each fuel block of the multiblock air test facility should be 0.224 kg/s to maintain the dynamic similarity. Results of the similarity analysis are summarized in Table 3-2. Figure 3-7 shows the result of the preliminary CFD analysis of the core part of the test section. Total pressure drop of the core part is approximately 6.0 kPa.

Table 3-2. Comparison of the SNU experimental conditions with reference reactor.

	Reference reactor	Experimental condition	Ratio
Dimensions of block	Height: 0.793 m Flat-to-flat width: 0.36 m	Height: 0.4 m Flat-to-flat width: 0.18 m	0.5
Working fluid	Helium	Air	N/A
Operating condition	7 MPa, 490~950℃	NTP	N/A
At each block column, - Coolant flow - Bypass flow	 1.1228 kg/s 2.196e-2 kg/s	 0.2239 kg/s 1.667e-3 kg/s	N/A
Diameter and number of coolant hole of fuel block	Total 108 holes: 102×Φ15.9, 6×Φ12.7	Total 90 holes: 90×Φ8	0.5
Coolant hole Re	18,489	22,793	~1.23
Bypass gap (2 mm) Re	1,500	241	~1.6
Coolant leakage perimeter			~1.0
Area ratio of the bypass gap (BG) to total flow area	5.62% (BG 2 mm) 10.6% (BG 4 mm) 19.2% (BG 8 mm)	22.58% (BG 2 mm) 36.85% (BG 4 mm) 46.67% (BG 6 mm)	
Pressure drop of coolant hole	51.1 kPa	6.0 kPa	
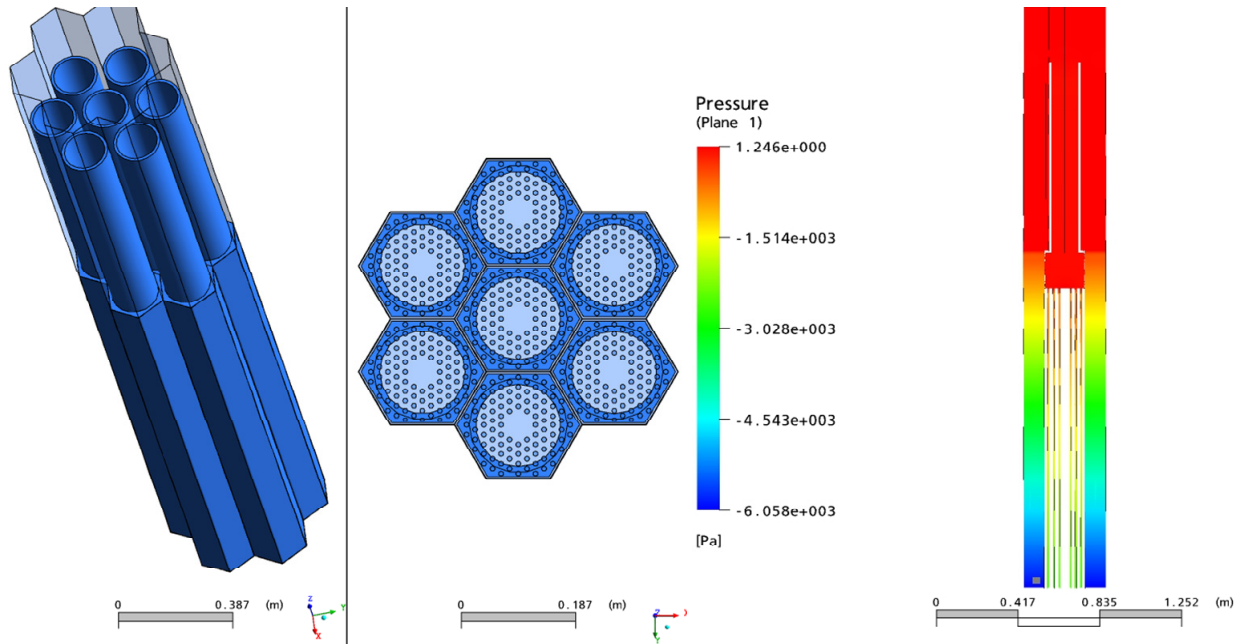
Figure 3-7. Preliminary CFD analysis of the core part of test section.

CFD analysis was carried out to evaluate the effect geometry of lower plenum has on flow distribution. Figure 3-8 shows that the elbow of diameter 0.36 m was installed to connect the lower plenum part to the blower. Figure 3-8 and Table 3-3 show the outlet flow rates of fuel column were uniform so the effect of the lower plenum geometry was negligible. The pressure drop in the lower plenum was less than 1.0 kPa and its effect on overall pressure distribution was considered to be small.
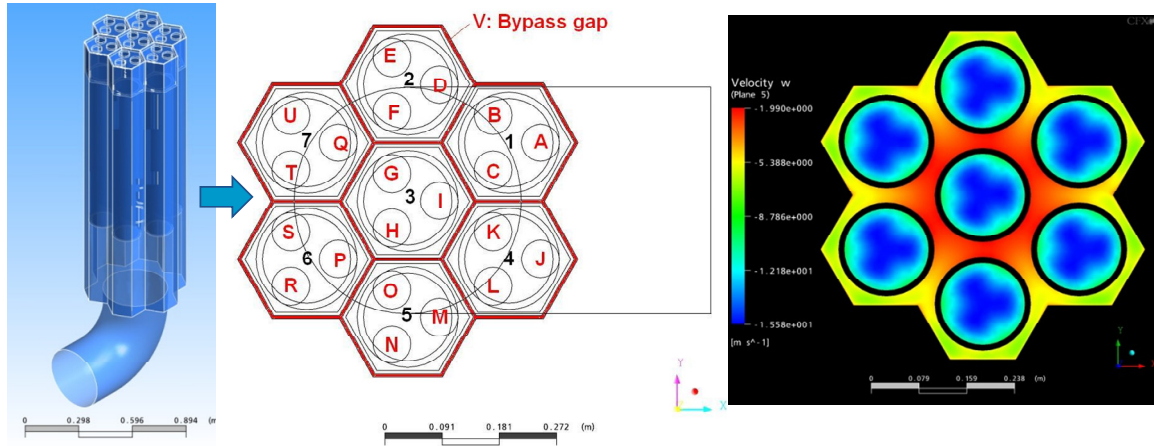
Figure 3-8. Preliminary CFD analysis of the lower plenum part of test section.

Table 3-3. Flow distribution of block column in the lower plenum part.

Block index	Flow rate ratio of block column to total flow
1	14.28
2	14.25
3	14.30
4	14.29
5	14.29
6	14.28
7	14.28
Average	14.28

3.3   Measurement Techniques for the SNU Air Test (SNU/KAERI)

The objective of the SNU multiblock air test was to estimate the effects of block combination, size of the bypass gap and cross-flow gap, on the bypass flow distribution. For this purpose, mass flow rates at the inlet and outlet of the block columns and the static pressures at the coolant holes and the bypass gaps were measured. Since the pressure distribution of the specific flow channel was determined by the mass flow rate of that channel, the information for the mass flow rate of the channel could be obtained by measuring the pressure. In particular, the direction of the cross flow could be inferred by the pressure distribution near the cross-flow gap.

Structure of the fuel type test block is shown in Figure 3-9. A total of 16 pressure taps were installed in the test block to measure the static pressures of the coolant holes within the fuel block and bypass gaps of the block periphery. Pressure taps on five coolant holes and three side walls were installed. For respective measuring points, two pressure taps were installed in the inlet and outlet of the channels to measure the pressure drop of each channel. The dimension of the test block was scaled down to half of the original fuel block. The number of coolant holes is reduced from 108 to 90 because 18 coolant holes at the center of fuel block are removed. Instead, a guide pipe 6.0 cm in diameter was installed to secure the space for the pressure tubes that connect the pressure taps in the experimental facility and the outside measuring devices.
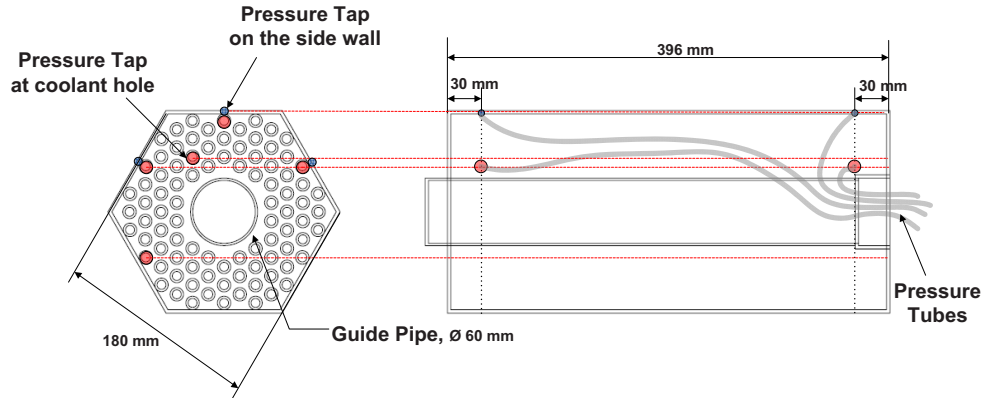
Figure 3-9. Schematic diagram of fuel block.

Since the structure of the test section is symmetric, the pressures of entire bypass gaps in the test section could be measured as shown in Figure 3-10. Furthermore, 14 pressure taps on the side wall of the test section shroud were installed along the flow direction to measure the local pressure distribution nearby the cross-flow gap.

◇ **Pressure measurement in bypass gap (outside)**

◆ **Pressure measurement in bypass gap (Inside)**

● **Pressure measurement in coolant hole**
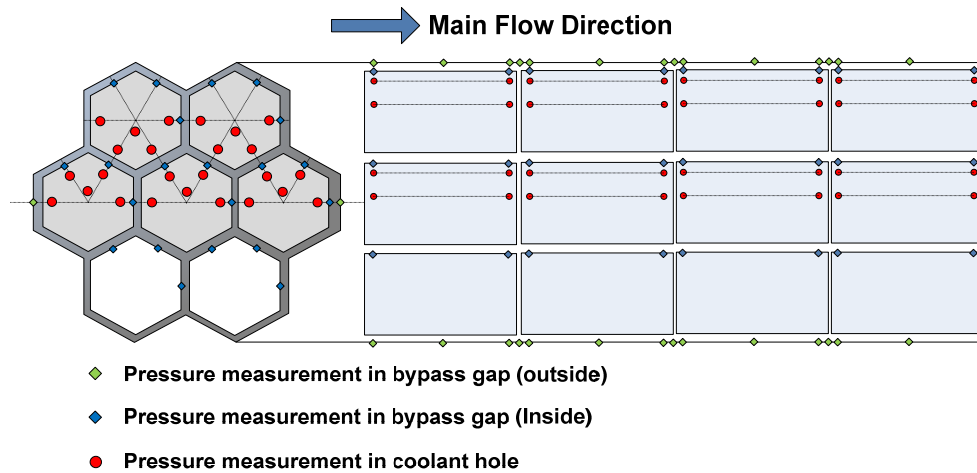
Figure 3-10. Pressure measuring points in the SNU multiblock test facility

3.4   Preliminary Estimation of Air Test Experiment (KAERI)

The multiblock air test consists of a complex combination of 28 test blocks with inlet and outlet sections. This makes the experimental setup and the data measurement difficult because the experimental setup requires a selection of experimental cases not only for producing data adequate for the code validation but also for reducing the experimental time and cost. Preliminary analyses of the multiblock air test were therefore performed by using a CFD code and the GAMMA+ code.

3.4.1   CFD Analysis

One advantage of the CFD analysis is providing a detailed flow distribution, which is difficult to measure in the air test. Preliminary CFD analyses for the air test were performed to provide insight for determining the experimental conditions. The CFD model, including the test section with the outlet region, was established as shown in Figure 3-11. The node number of mesh system is about 10 to 20 million, depending on the analysis cases.
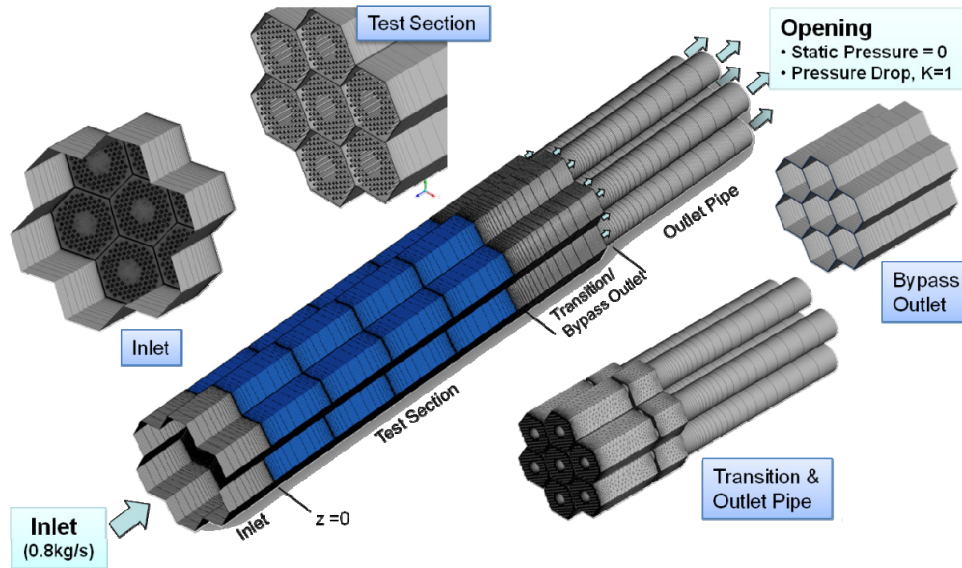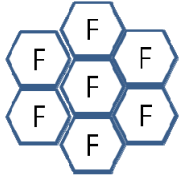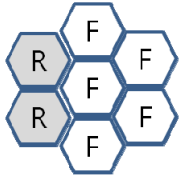
Figure 3-11. CFD model for the air test facility

The analysis cases considered are listed in Table 3-4. With two types of block arrangements (F7 and R2), three uniform bypass gap distributions (BG2, BG4, and BG6) and two variant bypass gap distributions (BG6242, BG6240) were selected for assessing the effect on bypass flow. The cross-flow gap size was fixed at 2 mm for all but the BG4 cases (F7-BG4-CG1, R2-BG4-CG1), in which the cross-flow gap of 1 mm was additionally included to estimate the effect of cross-flow gap size on the bypass flow distribution.

Table 3-4. Analysis cases considered in the CFD analyses of the air test.

Cases	Arrangement of Block Columns	Bypass Gap (BP) Size (mm)	Cross-flow Gap (CF) Size (mm)
F7-BG2-CG2	7 fuel blocks (F)	2 (uniform)	2 (uniform)
F7-BG4-CG2		4 (uniform)	2 (uniform)
F7-BG4-CG1			1 (uniform)
F7-BG6-CG2		6 (uniform)	
F7-BG6242-CG2		6, 2, 4, 2	2 (uniform)
F7-BG6240-CG2		6, 2, 4, 0	
R2-BG2-CG2	2 reflectors (R)/5 fuel blocks (F)	2 (uniform)	2 (uniform)
R2-BG4-CG2		4 (uniform)	2 (uniform)
R2-BG4-CG1			1 (uniform)
R2-BG6-CG2		6 (uniform)	
R2-BG6242-CG2		6, 2, 4, 2	2 (uniform)
R2-BG6240-CG2		6, 2, 4, 0	

The results of CFD analyses for uniform bypass gaps are compared in Figure 3-12. The results of the uniform BG cases show general trends that the bypass flow fraction decreases as it approaches the outlet and increases as the BG size increases. The largest bypass flow of 44.5% occurs in the R2-BG6-CG2 case; the smallest bypass flow of 8.5% occurs in the F7-BG2-CG2 case. The coolant flow variation in the blocks on the same layer was nearly uniform, much less than 1%. The influence of the cross-gap size on the flow distribution is so small that the CG size of 1 mm can be excluded in the experiment.

16
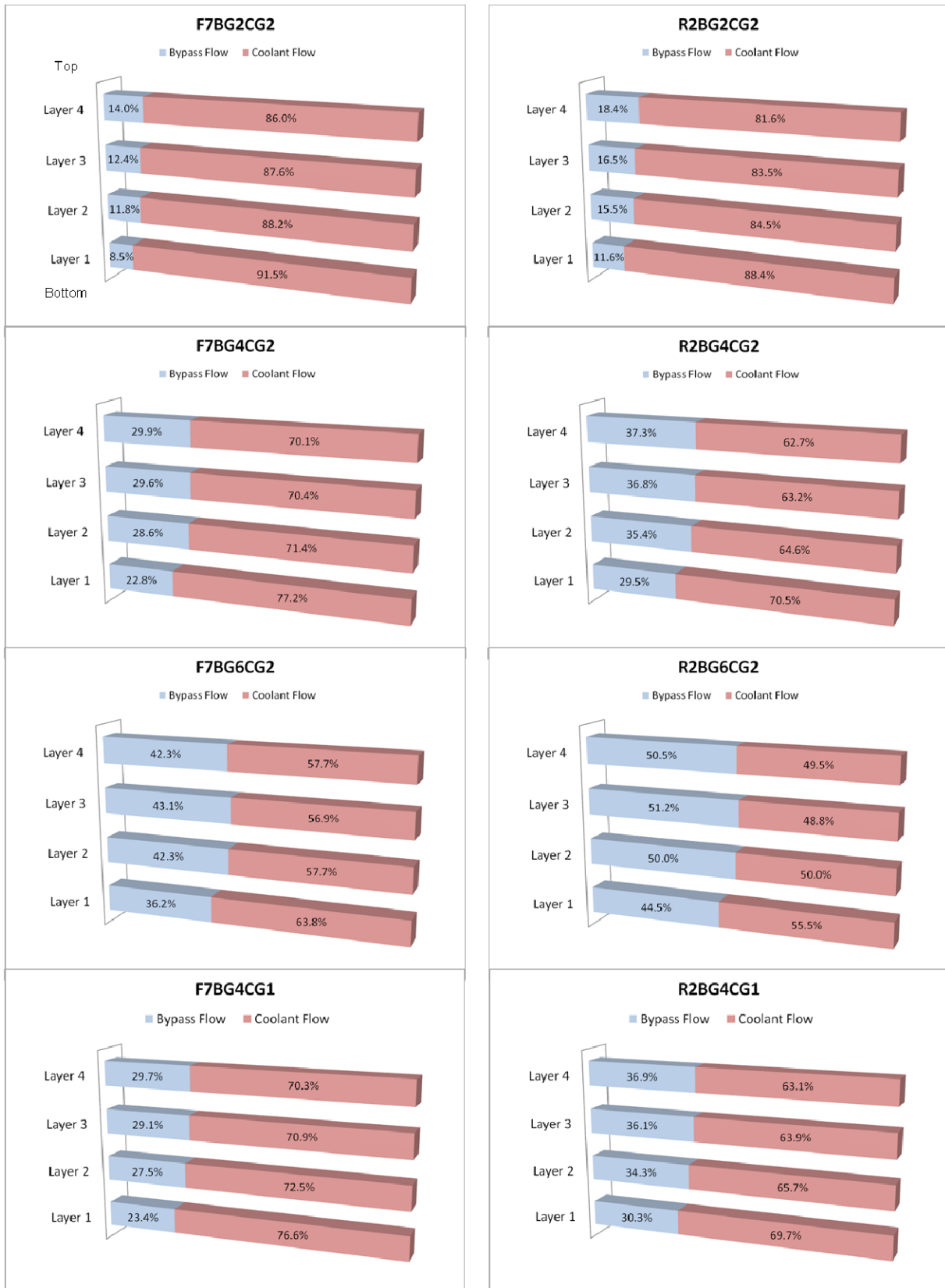
Figure 3-12. Distributions of coolant and bypass flows at each block layer for the uniform bypass gaps.

The effect of variant bypass gaps, which simulate the core at the EOC, is shown in Figure 3-13. It is clearly seen that the fraction of bypass flow is proportional to the local size of bypass gap. The case with reflector blocks reveals higher bypass flow similar to the constant BG cases with reflector blocks in Figure 3-12. The result shows that a smaller BG gap between larger gaps reduces the bypass flow, which should be larger if there are only large gaps. The case with zero BG size at the bottom mimics an installation of a device for a bypass flow reduction measure. The result shows that the countermeasure has influence on the bypass flow in the first and second layers. The bypass flow between the blocks far from the bottom remains almost unchanged.
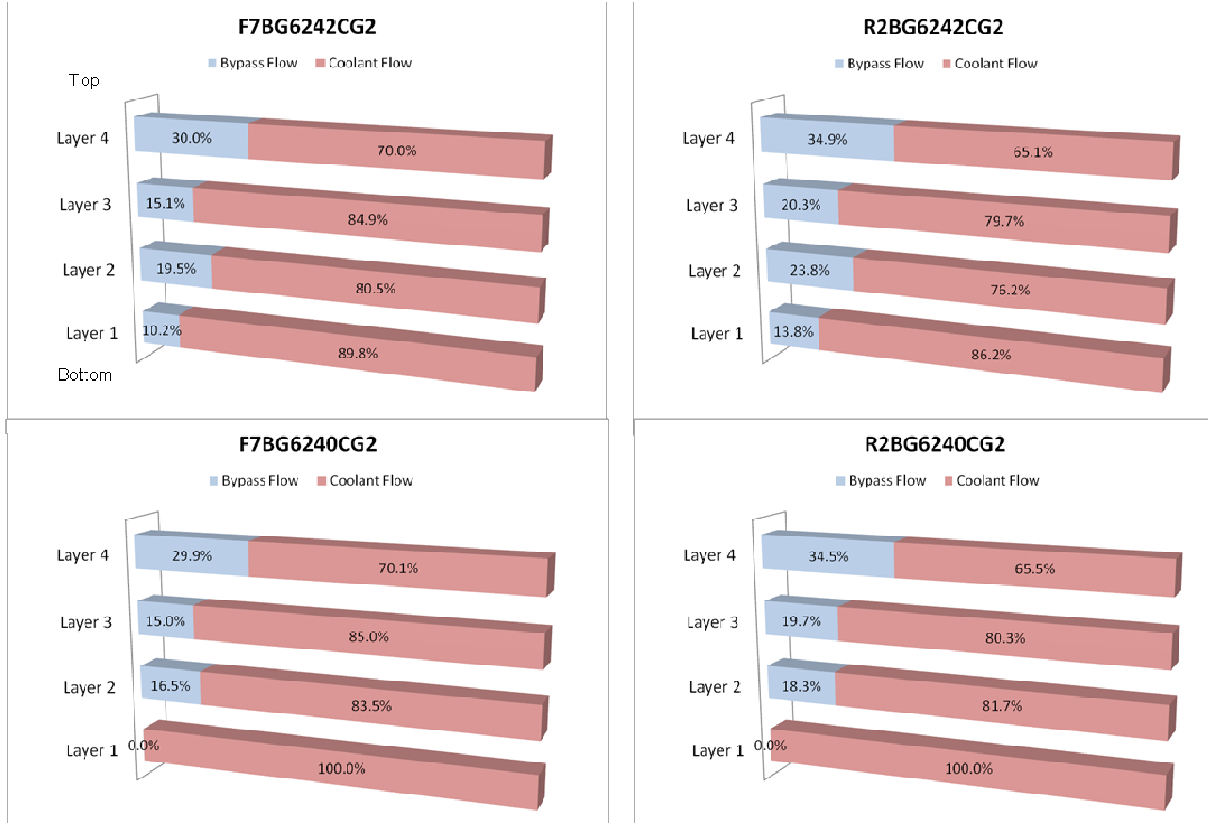
Figure 3-13. Distributions of coolant and bypass flows at each block layer for axially-variant bypass gaps.

3.4.2   GAMMA+ Analysis

System thermofluid analyses by using the GAMMA+ code had been performed to investigate its capability for predicting the complex bypass flow in the air test facility before the experimental data were available. Some parametric studies were performed and some comparisons were made with the CFD results.

Figure 3-14 illustrates the analysis model for the air test experiment. The 90 coolant channels in the block were modeled by six channels connected to the bypass gap channel in the same number, which allow cross flows between bypass gap and coolant channels. The total number of nodes is ~630, including 330 for the bypass gaps and 294 for the coolant channels and cross-flow gaps.
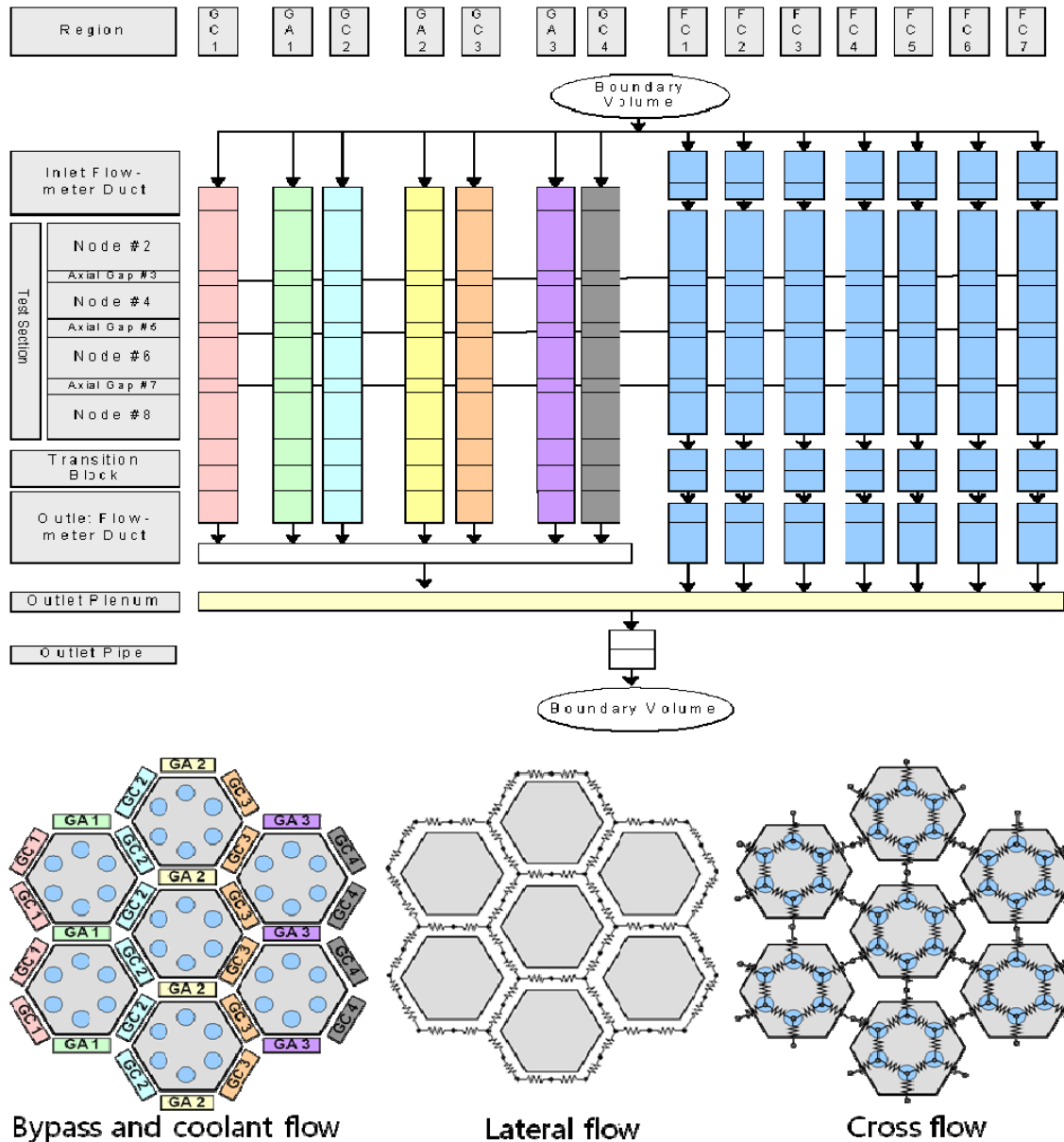
Figure 3-14. GAMMA+ model for the preliminary analysis of the SNU air test.

Table 3-5 summarizes the results of GAMMA+ calculation. The F7-BG2-CG0 case with different flow rates suggests that the bypass flow linearly decreases with the increase of the flow rate, but the rate of decrease is small. The cross-flow gap size has little effect on the bypass flow as shown in the CFD result in Figure 3-15. The predicted bypass flow fraction for the uniform BG cases is similar to the CFD results but a reduction of the bypass flow from inlet to outlet in the CFD results was not clearly predicted. A similar trend was also observed in the variant BG cases. A simple comparison of pressure distributions shown in Figure 3-15 indicates that the GAMMA+ model results in similar distribution to the CFD result in macroscopic perspective but reveals a little difference in the region occurring cross flows, which emphasizes the need of the model improvement in GAMMA+ code.

Table 3-5. Comparison of bypass flow fraction between GAMMA+ and CFD results.

Cases	Total Flow Rate (kg/s)		Bypass Flow Fraction @inlet (%)		Bypass Flow Fraction @outlet (%)	
	GAMMA+	CFD	GAMMA+	CFD	GAMMA+	CFD
F7-BG2-CG0	0.66	N/A	11.2	N/A	11.2	N/A
	0.87	N/A	10.5	N/A	10.5	N/A
	1.14	N/A	9.9	N/A	9.9	N/A
F7-BG2-CG2	0.87	0.8	10.7	14.0	9.1	8.5
F7-BG6-CG2	0.87	0.8	39.8	42.3	39.3	36.2
R2-BG2-CG2	0.59	0.8	14.7	18.4	12.7	11.6
R2-BG6-CG2	0.59	0.8	48.1	50.5	47.6	44.5
F7-BG2-CG1	0.87	0.8	10.8	N/A	9.3	N/A
R2-BG2-CG1	0.59	0.8	14.8	N/A	13.0	N/A
F7-BG6242-CG2	0.8	0.8	22.7	30.0	9.8	10.2
R2-BG6242-CG2	0.8	0.8	31.8	34.9	12.7	13.8
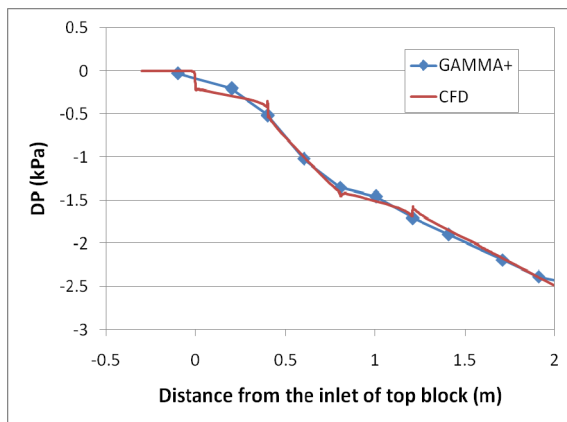
(a) Bypass gap channel
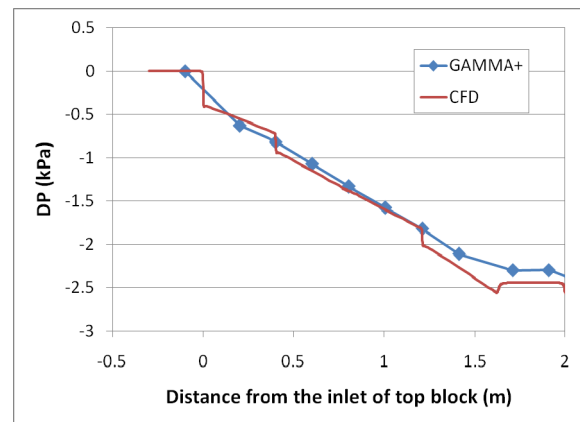
(b) Coolant channel

Figure 3-15. Comparison of pressure distributions along bypass gap and a coolant channels for the R2-BG6242-CG2 case.

4. Planned activities

    None

5. Issues/concerns

    None

4.   TASK 3

1. Task title and responsible lead:
    Testing and Interpretation of Experimental Data, KAERI/INL

2. Brief description of objectives:

    Perform the air and MIR tests independently, and reduce the test data for its interpretation

3. Task technical status overview:

4.1   Experimental Data from the SNU Air Test (SNU/KAERI)

4.1.1   Uniform Bypass Gap Test

In order to evaluate the effect of the bypass gap size, uniform bypass gap test was performed first. The tested bypass gap sizes were 2 mm and 6 mm. The cross-flow gap was not considered in the uniform bypass gap test, which leads to the mixing of the flow between the coolant hole and the bypass gap so that the effect of the bypass gap size cannot be accurately evaluated. In every layer of the test section, two reflector blocks and five fuel blocks were installed. There are four layers of the core block in the test section. Test cases are named as R2-BG2-CG0 and R2-BG6-CG0 where R2 means two reflector blocks, BG2 is bypass gap of 2 mm, and CG0 is cross-flow gap of 0mm. CFD analysis was carried out to investigate the flow characteristics in detail. CFD simulation results were validated by comparing them with the experimental results.

(a) *Bypass Gap Measurement.* Bypass gap size was measured at the top of each block layer after every installation. Average bypass gap sizes of each layer and 7th block column, which is located at the center, are summarized in Table 4-1 and Table 4-2. Since the scale of the bypass gap is in millimeter, tolerances of the test blocks and test-section have an influence on the experimental results. The tolerance of the experimental apparatus was considered so that the bypass gap around the central block column was controlled to correspond to the target value. Average bypass gap size of the R2-BG2-CG0 case is bigger than the target value of 2 mm while that of the R2-BG6-CG0 case is close to the target of 6mm.

(b) *Flow Distribution.* Bypass flow ratio is defined as the ratio of the bypass flow rate to the inlet flow rate (total flow rate). Experimental and computational results for the flow distribution were tabulated in Table 4-3 and Table 4-4. In R2-BG2-CG0 case, the bypass flow ratio was approximately 11.5% while it was 45% in R2-BG6-CG0 case. The higher bypass flow comparable to the coolant flow is because the hydraulic diameter of R2-BG6-CG0 case is bigger than the coolant channel. The hydraulic diameters of the bypass gap are 3.93 mm for the R2-BG2-CG0 case and 11.38 mm for the R2-BG6-CG0 case. When considering that the bypass flow area is linearly dependent on the hydraulic diameter, the bypass flow ratio is proportional to the bypass gap area.

Table 4-1. Measured bypass gap distribution of R2-BG2-CG0 case.

Layer	Average Bypass Gap Size (mm)	Average Bypass Gap Size Around Central Column (mm)
1	2.348	2.038
2	2.368	2.232
3	2.448	2.198
4	2.361	2.089
Transition	2.715	2.309

Table 4-2. Measured Bypass Gap Distribution of R2-BG6-CG0 Case

Layer	Average Bypass Gap Size (mm)	Average Bypass Gap Size Around Central Column (mm)
1	6.014	6.001
2	5.873	5.728
3	5.904	5.975
4	5.981	5.906
Transition	5.985	5.986

Table 4-3. Flow Distribution of R2-BG2-CG0 Case
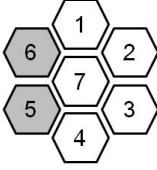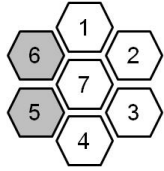
Number of Block Column		Experiment Inlet	Experiment Exit	CFD Analysis
	1	0.197244	0.20242	0.209768
	2	0.197463	0.208077	0.209811
	3	0.196618	0.20597	0.209729
	4	0.204486	0.205841	0.209695
	5	–	–	–
	6	–	–	–
	7	0.195659	0.204489	0.209672
Inlet Mass Flow Rate (kg/s)		1.234358	1.234358	1.234
Bypass Flow Ratio (%)		19.6773	16.8153	15.018

Table 4-4. Flow Distribution of R2-BG6-CG0 Case

Number of Block Column		Experiment Inlet	Experiment Exit	CFD Analysis
	1	0.11864	0.119237	0.11811
	2	0.123133	0.121589	0.118037
	3	0.116656	0.120808	0.118035
	4	0.118581	0.120088	0.118106
	5	–	–	–
	6	–	–	–
	7	0.116345	0.121551	0.118198
Inlet Mass Flow Rate (kg/s)		1.197134	1.197134	1.197
Bypass Flow Ratio (%)		50.4354	49.60692	50.67

(c) *Pressure Distribution.* Linear pressure drop occurred for the uniform bypass gap distribution as shown in Figure 4-1 and 4-2. The hydraulic diameter of the bypass gap in the R2-BG2-CG0 case was 3.93 mm, which is smaller than that of the coolant hole of 8 mm. Thus, the pressure drop of the coolant hole was bigger than that of the bypass gap at the inlet. Pressure drop inside each channel is mainly induced by the frictional loss so that it is influenced by the wall friction and mass flow rate. In general, although the flow area is equal to each other, the frictional loss in a narrow flow channel between two plates is larger than that of circular pipe channel because of the wall frictional effect. In spite of the smaller hydraulic diameter of bypass gap, the pressure gradient of coolant hole and bypass gap in the R2-BG2-CG0 case was similar because of the mass flow rate difference of the channels. In contrast, the hydraulic diameter of bypass gap in the R2-BG6-CG0 case was 11.38 mm, which is larger than that of the coolant hole. Since the difference of hydraulic diameter between the coolant hole and the bypass gap was small, the sudden contraction pressure drop at the inlet was similar for both channels. In addition, the frictional pressure drop of BG6 case was different from BG2 case.
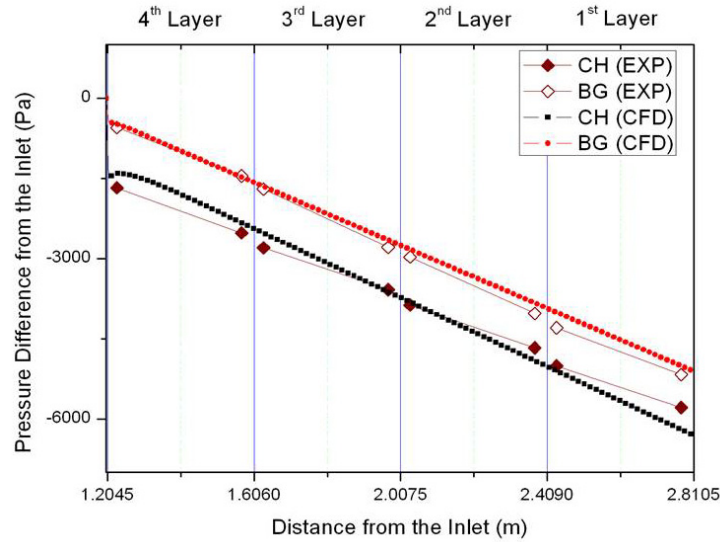
Figure 4-1. Pressure distribution of R2-BG2-CG0 case.
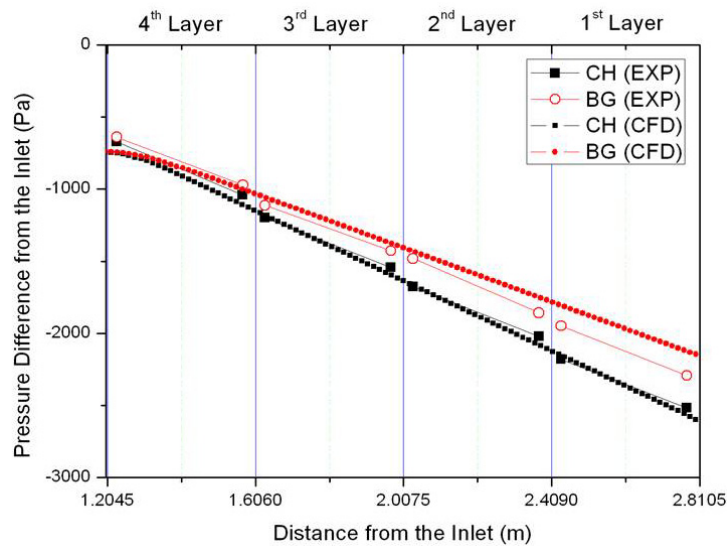
Figure 4-2. Pressure distribution of R2-BG6-CG0 case.

23

4.1.2   Nonuniform Bypass Gap Test

The bypass gap distribution in the actual VHTR core is not uniform. In particular, the local difference of the neutron fluence and axial shuffling of fuel block causes the axial distribution of the bypass gap. A nonuniform bypass gap test was included to investigate the effect of axial distribution of the bypass gap. The bypass gap size of each layer in the experiment was determined from the results of analytical study on the bypass gap distribution by KAERI.[6] The bypass gap sizes in the experimental case, named R2-BG6242-CG2, varies in order from top to bottom as 6, 2, 4, and 2 mm. A cross-flow gap of 2.0 mm is assumed to investigate cross flow phenomena caused by the change of bypass gap size.

Table 4-5 shows the measured bypass gap size of the R2-BG6242-CG2 case in which the maximum deviation of bypass gap was 4.5% at the third layer of core block. However, the bypass gap around the central block column, the region of interest, was close to the target value.

Table 4-5. Measured bypass gap distribution of R2-BG6242-CG2 case.

Layer	Average Bypass Gap Size (mm)	Average Bypass Gap Size Around Central Column (mm)
1	6.069	6.001
2	2.558	2.107
3	4.889	4.158
4	2.427	2.122
Transition	2.635	2.309

Table 4-6 shows the flow rate of each column block. The coolant flow rate at the inlet of the central block is the lowest in the experiment, 3.1% less than the average inlet flow rate. CFD result shows a similar trend but the difference is very small. The bypass flow ratio is reduced to 22.4% at exit from 39% at inlet because of two block layers of 2 mm bypass gap. Higher bypass flow ratio in the experiment than the CFD is attributed to the larger bypass gaps in the experiment.

Table 4-6. Flow distribution of R2-BG6242-CG2 case.
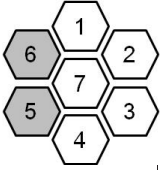
Number of Block Column		Experiment		CFD Analysis	
		Inlet	Exit	Inlet	Exit
	1	0.150006	0.176025	0.153129	0.209641
	2	0.148723	0.195093	0.153566	0.209348
	3	0.149214	0.192195	0.153563	0.209311
	4	0.151646	0.191137	0.153104	0.209605
	5	–	–	–	–
	6	–	–	–	–
	7	0.144119	0.192482	0.15355	0.209327
Mass Flow Rate(kg/s)		1.220945	1.220945	1.22094	1.22094
Bypass Flow Ratio (%)		39.08759	22.44269	37.18676	14.2274

Figure 4-3 shows the pressure distribution in the R2-BG6242-CG2 case. Frictional pressure drop decreases as the bypass gap size increases. Consequently, the pressure gradients in the 4th and second

layers were gradual where the bypass gap size was relatively large. Those in third and first layers where the bypass gap is 2.0 mm reveal a steeper gradient.
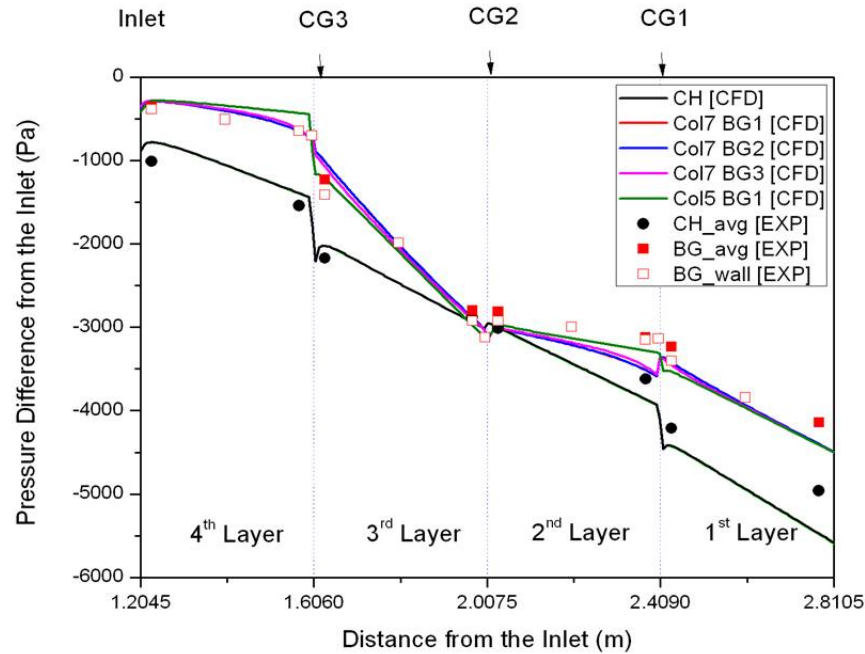
Figure 4-3. Pressure distribution of R2-BG6242-CG2 case.

Figures 4-4, 4-5, and 4-6 show the velocity distribution on the cross section of the cross-flow gap in R2-BG6242-CG2 case. The cross flow occurred strongly at the top cross-flow gap (CG3); because of the bypass gap size change from 6 to 2 mm. Characteristics of the pressure drop by the cross flow is similar to the pressure drop caused by the sudden change of the flow area. While pressure drop of the bypass gap was caused by the change in flow area, the pressure drop of the coolant hole was caused by the inflow of cross flow. The cross flow coming from the bypass gap at the CG3 makes the velocity at the coolant hole increased suddenly, leading to a sudden change in pressure. On the other hand, sudden expansion pressure distribution occurs at the middle cross-flow gap (CG2) where the bypass gap changed from 2 to 4 mm. The direction of the cross flow at CG2 reverses so that the cross flow moves from the coolant hole to the bypass gap. Since the flow area of bypass gap was extended, the pressure of the gap increased slightly. Cross flow at the bottom cross-flow gap (CG1) flows from the bypass gap to the coolant hole in common with that at CG3 since the bypass gap size changed from 4 to 2 mm. However, the pressure distribution at CG1 is different from that at CG3, which can be explained by the axial velocity distribution below.

Figure 4-7 shows axial velocity distribution of each flow channel. At the CG3, the downstream velocity in the 3rd layer is larger than the upstream velocity in the 4th layer while the downstream velocity in the 1st layer is smaller than the upstream velocity in the 2nd layer at CG1. In particular, the bypass flow to the 1st layer already decreased as it passed by the 3rd layer. The bypass flow decreases again by the cross flow at CG1, which heads toward the coolant hole. Consequently, the pressure of the bypass gap across CG1 rise slightly because of the decrease of the flow velocity as shown in Figure 4-3.
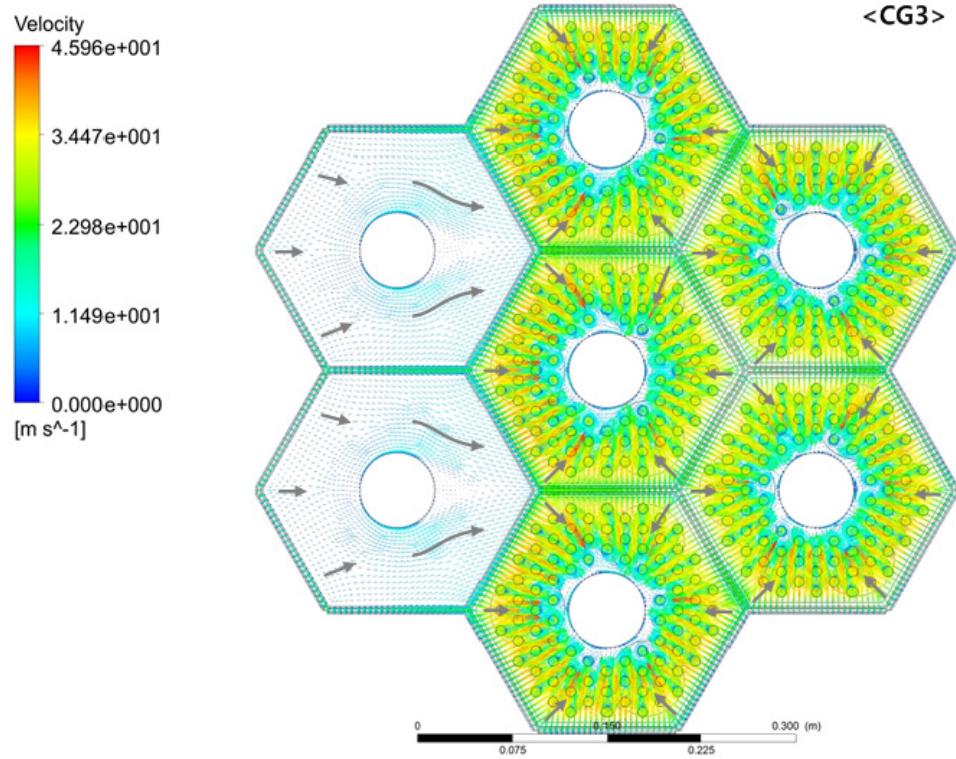
Figure 4-4. Velocity vector field on the cross section at CG3 (R2-BG6242-CG2 case).
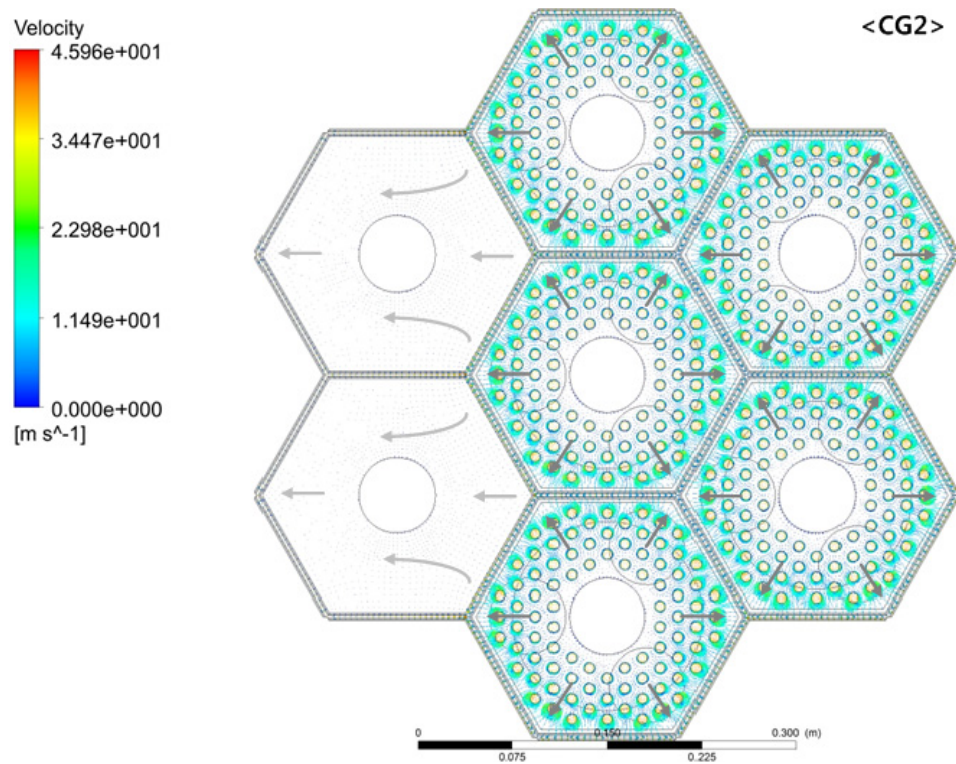
Figure 4-5. Velocity vector field on the cross section at CG2 (R2-BG6242-CG2 case).
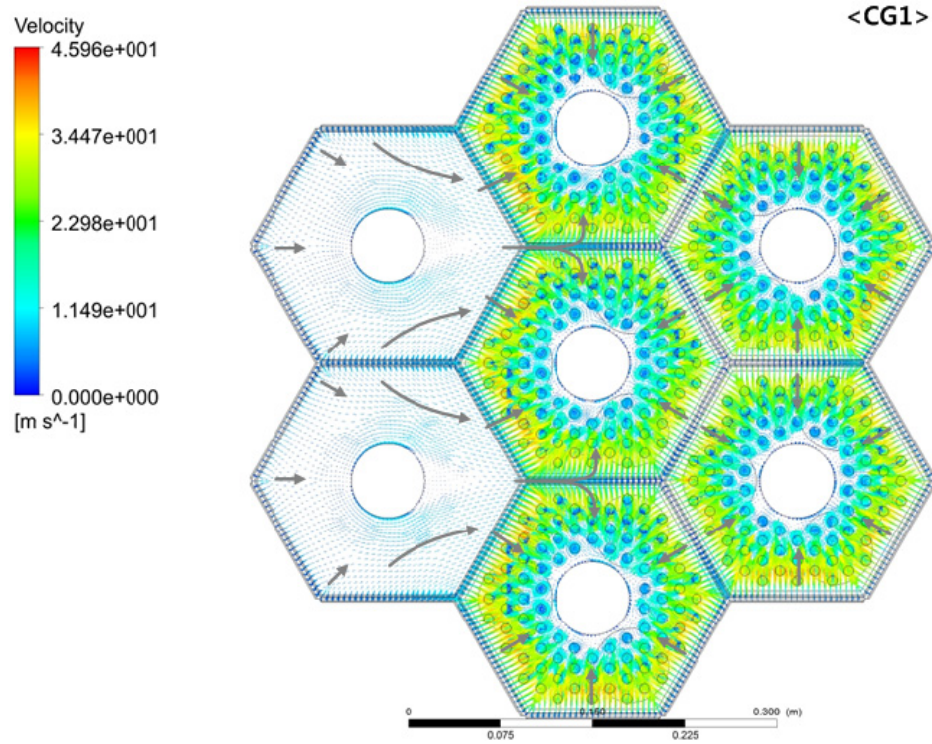
Figure 4-6. Velocity vector field on the cross section at CG1 (R2-BG6242-CG2 case).
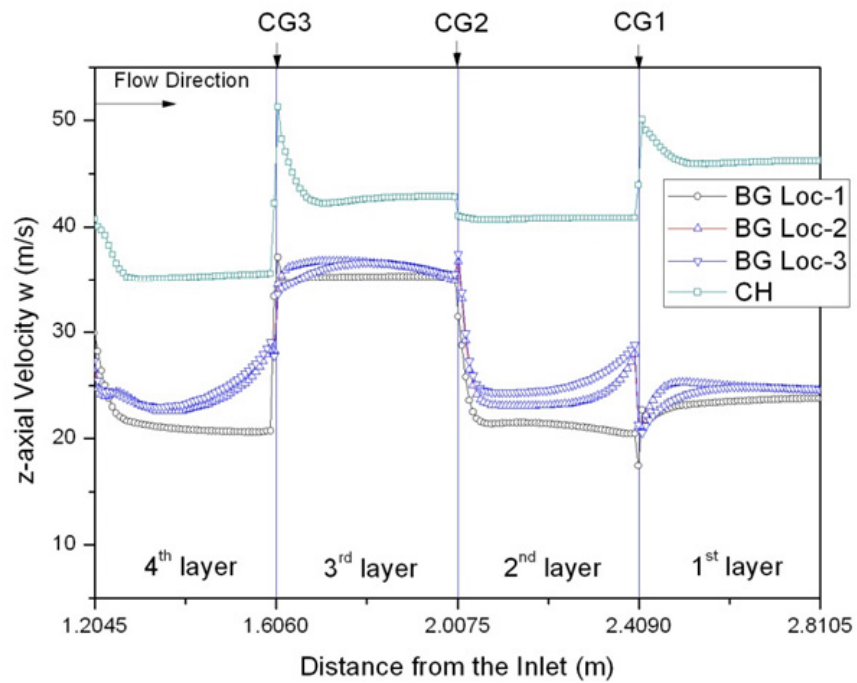
Figure 4-7. Axial velocity distributions of coolant hole and bypass gap (R2-BG6242-CG2)

27

The pressure characteristics of the bypass gap differ, depending on its location. This is caused by the cross flow and the lateral flow that pass through the block periphery from the reflector block side. Figure 4-8 shows the detailed velocity vector field on the cross section of CG1. The cross flow at Loc-2 and Loc-3, located between fuel blocks, headed bilaterally to the coolant hole, but the cross flow at Loc-1, located between the reflector and fuel block, flows in one direction from the reflector block to the fuel block. This cancelled out the effect of the velocity change at Loc-1 on the pressure distribution, which is confirmed from the z-axial velocity distribution for each channel near CG1. As shown in Figure 4-7, the axial velocity distribution at Loc-1 was definitely distinguished from those at Loc-2 and Loc-3.
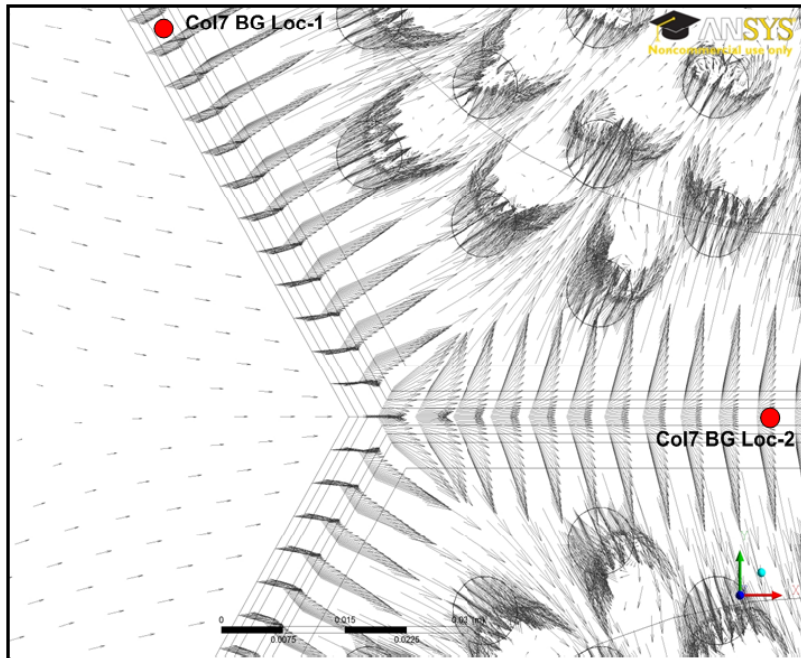
Figure 4-8. Detailed velocity vector field on the cross section at CG1 (R2-BG6242-CG2 case)

4.2   Analysis of TAMU MIR Shakedown Test Using Air

4.2.1   Air Flow Shakedown Experiments

A series of experiments were performed to quantify the flow and pressure loss characteristics of the test section. Flow rates in all flow passages were measured and checked for flow balance. The percentages of flow rate difference between the inlet flow and the flows measured at each collector and the bypass were less than 5%. The pressure losses for the preliminary hardware assembly were determined to be on the order of 1.8 kPa for the scaled test section flow rate.[7] The percentage of flow through the prismatic block cooling passages for this flow condition were on the order of 17% (of the total incoming test section flow rate) for each block. These data were used to compare to CFD calculations performed using STAR-CCM+.

4.2.2   CFD Calculation of Air Flow Shakedown Experiment

A CFD model was constructed and a detail of one of the bypass gaps is shown in Figure 4-9. Calculations performed using this CFD model, with the scaled air flow rate, are shown in Figure 4-10. The calculated percentage flow rate through the prismatic block cooling passages was 19% and the pressure loss was calculated to be 0.8 kPa. The differences between the data and calculation are being evaluated.
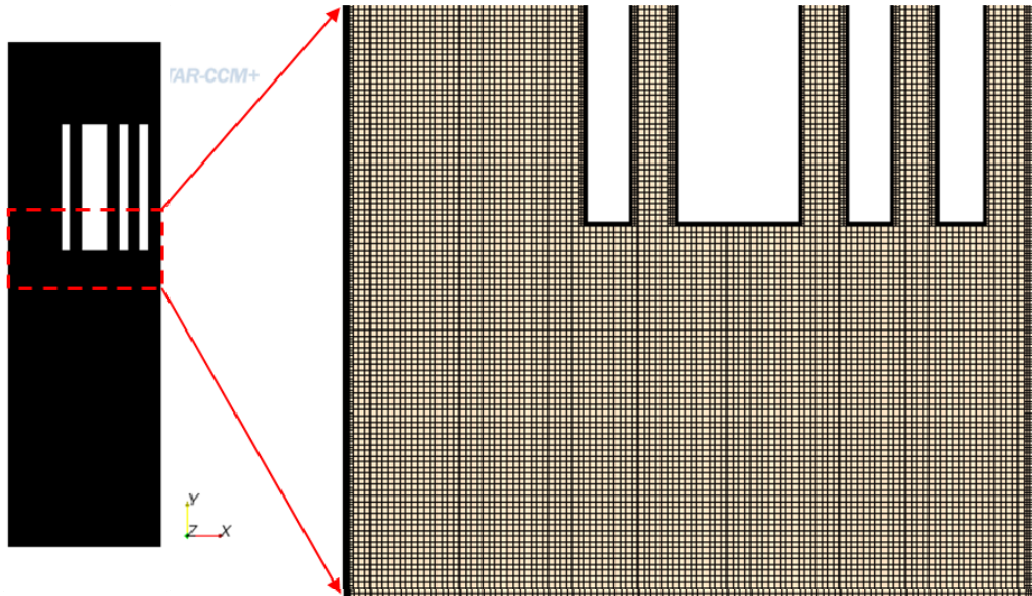
Figure 4-9. Mesh in the x-y plane showing one of the bypass gaps.
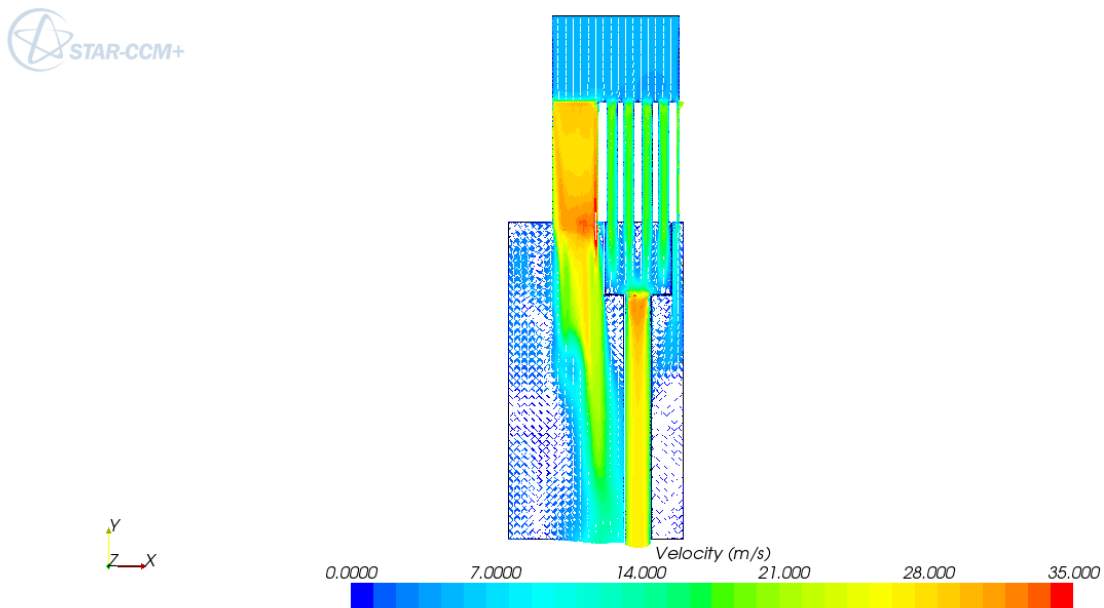
Figure 4-10. Typical velocity distributions for the x-y plane.

4.2.3   Pretest CFD Calculation Using P-Cymene Working Fluid

A pretest calculation was performed using the design working fluid for the MIR experiment at the maximum obtainable flow rate for the existing hardware: P-Cymene. The maximum Reynolds number that can be achieved for the bypass flow is 3570. The calculation is shown in Figure 4-11. These results will be used to evaluate potential modifications to the experimental hardware and to plan future experiments.
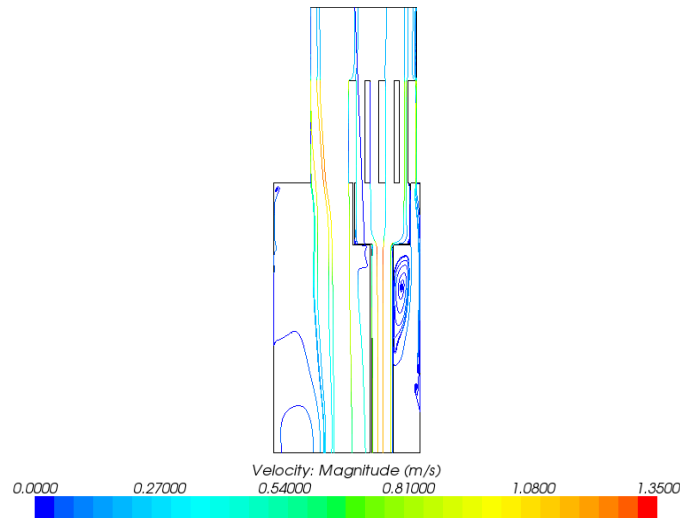
Figure 4-11. Typical velocity distribution in x-y plane with P-Cymene as working fluid.

4.2.4 Summary

The experimental hardware was constructed and shakedown experiments were performed using air as the working fluid. CFD calculations performed for the scaled air flow rate showed reasonable agreement for the flow distribution with the experimental shakedown data. CFD calculations were also performed using the MIR working fluid P-Cymene at the maximum achievable flow rate for the MIR hardware. Bypass Reynolds numbers on the order of 3570 are calculated when P-Cymene is used as the working fluid. Work is ongoing to adjust the hardware to minimize the hardware pressure losses and to lower the bypass flow rate before taking experimental data using P-Cymene. The validation experiments will be performed in the last I-NERI year and compared with the corresponding CFD calculations.

4.3 Experimental Data from INL MIR Test (INL)

A reference data set was collected consisting stereo particle image velocimeter images along the coolant channel centerlines of three coolant channels at the downstream location at the mid-level Reynolds number. A gap was not included in this reference data set. Each file consisted of 500 double images at a total flow rate into the model of about 580 l/min (approximately 153 gpm). This flow volume corresponds to a Reynolds number based on the hydraulic diameter of the coolant channels of about 2800. This data set will be used to refine image collection parameters such as the number of images required to minimize scatter in the mean velocities, camera lens size, lens f-stop setting, ratio of background intensity to particle intensity, contrast, seeding density, light sheet thickness, time between images, sampling frequency, interrogation window size (for first and subsequent passes), post-processing operations, post processing parameters, and help finalize some of the inputs to the ongoing uncertainty analysis.

Figures 4-12 to 4-17 display the results of the reference data set collection. Figures 4-12 to 4-14 describe three very similar turbulent-like mean vector field velocity profiles. Figures 4-15 to 4-17 confirm that the three velocity profiles are similar and representative of turbulent-like profiles. Of note is that the two profiles in Figures 4-16 and 4-17 are symmetrical and nearly identical, but the profile in Figure 4-15 is not as symmetrical and appears to be skewed to the right, which is toward the top of the model as oriented in the test section. With the model oriented horizontally in the test section this profile implies that buoyancy effects may be affecting the flow in this (bottom) channel. This situation will be thoroughly investigated by subsequent tests and data.
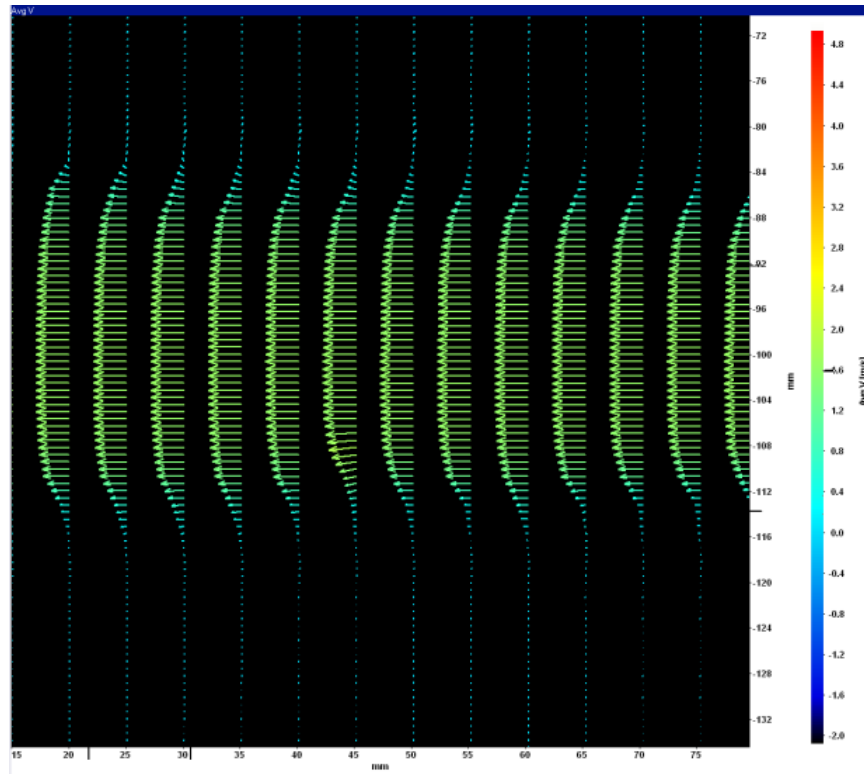
Figure 4-12. Bottom channel mean vector display.
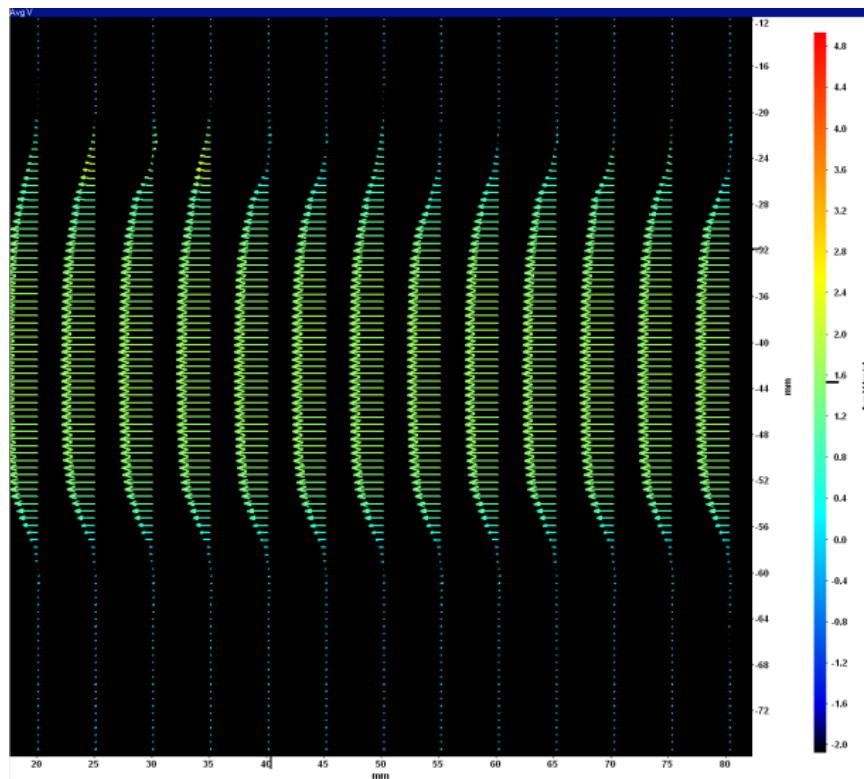
Figure 4-13. Middle channel mean vector display.
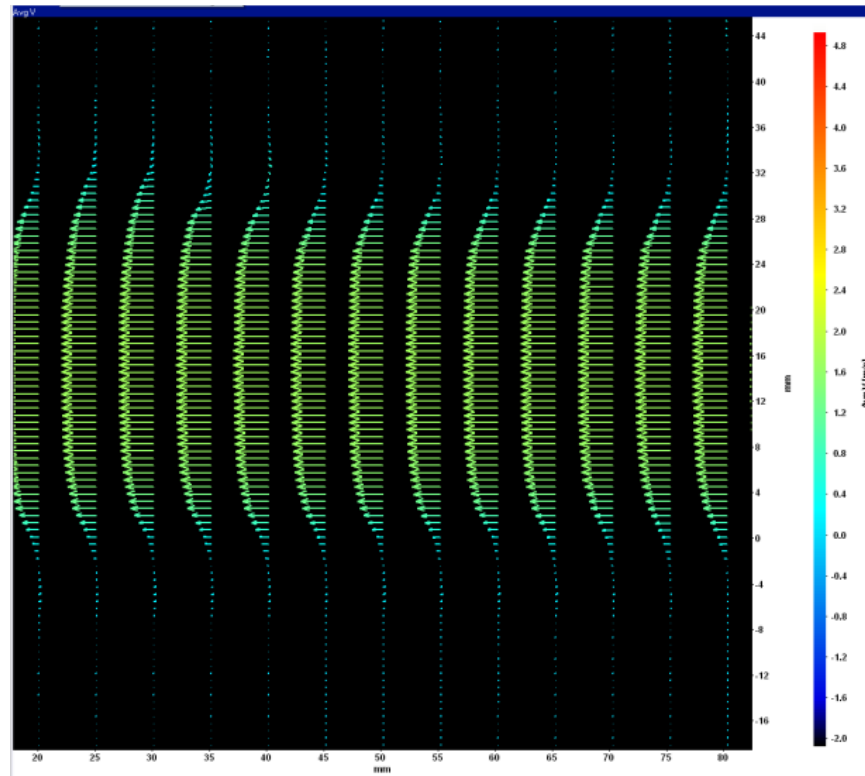
Figure 4-14. Upper channel mean vector display.
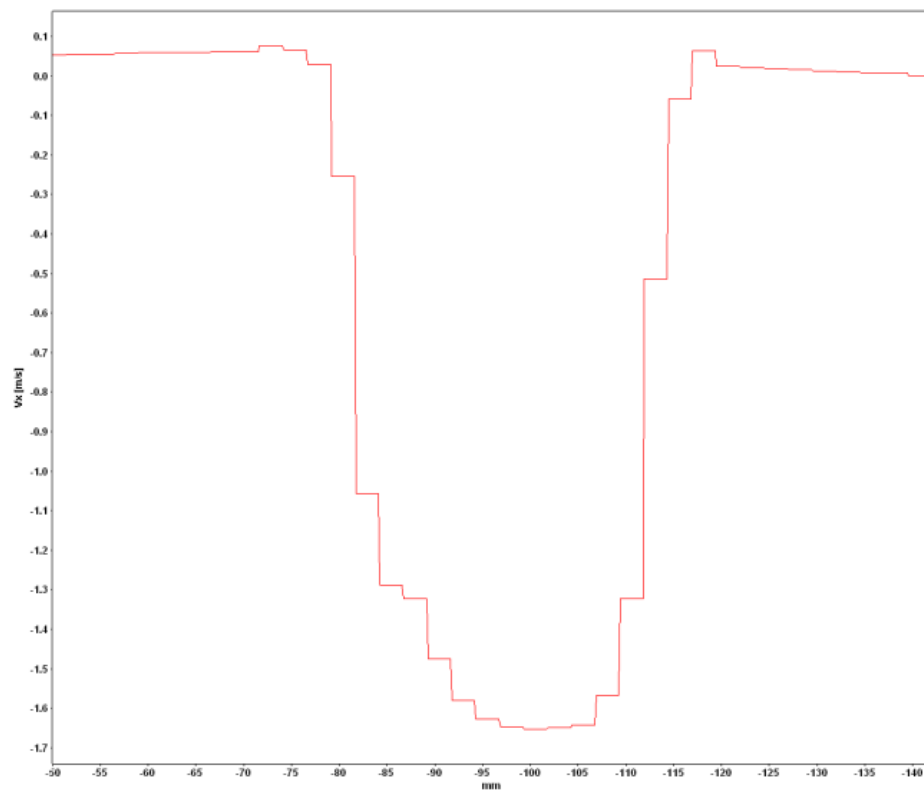
Figure 4-15. Bottom channel velocity profile.
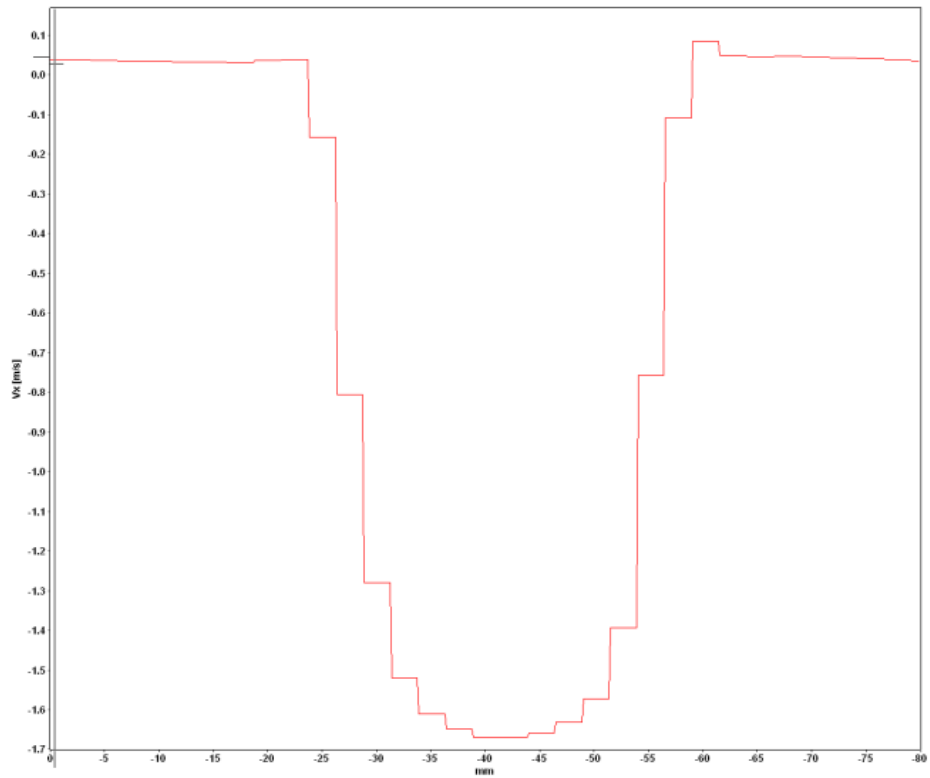
Figure 4-16. Middle channel velocity profile.
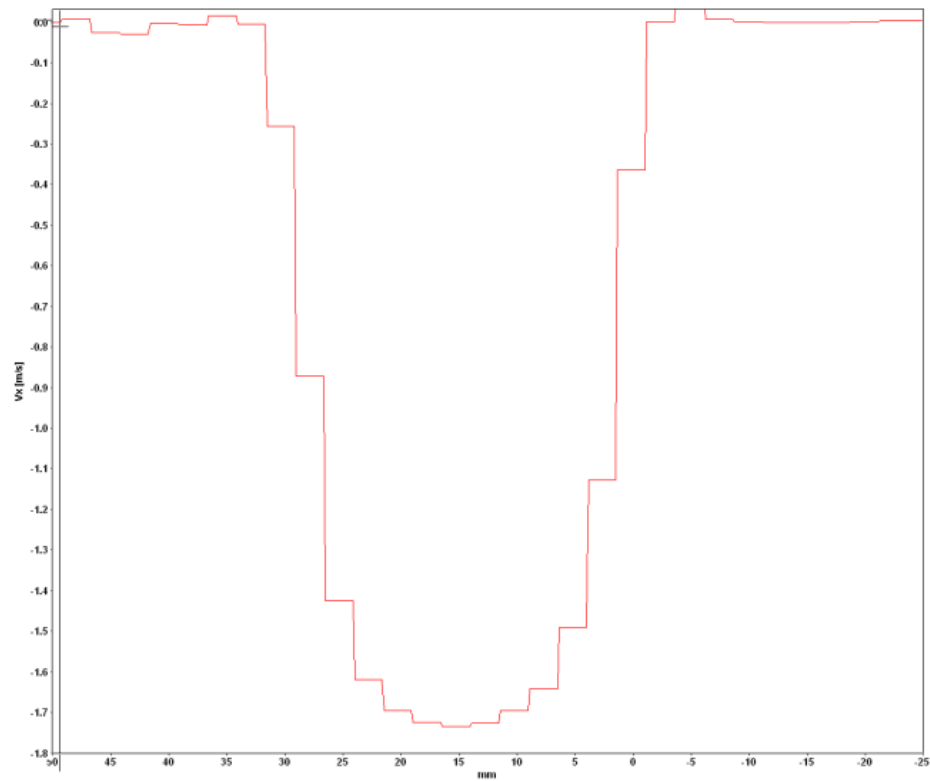
Figure 4-17. Upper channel velocity profile.

4.3.1 Summary and Action Plan

The bypass flow model and stereo particle image velocimeter systems are performing as designed and have produced a reference data set that is fundamental in refining the study parameters for collection of standard problem validation data sets. The reference data set confirms that the total hydraulic head analysis accurately predicts flow velocities and volume flow rates in the model and indicates that a Reynolds number based on a coolant channel hydraulic diameter of about 2800 is obtainable.

The results of the reference data set have been studied, and many of the study parameters have been refined. Present operations include collecting a second data set to confirm the benefit of these refinements and conduct a detailed study of the number of double images that must be recorded to minimize the scatter in the mean velocities. The reference data set has also identified several modifications to the model that will be made when the model is removed to change the axial gap size.

4.4 Experimental Data from TAMU MIR Test (TAMU)

An open-loop air flow experiment was set up to measure and estimate volume flow rates through all flow passages of the prismatic core model, which include total flow rate, flow rate through each prismatic block, and flow rates through bypass gaps. The schematic diagram of the flow loop in Figure 4-18 shows its important components and locations for velocity (V) and pressure (p) measurements.

Two sets of air flow experiments were performed for each bypass gap width of 6.10, 4.66, and 3.21 mm. A flow meter was attached to each prismatic block for the first data set so that all flow rates could be measured and estimated. This experiment suffered from high percentages of bypass flow because of large pressure losses at the flow meter connections so another data set was conducted by removing all of the flow meters. All calculation procedures were repeated by assuming that air flowed through each prismatic block equally. Bypass flow percentages were reduced, but were still higher than those occurring in the actual operation of a nuclear reactor. The Reynolds numbers of flow through the coolant channel and bypass gap were far from actual conditions.
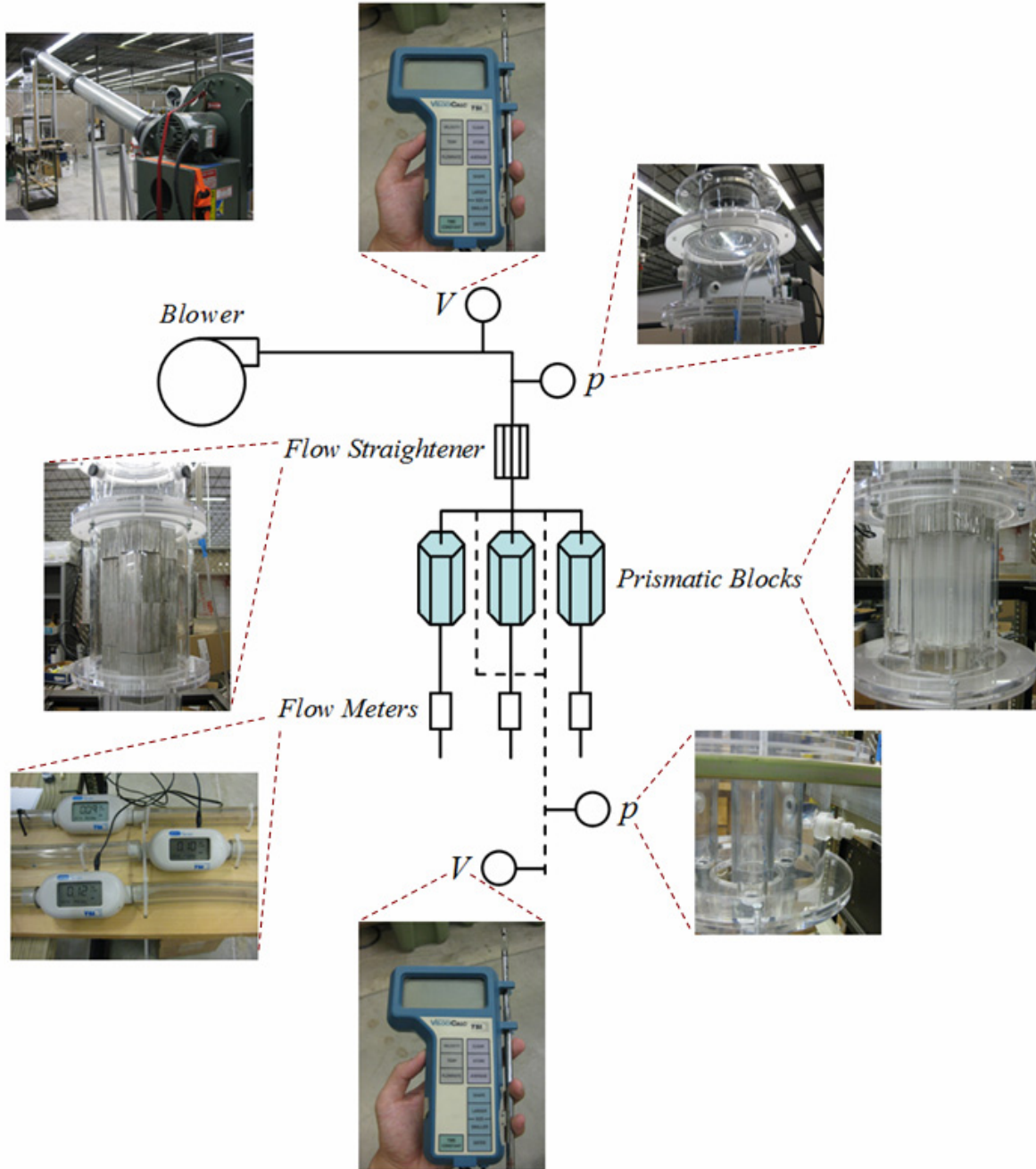
Figure 4-18. Schematic diagram of the flow loop.

4.4.1   Prismatic Core Model

Geometry of the prismatic block model used in the experiments is shown in Figure 4-19 with three important dimensions: block height (h), block side length (l) and coolant channel diameter (d). The actual sizes for these dimensions are $h = 152$ mm, $l = 50$ mm, and $d = 12.7$ mm. Flow collector at the bottom of the model that will be used to connect to flow meter is not shown here. When three prismatic blocks are arranged to form a part of reactor core, the additional dimensions to be considered are bypass gap width (b) and side gap width (s) as shown in Figure 4-20.
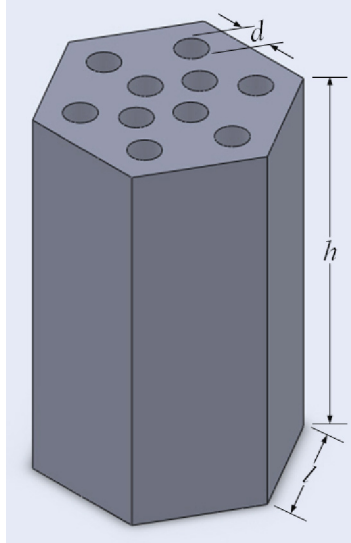
Figure 4-19. Prismatic block model.
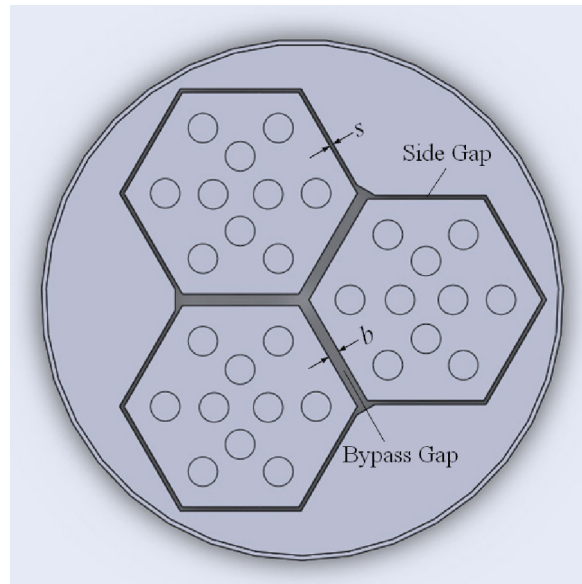
Figure 4-20. Combination of prismatic block models.

To accurately study the effect of flow through bypass gap, all side gaps are removed by attaching thin plastic plates on four walls of prismatic block models and sealing them with side walls of housing. Then, bypass gap width can be varied by attaching those plates on two remaining walls of prismatic block models. Bypass gap widths that can be attained in air flow experiments are 6.10, 4.66 and 3.21 mm. These bypass gap widths are approximated from the photos shown in Figure 4-21.

The effects of cross flow and related phenomena occur when more than one prismatic block models are stacked in one column are omitted in present study because this facility has one prismatic block model stacked in one column. Therefore, new facility design is required to make those studies to be possible.
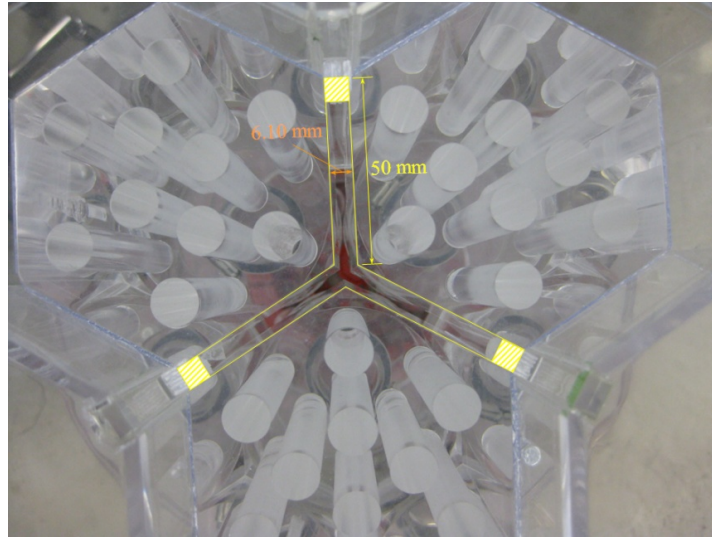
(a) 6.10 mm
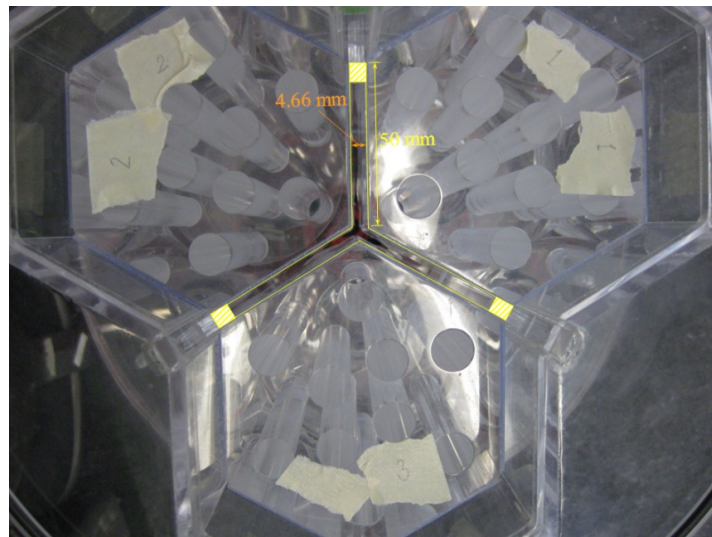
(b) 4.66 mm
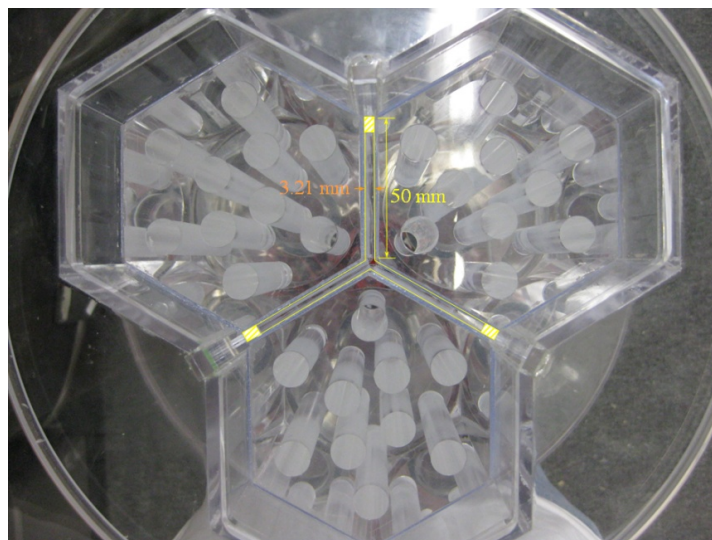
(c) 3.21 mm

Figure 4-21. Bypass gap widths of prismatic core model.

4.4.2   Raw Data from Air Flow Experiments

For the first data set when all flow meters are attached, data measured from air flow experiments is consisted of: (1) volume flow rate of flow through each prismatic block with corresponding temperature and pressure, (2) pressure drop between the location before air reaches flow straighteners and just after the exit of bypass gap, Δp, (3) the maximum velocity of air flow before it reaches flow straighteners, V_{Inlet}, and (4) the maximum velocity of air flow at the final exit of bypass flow passage, V_{Bypass}. Flow speeds in part (3) and (4) are taken at the centerline of pipe. For another data set when all flow meters are removed, data in part (1) is omitted and only data in part (2), (3), and (4) are taken.

In part (1), volume flow rate is measured in unit of l/min (liter per minute) and conversed into cfm (cubic feet per minute). Then, the corresponding temperature and pressure are used to correct the volume flow rate.

$$Volumetric\ Flow = Std\ Flow \left[\frac{273.15 + T_m}{273.15 + 21.11} \right] \left(\frac{101.3}{p_m} \right)$$

where: $Std\ Flow$ is the standard flow rate read from the 4000 Series flow meter,

T_m is the air temperature measured in unit of degree Celsius,

p_m is the absolute pressure measured in unit of kPa.

Pressure drop in part (2) is measured in mm-H_2O and converted into kPa for plotting with total flow rate in cfm. Maximum flow speeds in part (3) and (4) is taken at the centerline of the pipe and used in flow rate estimations for total inlet flow and bypass flow. Flow speeds in part (3) are taken from 8-inch-diameter pipe before air reaches flow straighteners while flow speeds in part (4) are taken from 3-inch-diameter pipe which collects air flow through all bypass gaps.

Reynolds number (Re) is estimated from average velocity (u_{av}) in each flow passage with air density (ρ) and dynamic viscosity (μ) of 1.1845 kg/m^3 and 1.8444×10^{-5} Pa·s (at 25°C). Turbulent flow regime is assumed at the beginning of calculation and Reynolds number is estimated by applying the power law for velocity profile as shown below. Under the assumption of smooth pipe ($\varepsilon = 0$), the index (n) of power law is found iteratively from the relation proposed by Nunner[8] with the aid of friction factor (f) obtained from Colebrook equation. After the iteration is ended, average velocity of flow in each pipe is known and volume flow rate can be estimated. If Reynolds number obtained from preceding assumption is lower than 2300, laminar velocity profile will be used in the calculations.

Reynolds Number:
$$Re = \frac{\rho u_{av} d_h}{\mu}$$

Velocity Profile (Laminar):
$$\frac{u}{u_{max}} = 1 - \left(\frac{r}{R} \right)^2$$

Average Velocity (Laminar):
$$\frac{u_{av}}{u_{max}} = \frac{1}{2}$$

Velocity Profile (Turbulent):
$$\frac{u}{u_{max}} = \left(1 - \frac{r}{R} \right)^{1/n}$$

Average Velocity (Turbulent):
$$\frac{u_{av}}{u_{max}} = \frac{2n^2}{(n+1)(2n+1)}$$

Relation Proposed by Nunner:
$$\frac{1}{n} = \sqrt{f}$$

Colebrook Equation:
$$\frac{1}{\sqrt{f}} = -2\log_{10}\left(\frac{\varepsilon/d_h}{3.7} + \frac{2.51}{Re\sqrt{f}}\right)$$
.

4.4.3   Air Flow Experiments when Flow Meters Attached

The comparison of total flow rates in air flow experiments with bypass gap width of 6.10, 4.66, and 3.21 mm are summarized in Table 4-7 through Table 4-9. If the result at the minimum flow rate in each case is omitted, it may be said that differences of flow rates obtained from two approaches will not exceed 10%. A large discrepancy in the low flow rate results from applying the power law for velocity profile when the Reynolds number is in transition regime (2300 to 4000). The maximum flow rates that can be attained in air flow experiments with bypass gap widths of 6.10, 4.66, and 3.21 mm are 130, 91, and 55 cfm respectively.

Table 4-7. Air flow rates when bypass gap is 6.10 mm (flow meters attached).

#	Block 1 (cfm)	Block 2 (cfm)	Block 3 (cfm)	Bypass (cfm)	Total Flow (cfm)	Inlet Flow (cfm)	Difference (%)
1	1.122	1.147	1.087	14.780	18.135	21.234	17.088
2	2.528	2.588	2.412	32.121	39.649	43.000	8.452
3	4.049	4.107	3.809	49.488	61.453	65.072	5.889
4	5.707	5.703	5.236	66.603	83.249	86.489	3.891
5	7.377	7.390	6.666	84.952	106.385	108.581	2.063
6	9.181	9.219	8.237	102.994	129.631	132.794	2.440

Table 4-8. Air flow rates when bypass gap is 4.66 mm (flow meters attached).

#	Block 1 (cfm)	Block 2 (cfm)	Block 3 (cfm)	Bypass (cfm)	Total Flow (cfm)	Inlet Flow (cfm)	Difference (%)
1	1.137	1.159	1.104	10.047	13.446	15.617	16.146
2	2.561	2.607	2.455	20.930	28.554	32.000	12.067
3	4.107	4.132	3.868	32.872	44.978	47.303	5.169
4	5.784	5.735	5.325	44.397	61.241	63.666	3.961
5	7.449	7.413	6.788	54.640	76.290	80.116	5.014
6	9.263	9.235	8.394	63.440	90.332	95.641	5.877

Table 4-9. Air flow rates when bypass gap is 3.21 mm (flow meters attached).

#	Block 1 (cfm)	Block 2 (cfm)	Block 3 (cfm)	Bypass (cfm)	Total Flow (cfm)	Inlet Flow (cfm)	Difference (%)
1	1.162	1.184	1.125	2.215	5.686	4.962	12.735
2	2.597	2.661	2.498	7.486	15.242	16.779	10.081
3	4.145	4.195	3.918	11.988	24.247	25.329	4.463
4	5.824	5.831	5.365	16.910	33.930	33.316	1.811
5	7.491	7.482	6.821	22.458	44.251	42.522	3.909
6	9.279	9.279	8.413	27.827	54.798	50.745	7.396

Because three separators are used in the experiments to prevent bowing of prismatic block models (as seen in Figure 4-16), the smallest flow area through the bypass gap that characterizes this flow is 90% of the bypass flow area. All experimental data must be modified by multipath flow analysis[9] to estimate flow rates and pressure drops when there is no separator in the test section, making the comparison between experimental data and simulation possible.

Firstly, the experimental data is assumed to be explained by the following equations:

Volume Flow Rate: $3Q_{Block} + Q_{Bypass} = Q_{Total}$

Pressure Drop: $K_{Block}Q_{Block}^2 = K_{Bypass}Q_{Bypass}^2$.

Loss coefficients (K_{Block} and K_{Bypass}) vary in proportion to A^{-2} because the change in bypass flow area is assumed to cause very small changes in friction factor. The experimental data can thus be adjusted by solving these equations simultaneously with the measured values as initial guesses.

Pressure Drop (Adjusted): $K_{Block}Q_{Block}^2 = 0.81K_{Bypass}Q_{Bypass}^2$

Percentages of bypass air flow of flow experiments in Figure 4-22 are almost constant at each bypass gap width for both the original data and estimated values. It can be concluded that the percentage of bypass flow decreases with bypass gap width (drastically decreases when bypass gap width approaches zero), depending on the flow regime through the bypass gap only. The one with a bypass gap width of 3.21 mm (the lowest width) indicates that flow through the bypass gap is laminar (as seen from the lowest data point in Figure 4-25). However, all percentages of bypass flow are much higher than those occurring in actual operation, which is less than 10%.[10]

Pressure drops measured in Part 2 at each bypass gap width are plotted in Figure 4-23 with estimated values. It is obvious that pressure drops increase at the same flow rate that bypass gap widths decrease. It is not surprising that flow in the smallest bypass flow area also increases when there are no separators in the test section, resulting in lower pressure drops than those measured from the experiment because air can flow more easily through the bypass gap. Estimated bypass flow fractions are also higher than those obtained from the experiment.

The Reynolds number of flow through the coolant channel (Re_C) and the Reynolds number of flow through the bypass gap (Re_B) based on hydraulic diameters (d_h) are calculated and plotted in Figures 4-24 and 4-25.
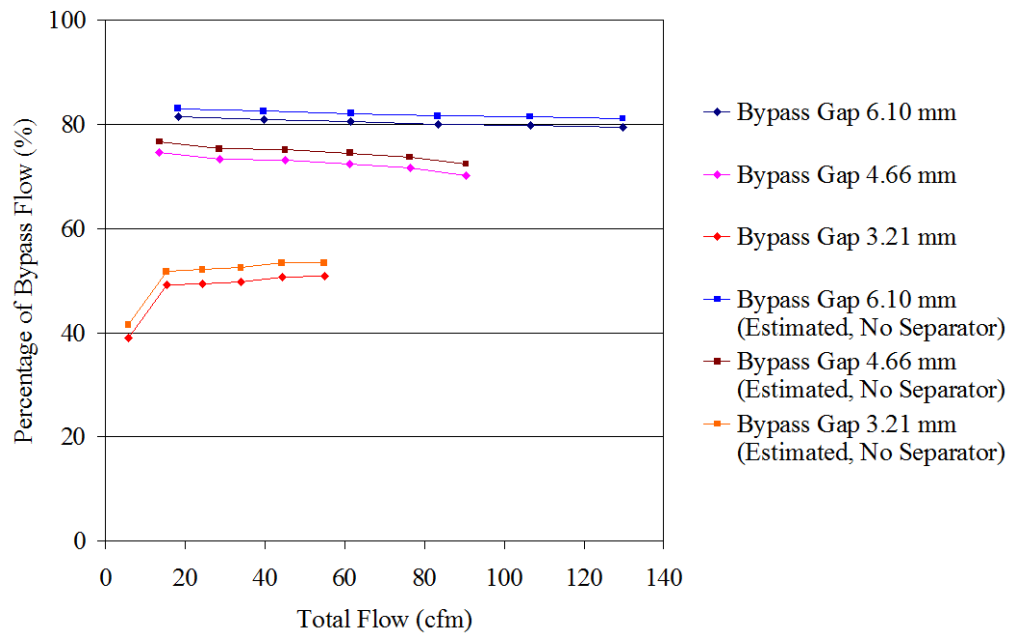
Figure 4-22. Percentages of bypass flows (flow meters attached).
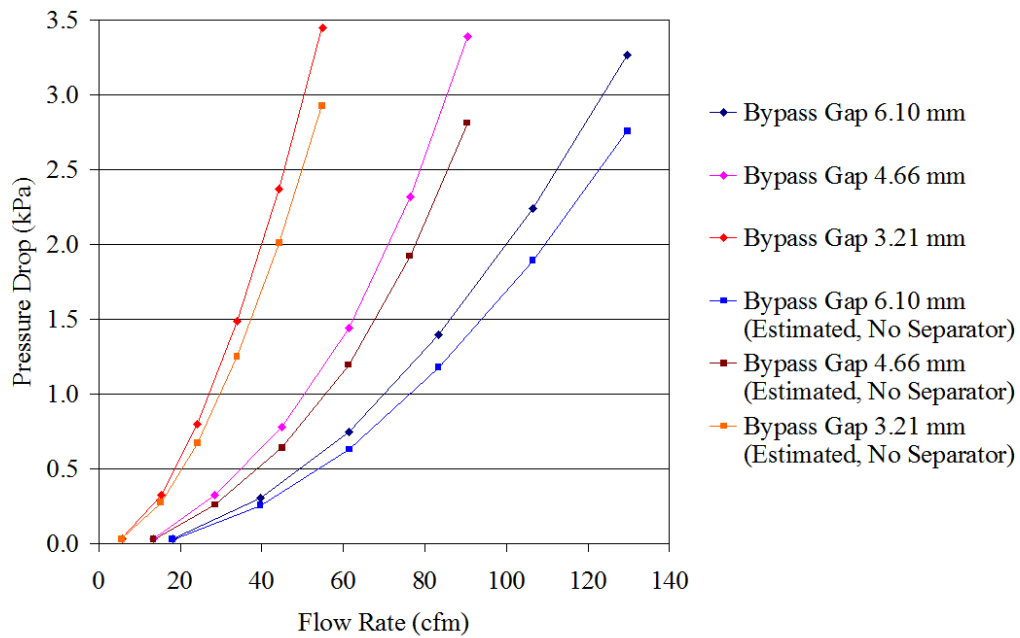
Figure 4-23. Pressure drops of bypass flows (flow meters attached).

41
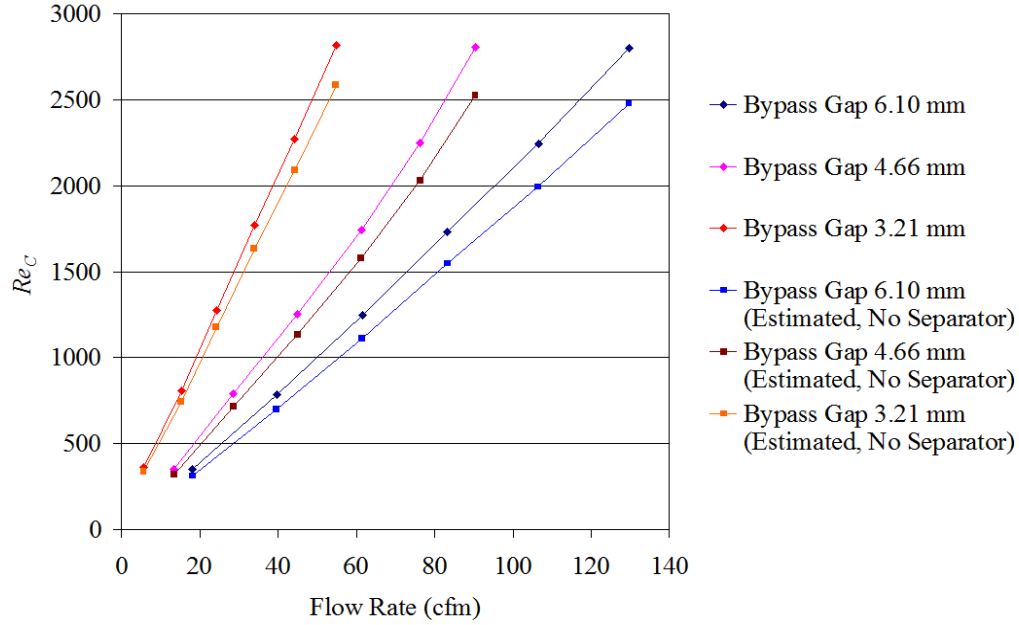
Figure 4-24. Reynolds number of flow through coolant channel (flow meters attached).
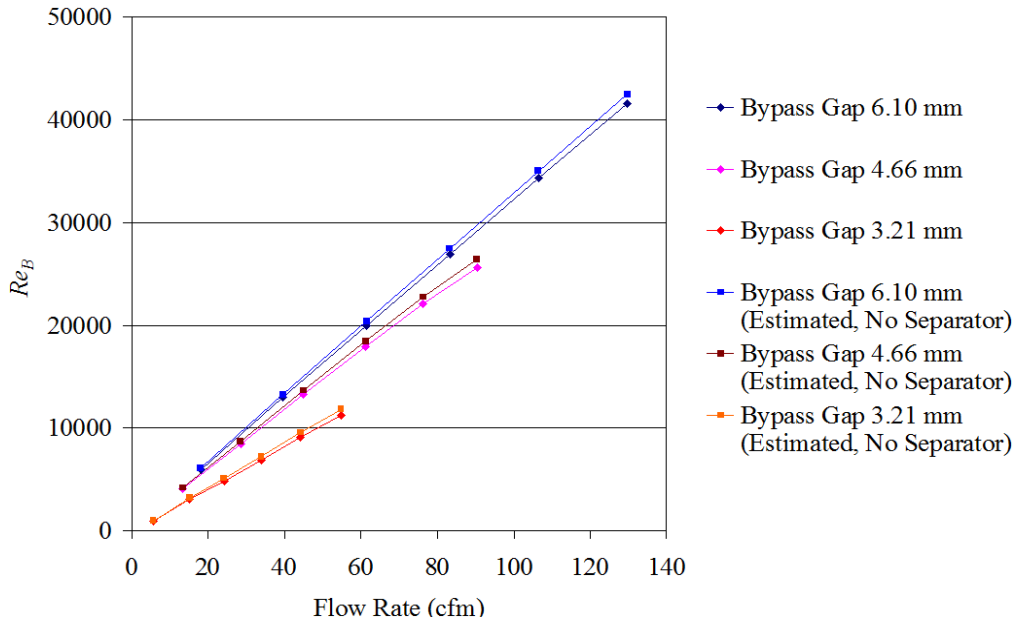
Figure 4-25. Reynolds number of flow through bypass gap (flow meters attached).

The maximum values of Re_C are almost equal at about 2800 for the original data but varied from 2500 to 2600 for the adjusted data. This indicates that bypass gap width does not affect Re_C's very much. Still, they are affected from the size and location of the coolant channel (mainly by size), which is unchanged in the present study. The maximum values of Re_B do decrease with bypass gap width because it is characterized by this. These two Reynolds numbers are far from actual conditions occurring in a reactor core (Re_C at 35000 and Re_B at 2500).

4.4.4   Air Flow Experiment when Flow Meters Removed

Another set of air flow experiments was conducted after removing the flow meter attached to the prismatic block model. In this set of experiments, the inlet flow rate estimated in Part 3 is presumed as total flow rate. After calculating the bypass flow rate from Part 4, the flow rate through each prismatic block model can be estimated by assuming that air flows through each prismatic block model equally. The flow rates in all flow passages of air flow experiments with bypass gap widths of 6.10, 4.66, and 3.21 mm are summarized in Table 4-10 through Table 4-12. The maximum flow rates that can be attained in this set of air flow experiments are 262, 229, and 191 cfm respectively.

Table 4-10. Air flow rates when bypass gap is 6.10 mm (flow meters removed).

#	Block 1 (cfm)	Block 2 (cfm)	Block 3 (cfm)	Bypass (cfm)	Total Flow (cfm)	Inlet Flow (cfm)	Difference (%)
1	9.097	9.097	9.097	13.199	–	40.491	–
2	17.223	17.223	17.223	28.911	–	80.581	–
3	24.732	24.732	24.732	45.347	–	119.543	–
4	34.602	34.602	34.602	61.335	–	165.142	–
5	45.032	45.032	45.032	78.699	–	213.796	–
6	55.328	55.328	55.328	95.460	–	261.446	–

Table 4-11. Air flow rates when bypass gap is 4.66 mm (flow meters removed).

#	Block 1 (cfm)	Block 2 (cfm)	Block 3 (cfm)	Bypass (cfm)	Total Flow (cfm)	Inlet Flow (cfm)	Difference (%)
1	9.113	9.113	9.113	9.130	–	36.470	–
2	18.490	18.490	18.490	19.286	–	74.757	–
3	26.833	26.833	26.833	30.703	–	111.202	–
4	35.917	35.917	35.917	41.883	–	149.633	–
5	45.921	45.921	45.921	51.777	–	189.540	–
6	56.131	56.131	56.131	60.473	–	228.867	–

Table 4-12. Air flow rates when bypass gap is 3.21 mm (flow meters removed).

#	Block 1 (cfm)	Block 2 (cfm)	Block 3 (cfm)	Bypass (cfm)	Total Flow (cfm)	Inlet Flow (cfm)	Difference (%)
1	9.530	9.530	9.530	1.773	–	30.364	–
2	18.666	18.666	18.666	6.651	–	62.649	–
3	27.332	27.332	27.332	10.945	–	92.941	–
4	35.770	35.770	35.770	15.478	–	122.787	–
5	45.338	45.338	45.338	20.687	–	156.701	–
6	54.967	54.967	54.967	25.665	–	190.566	–

All data in this set is adjusted in the same way as in the former set. Percentages of bypass flow in Figure 4-26 are almost constant at each bypass gap width for both the original data and estimated values. The same conclusions can be drawn—percentage of bypass flow decreases with bypass gap width, depending on the flow regime through the bypass gap only. The lowest one in the air flow experiment with the bypass gap width of 3.21 mm indicates that flow through the bypass gap is laminar (as seen from the lowest data point in Figure 4-29). Although percentages of bypass flow are still higher than actual conditions, their decrease in this experiment suggests the need for a new facility design to avoid area reduction of flow through the passage connected from the prismatic block model.
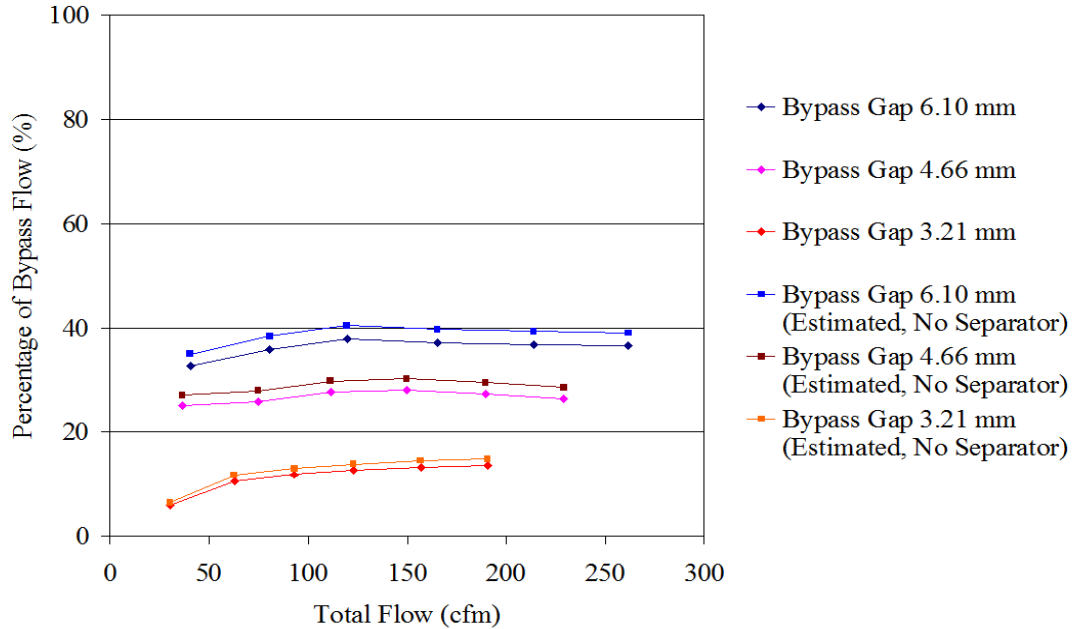
Figure 4-26. Percentages of bypass flows (flow meters removed).

Pressure drops measured in Part 2 at each bypass gap width are plotted in Figure 4-27 with estimated pressure drops. The plot shows that pressure drop increases at the same flow rate as the bypass gap width decreases, but the flow rate is less than that in air flow experiments when flow meters are attached.

Based on hydraulic diameters (d_h), the Reynolds number of flow through the coolant channel (Re_C) and through the bypass gap (Re_B) are calculated and plotted in Figure 4-28 and Figure 4-29.

The maximum values of Re_C are almost equal at about 17000 for all bypass gap widths and the same conclusions can be drawn as in the preceding set of experiments. The maximum values of Re_B are decreased with bypass gap width because it is characterized by bypass gap width. Although these Reynolds numbers are still far from actual reactor core conditions, their values in this set of experiments, which show a better trend and guide for the a new facility design, can be drawn as stated above.
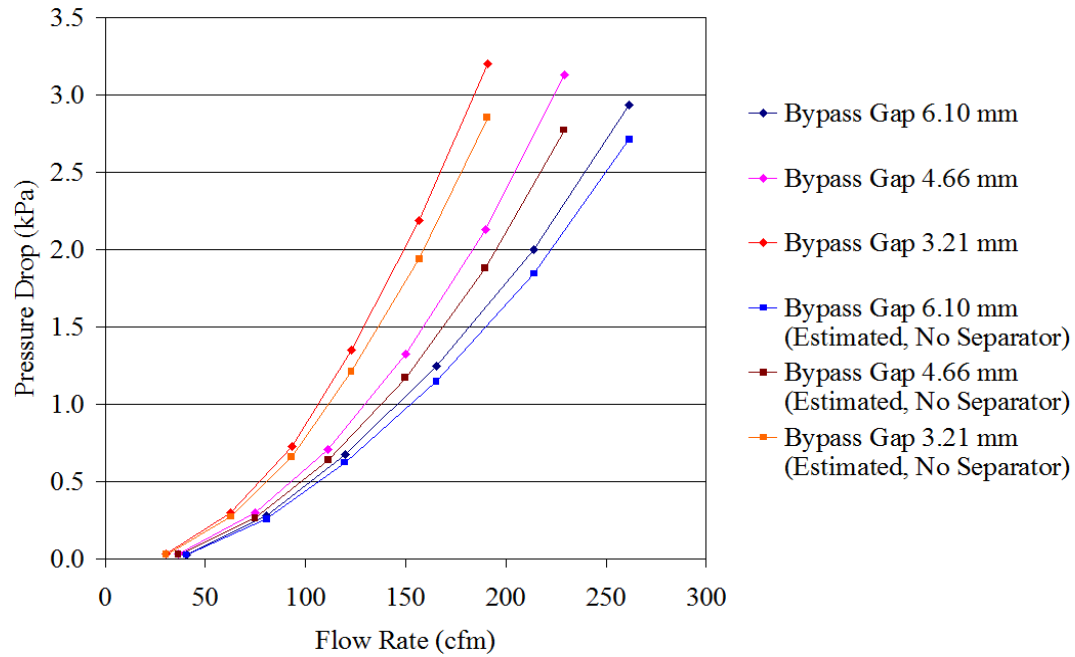
Figure 4-27. Pressure drops of bypass flows (flow meters removed).
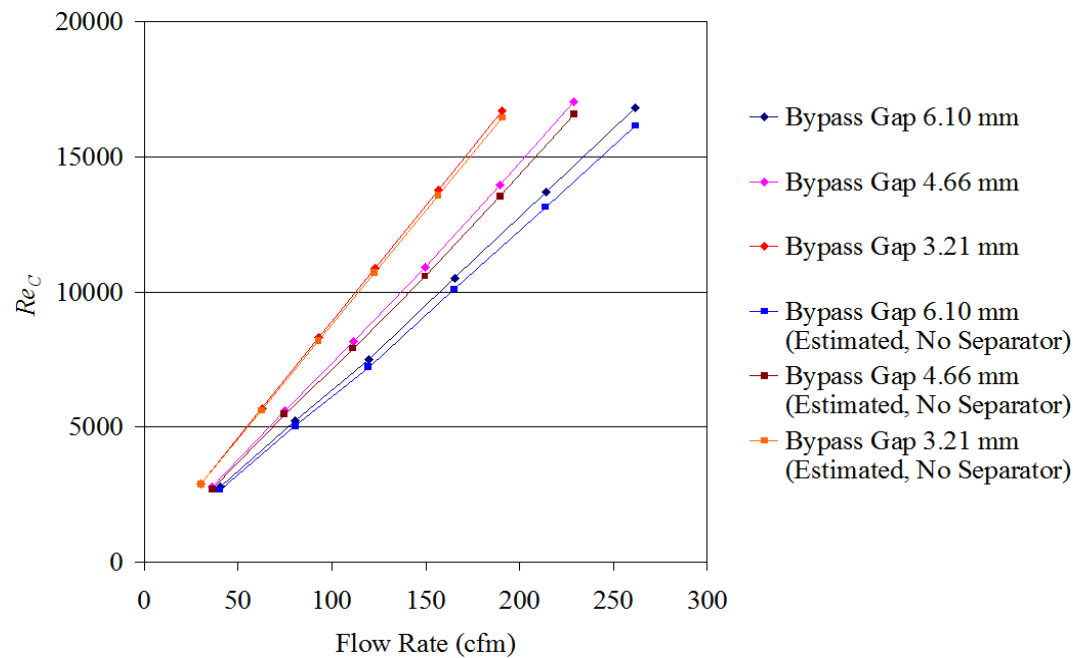
Figure 4-28. Reynolds number of flow through coolant channel (flow meters removed).
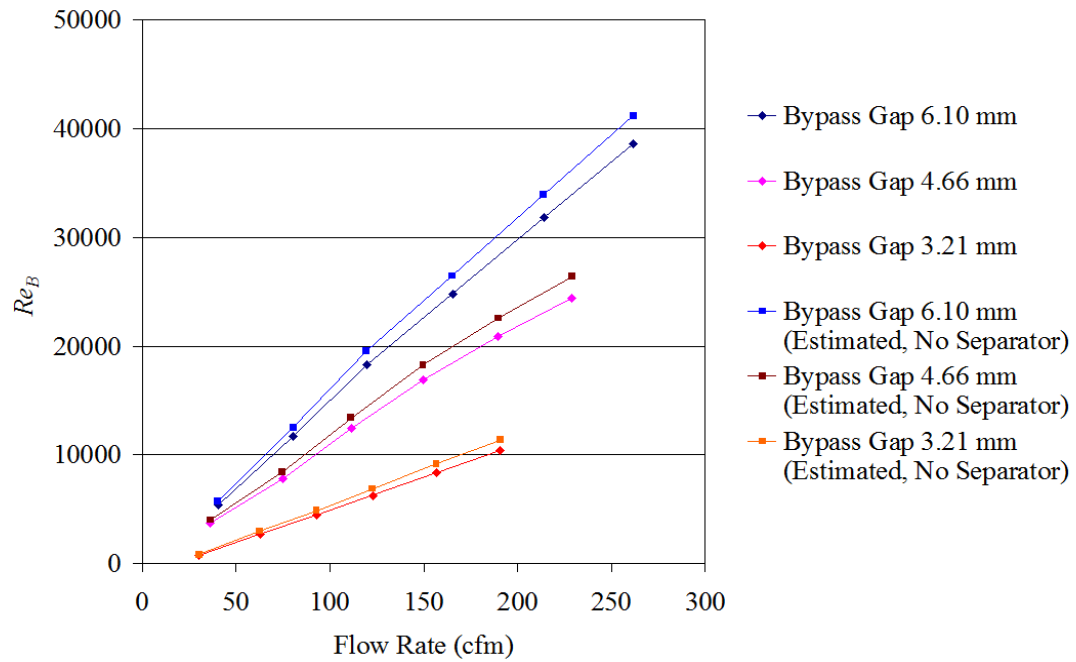
Figure 4-29. Reynolds number of flow through bypass gap (flow meters removed).

4. Planned activities

    None

5. Issues/concerns

    None

5.   TASK 4

1. Task title and responsible lead:

   Validation and Improvement of Thermofluid Analysis Tools, ANL/KAERI

2. Brief description of objectives:

   Validate and improve the existing thermofluid analysis tools, including both system-level and CFD codes. Integrate and enhance GAS-NET code by ANL before the validation. Apply GAMMA+ code by KAERI for the flow network analysis. Develop detailed CFD models for each experiment and perform benchmark calculations.

3. Task technical status overview:

   Benchmark calculations were performed to investigate the performance of GAMMA+ for a simple multiblock experiment. CFD analyses were carried out to compensate for the lack of data for the comparison in the experiment. A detailed comparison was made between CFD and GAMMA+ results to identify major phenomena overlooked in the GAMMA+ model. Some improvement of the GAMMA+ code has been made to improve the prediction of flow characteristic in bypass and cross-flow regions. Core hot spot analyses considering the gap size distributions obtained in Task 2 were carried out by the GAMMA+ code with improved models. CFD benchmark analyses for MIR tests were performed by KAERI and INL and code-to-code comparison were made.

5.1   Benchmark Calculation for a Simple Multiblock Experiment (KAERI)

The test section of the experiment[11] shown in Figure 5-1 consists of three layer and 11 columns of acryl blocks. Each layer includes three hexagonal blocks in the middle row, on each side of which are located two pentagonal and two rectangular blocks. Most of the air flow coming from the inlet supplies into the channels, which is provided in the block to mimic the coolant channel, discharges at the channel outlet through mixing chambers. The other flow enters into uniform bypass gaps of 2 mm between the blocks and discharges at the bypass outlet. Two different block arrangements were selected. One was three rows of channel blocks designated by F3 whereas the other was one row of channel blocks and two rows of nonchannel blocks by F1. Cross flow gap of 2 mm, designated by CG2, was used, but zero of the gap was also considered for the F3 case. Data for pressure distribution were only measured along the line BG1 and BG2.

Figure 5-2 shows the GAMMA+ analysis model. To model all flow paths in the simple multiblock experiment, flow channels in the blocks were rotated to be connected to corresponding gap channels. Pressure drop along the block and gap channel was modeled by the Haaland formula with the Reynolds number based on hydraulic diameter. The effect of the cross flow loss factor was considered by Kaburaki's correlation. The loss models or coefficients considered are listed in Table 5-1.

The bypass flow fractions are compared in Table 5-2. The analysis result for F3CG2 and F1CG2 cases shows a relatively high fraction of bypass flow when compared with experimental data. However, the F3CG0 case shows higher bypass flow in the experiment. It is conjectured that the fully closed cross-flow gap might not be realized in the experiment. In other words, there would be a leak through the cross-flow gap.

47
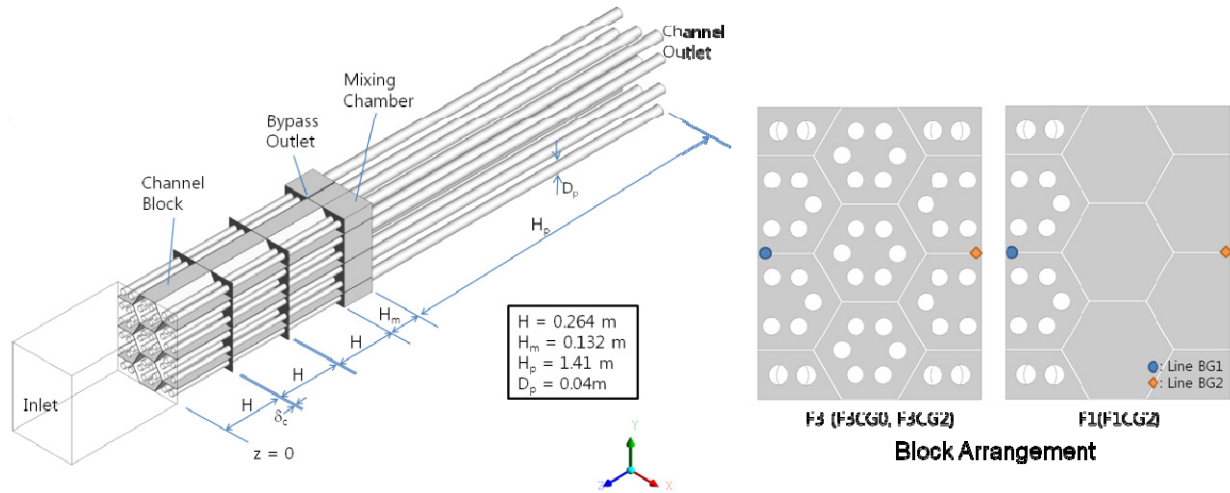
Figure 5-1. Layout of simple multiblock experiment.
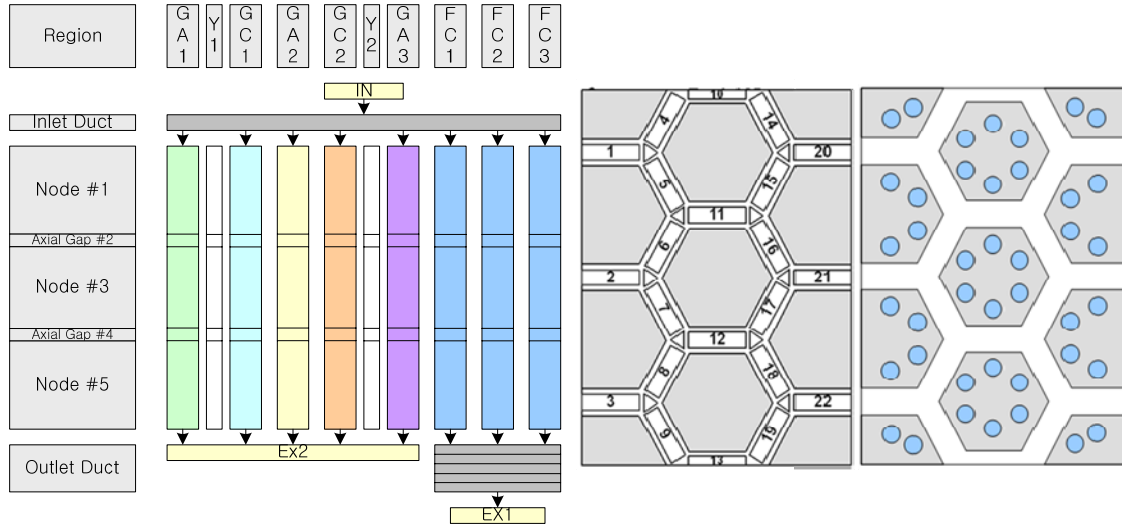
Figure 5-2. GAMMA+ analysis model for a simple multiblock benchmark.

Table 5-1. Pressure loss model used in the GAMMA+ analysis.

Regions	Pressure loss coefficient	Remarks
Channels	$$\sqrt{1/f} = -1.8\log\left[\frac{6.9}{\text{Re}} + \left(\frac{\varepsilon/D}{3.7}\right)^{1.11}\right]$$	Haaland formula
Abrupt area change	$$K = \left(1 - \frac{\varepsilon_s}{\varepsilon_c \varepsilon_t}\right)^2$$ $$\varepsilon_c = 0.62 + 0.38\varepsilon_t^3, \ \varepsilon_t = A_j/A_{up}$$	$\varepsilon_s = A_{dn}/A_{up}$ (contraction) $\varepsilon_s = A_{up}/A_{dn}$ (expansion)
Lateral flow loss	K = 0.38	Idelchick's Handbook
Cross flow model	K = C1/(□Re) +C2	Kaburaki's model

48

Table 5-2. Comparison of bypass flow fraction.

Case	Inlet Flow Rate (kg/s)	Bypass Flow(%)		
		Exp.	CFX	GAMMA+
F3CG0	0.4226	13.39	12.01	12.42
F3CG2	0.4179	13.35	14.19	14.12
F1CG2	0.1775	29.69	30.02	29.99

Figure 5-3 shows pressure distributions along the BG1 line with the CFD velocity distribution at the second cross-flow gap. The CFX and GAMMA+ results show a good agreement with the experiment, except for the region after the abrupt pressure drop across the cross-flow gap between the second and third blocks. It is seen from the velocity distribution that the cross flow from the block channels merges into the bypass flow at the BG1 line, which results in a steep pressure drop because of a blockage effect by the flow direction change at the merging location that was not properly modeled in the GAMMA+ analyses.
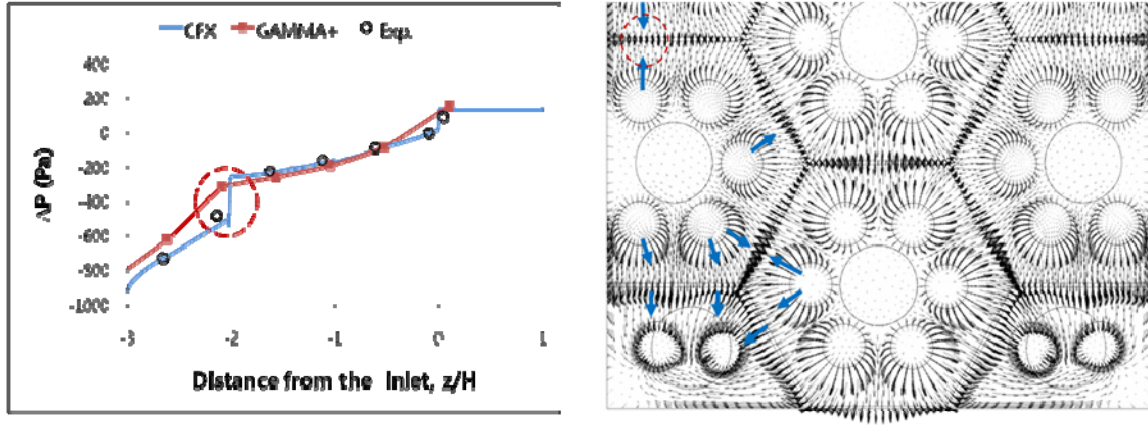
Figure 5-3. Pressure distribution along the line BG1 and velocity vector plot on the plane of the second cross-flow gap for the F3CG2 case.

5.2 Model Improvement of GAMMA+ Code (KAERI)

5.2.1 Heat Conduction Model

A heat conduction model to calculate the temperature profile in tristructural isotropic (TRISO) particles dispersed within a fuel matrix, implicit coupling for the consideration of heat exchange between a fuel matrix and coated TRISO particles, an improved multi-D heat conduction model considering sub-meshes with hexagonal fuel and reflector blocks.

$$\left(\rho C_p\right)_p \frac{\partial T_p}{\partial t} = \frac{1}{r^2} \frac{\partial}{\partial r}\left(r^2 \lambda_p \frac{\partial T_p}{\partial r}\right) + \dot{q}_N'' - \dot{q}_{pf}''' \quad \text{(TRISO particle)}$$

$$\varphi_f \left(\rho C_p\right)_f \frac{\partial T_f}{\partial t} = \frac{1}{r} \frac{\partial}{\partial r}\left(r \lambda_f \frac{\partial T_f}{\partial r}\right) + \dot{q}_{pf}''' - \dot{q}_{gf}''' \quad \text{(Fuel compact)}$$

$$\varphi_s \varphi_f \left(\rho C_p\right)_g \frac{\partial T_g}{\partial t} = \frac{\partial}{\partial x_i}\left(\lambda_{eff} \frac{\partial T_g}{\partial x_i}\right) + \dot{q}_{gf}''' - \dot{q}_{sf}''' \quad \text{(Fuel/reflector blocks)}$$

49

where φ_s, φ_g and φ_f are volume fractions of solid, graphite and fuel. The underlined heat exchange terms between a particle and a fuel ($\dot{q}'''_{pf}$) and a fuel and a graphite block ($\dot{q}'''_{gf}$), are evaluated at new time step in an implicit-coupled way.

5.2.2   Multi-channel Flow Model

The flow pattern in the bypass gap represents the 2-D flow distribution. The multichannel flow model has been developed for this purpose. The 1-D flow network model was modified by including the convective and viscous terms. The normal junction momentum is used at the flow paths in the vertical direction, and the cross junction momentum is used at the flow paths in the lateral direction.

Normal Junction Momentm:

$$\rho\left(\frac{\partial V_z}{\partial t} + V_x\frac{\partial V_z}{\partial x} + V_z\frac{\partial V_z}{\partial z}\right) = -\frac{\partial P}{\partial z} - \rho f|V_z|V_z + \rho g_z + \frac{\partial}{\partial x}\left[\mu\left(\frac{\partial V_z}{\partial x} + \frac{\partial V_x}{\partial z}\right)\right] + 2\frac{\partial}{\partial z}\left(\mu\frac{\partial V_z}{\partial z}\right)$$

Cross Junction Momentum:

$$\rho\left(\frac{\partial V_x}{\partial t} + V_x\frac{\partial V_x}{\partial x} + V_z\frac{\partial V_x}{\partial z}\right) = -\frac{\partial P}{\partial x} - \rho f|V_x|V_x + 2\frac{\partial}{\partial x}\left(\mu\frac{\partial V_x}{\partial x}\right) + \frac{\partial}{\partial z}\left[\mu\left(\frac{\partial V_z}{\partial x} + \frac{\partial V_x}{\partial z}\right)\right]$$

Figure 5-4 shows the conceptual test results of the multichannel flow model for the 2-D flow distribution. The multichannel flow model improves the 1-D flow network model and follows the 3-D calculation result using GAMMA+ 3-D modeling feature. Meanwhile, the 2-D calculation model without the friction loss term (second term in the right side of the above equations) is not adequate in this application because the bypass gap flow channel is confined between the graphite blocks (wall boundaries).
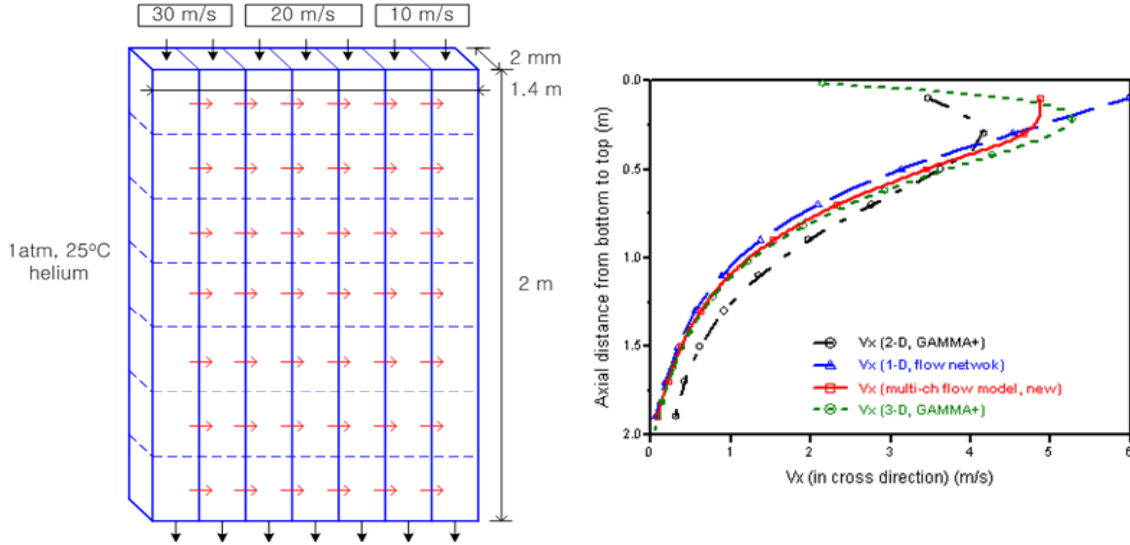
Figure 5-4. 2-D flow distribution test of the multichannel flow model.

5.2.3   Wye Converging/Diverging Form Loss

The form loss for diverging and converging wye is taken from Idelchik's handbook.[12] The form loss for the converging wye is evaluated as follows:

$$K_{loss} = 1 + Q_{rat}^2 - Q_{rat}^2 \frac{1 + Q_{rat}}{(0.75 + 0.25Q_{rat})^2}$$

$$Q_{rat} = Q_{st,1}/Q_{st,2} \;,\; Q_{st,2} = Q_{side} + Q_{st,1}$$

where the subscripts 1 and 2 indicate the upstream and downstream locations of the straight passage. For diverging wye, the form loss is evaluated as follows:

$$K_{loss} = fcn(Q_{rat}, A_{rat})$$

Q_{rat}										
0	0.1	0.2	0.3	0.4	0.5	0.6	0.7	0.8	0.9	1.0
$A_{rat} \leq 0.4$										
0	0.004	0.016	0.036	0.064	0.1	0.144	0.196	0.256	0.324	0.40
$A_{rat} > 0.4$										
0	-0.016	-0.048	-0.072	-0.064	0	0.21	0.059	0.115	0.194	0.30

where $Q_{rat} = \dfrac{Q_{side}}{Q_{st,2}}$, $Q_{side} = Q_{st,2} - Q_{st,1}$, and $A_{rat} = \dfrac{A_{side}}{A_{st,2}}$.

5.2.4 Suitability of Kaburaki's Correlation

Kaburaki's correlation for cross flow was obtained from specific block and hole sizes as shown in Figure 5-5. It is necessary to confirm whether or not the correlation is suitable for the multihole fuel blocks used in PMR200 or MHTGR core.

The number constants of nondimensional K-loss are obtained from the Kaburaki's correlation by multiplying the gap opening area (A).

$$K = A^2 \left(\frac{c_1}{\delta \, \text{Re}} + c_2 \right) / \delta^2 = \frac{C_1}{\delta \, \text{Re}} + C_2 \, .$$

When applying gap-opening area and gap size(δ), the constants C_1 and C_2 converge to limiting values by increasing the number of holes and decreasing the hole size as shown in Table 5-3. In addition, the amount of cross flow is largely dependent on the difference of pressure drop between the bypass gap and the coolant channel. Therefore, the Kaburaki's correlation for Type III can be selected as cross flow correlation for the multihole fuel block.
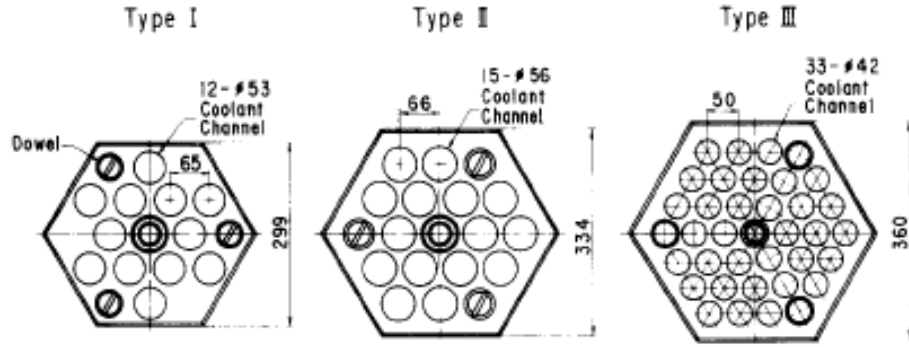
Figure 5-5. Tested block models in the Kaburaki's correlation.

Table 5-3. Constants for nondimensional Kaburaki's correlation.

Parallel gap	Type I	Type II	Type III
C1	0.722	1.207	1.215
C2	3.37	2.68	2.65

5.3 GAMMA+ Analysis for SNU Multi-block Air Test (KAERI)

5.3.1 Simple Multiblock Analysis

As described above, the wye converging/diverging form loss model was incorporated in the new version of the GAMMA+ code. In order to examine the effect of the new model, GAMMA+ calculations were carried out for the simple multiblock experiment. Figure 5-6 shows the results for the case with the cross-flow gap of 2 mm (F3CG2). Without the new model, the GAMMA+ code under-predicts the sudden pressure drop across the last cross-flow gap where a large cross flow occurs. However, it can be clearly seen that the improvement in the GAMMA+ prediction is achieved with the new model.
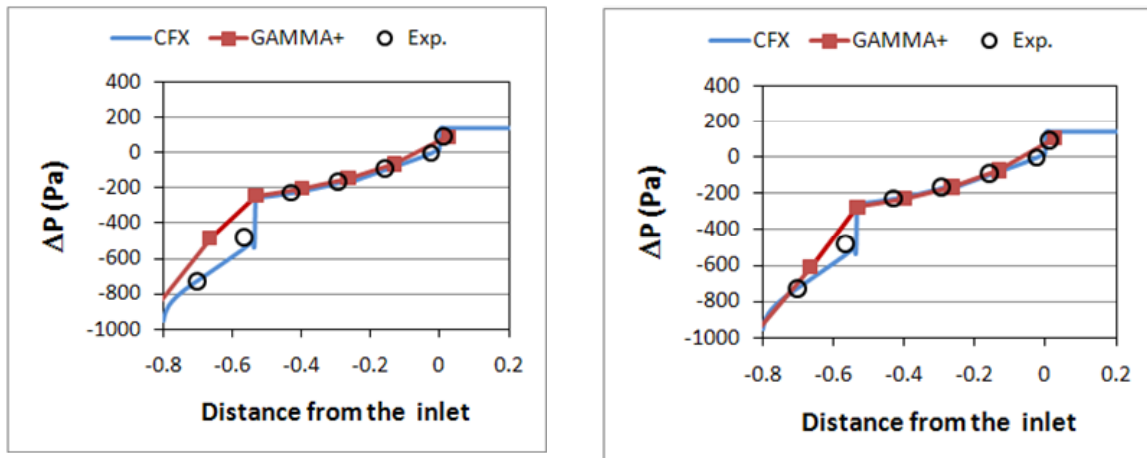
(a) Without the new model   (b) With the new model

Figure 5-6. The effect of the improved model with wye converging/diverging form loss.

5.3.2 SNU Air Test Analysis

The SNU multiblock air experiment performed under the present I-NERI project was analyzed with the GAMMA+ code. Figure 5-7 shows the GAMMA+ model for the analysis. The inlet/outlet flow

measurement ducts, the test block coolant channels, the bypass gap channels, the cross-flow gaps, the bottom transition blocks, and the outlet plenum/pipe are precisely modeled. Lateral flows around the hexagonal test blocks and the cross flows between the coolant channels and the bypass gaps are modeled as well. The 90 coolant channels in the block were grouped into six channels. The total numbers of fluid cells and junctions were 580 and 65 respectively. Table 5-4 shows the comparison of the predicted and measured bypass fractions for the four test cases. The overall agreement is founded to be good. GAMMA+ under-predicts the bypass flow at the inlet in the cases of the axially variant gaps with the cross flows R2BG6242-CG2 and R2BG62420-CG2. However, as shown in Figure 5-8, the GAMMA+ well predicts the pressure distributions for such cases. It is therefore concluded that the GAMMA+ model for the bypass gap flow in a prismatic core is reasonably good.

Table 5-4. Comparison of the predicted and measured bypass flow fractions.

Case	Inlet Flow Rate (kg/s)	Inlet Bypass Flow (%)		Outlet Bypass Flow (%)	
		Exp.	GAMMA+	Exp.	GAMMA+
R2-BG2-CG0	1.234	19.7	19.3	16.8	19.3
R2-BG6-CG0	1.197	50.4	50.1	49.6	50.1
R2-BG6242-CG2	1.221	39.1	33.0	22.4	21.8
R2-BG62420-CG2	1.109	36.8	31.0	2.2	0
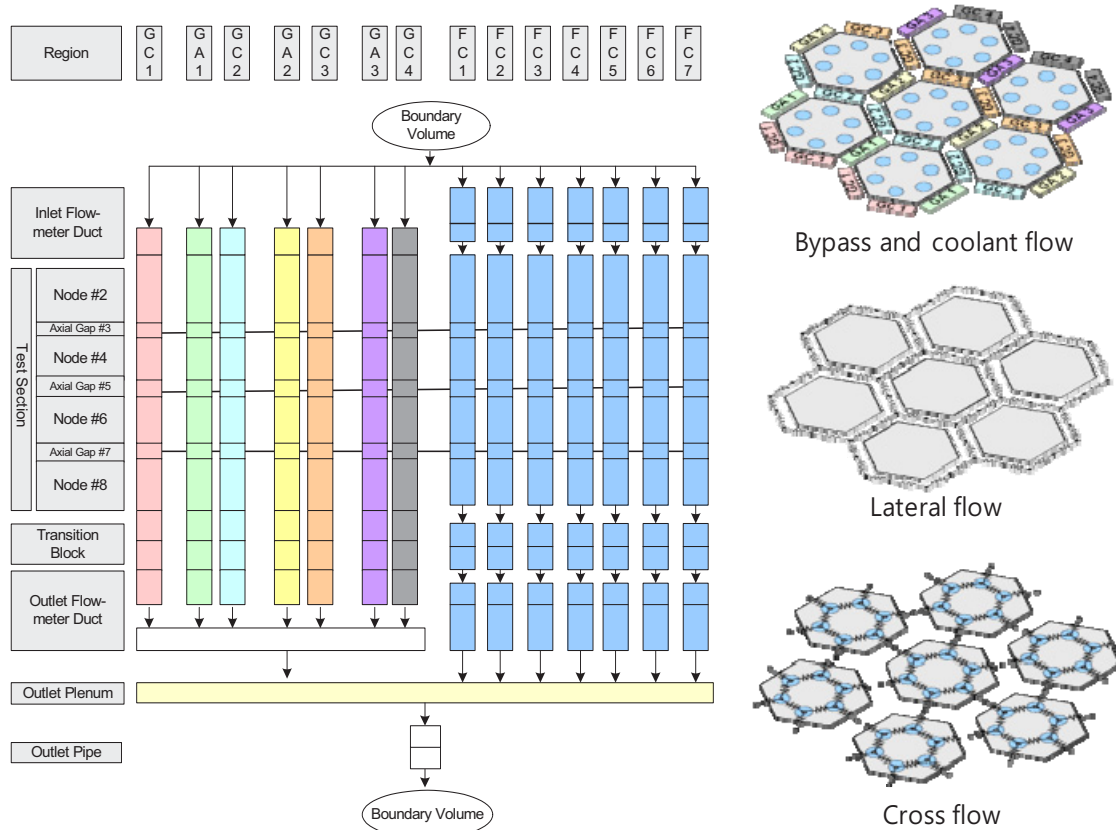
Figure 5-7. The GAMMA+ model for the SNU multiblock air test.

(a) Coolant channel   (b) Bypass gap
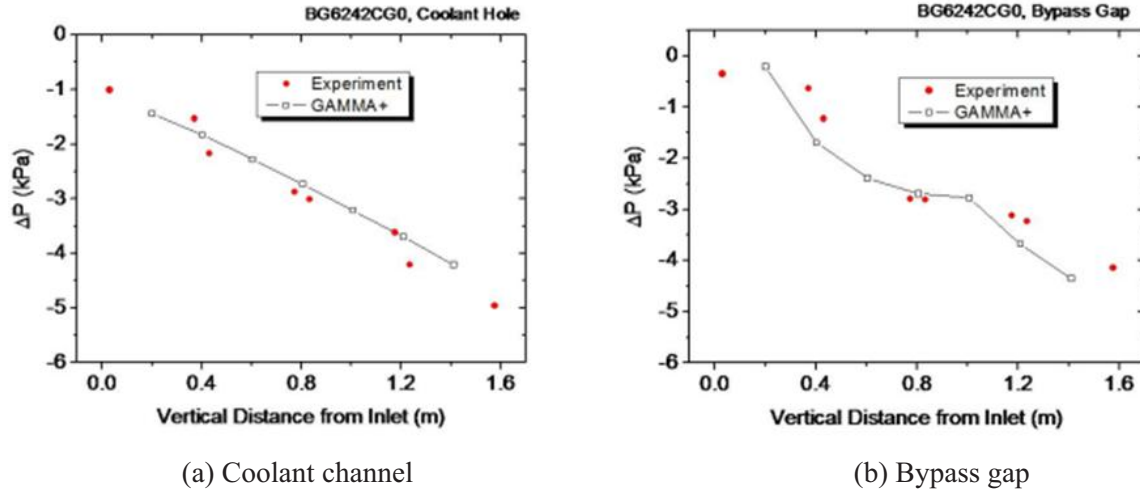
Figure 5-8. Predicted and measured pressure distributions for R2BG6242-CG2 case.

5.4   Bypass Flow and Hot Spot Analysis (KAERI)

KAERI performed the bypass flow and hot spot analysis to investigate the impacts of the variation of bypass gaps during core life cycle as well as core restraint mechanism on the amount of bypass flow and thus maximum fuel temperature. The core thermofluid analysis was performed using the GAMMA+ code for the PMR200 block-core design.

The PMR200 block-core design[13] has the thermal power of 200 MW, system pressure of 70 bar, and coolant inlet and exit temperatures of 490 and 950°C respectively. When considering the heat loss of 2.34 MW to the passive reactor cavity cooling system (RCCS), the helium coolant flow rate was 13.8 kg/s to achieve the exit temperature of 950°C.

The core region consists of 66 columns of fuel blocks stacked up with six fuel blocks each. There are two layers of reflectors at the top and bottom regions respectively. There are three rings of inner reflectors in the inner region of the core, two rings of outer reflectors, and one ring of permanent reflectors. The heat loss to the RCCS was applied at the outer surface of permanent side reflectors. The coolant flow paths are composed of bypass gap channels, coolant channels in fuel blocks, control rod(CR)/reserve shutdown coolant channels, and rising channels for the inlet coolant.

The thermal conductivity in the fuel and reflector blocks is one of the important properties determining the temperature distribution in the core. Although it should be varied with the fast neutron fluence, the dependency of thermal conductivity on the fast neutron fluence was not considered in the analysis. Instead, the irradiated thermal conductivity, lower than the unirradiated one, was used for a conservative calculation.

Figure 5-9 shows the one-sixth core analysis model for the hot spot analysis, consisting of the nodal schemes for the coolant and bypass flow channels, the lateral flow network defined at the middle point of graphite blocks, the cross flow networks at the interface between graphite blocks, and the fuel and solid submeshing. The number of flow channels is eight for the inlet riser, 73 for the coolant, 97 for the bypass, 62 for the bypass branch, six for the startup and operating control rod, and two for the reserve shutdown control rod. Total number of nodes in the fluid domain is 4,451.
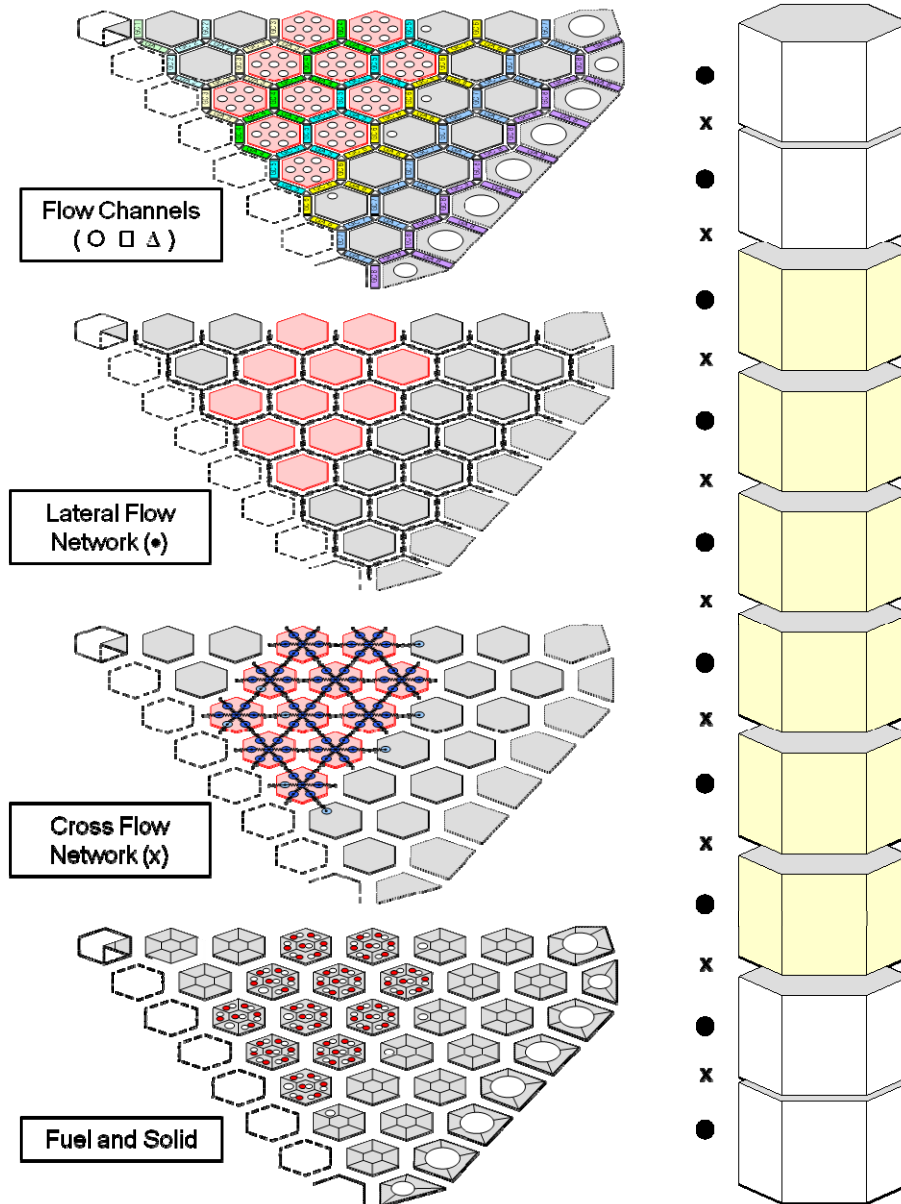
Figure 5-9. GAMMA+ PMR200 one-sixth-core analysis model.

There are 36 graphite blocks in the solid domain, which are divided into from two to seven cross-sectional meshes depending on their locations. The standard fuel block has seven solid submeshes with seven fuel compact meshes, while the control fuel block has seven submeshes with six fuel compact meshes. Uniform power distribution within the fuel block is assumed. Total number of solid meshes is 9,628.

Figure 5-10 shows the detailed multichannel flow model in the one-sixth core model, the improved features being as follows:

- Flow channels are inserted between the permanent side reflectors and the core barrel.

- Small flow nodes are eliminated at the Y-shaped joint

- Multichannel model is applied. Now the flow channels have the direction (arrows) in order to represent the 2-D flow field. The number in the box indicates the flow channels and the italic number indicates the flow path.

- Form loss calculation turns on at the converging and diverging wye.

- Re-evaluated gap size distribution is applied.
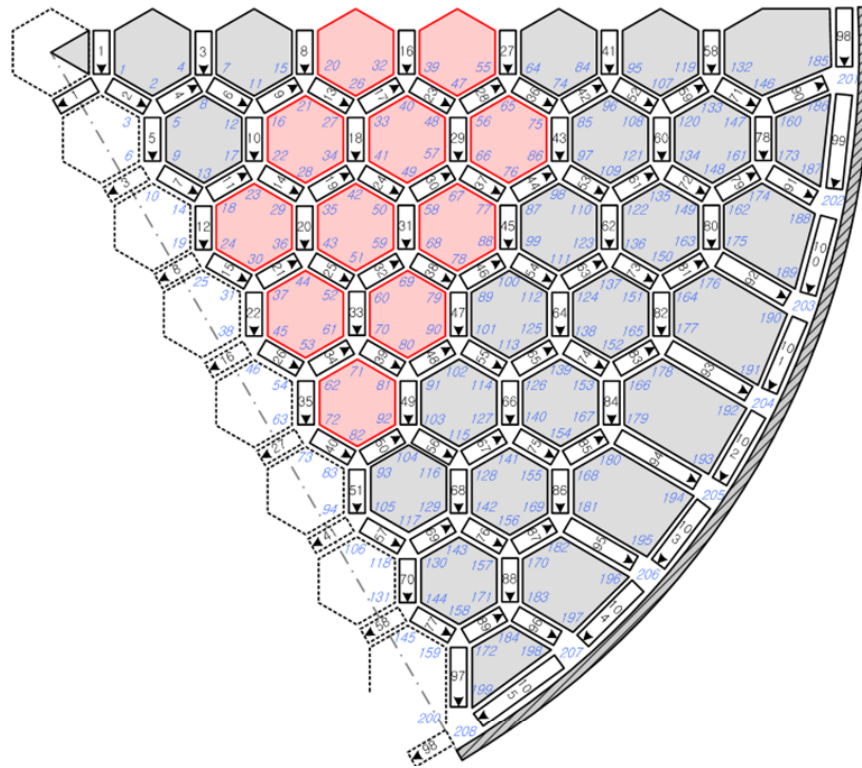
Figure 5-10. 2-D flow distribution test of the multichannel flow model.

Figure 5-11 shows the axial and radial power distribution in the PMR200 core with axial shuffling scheme. Because of fresh fuel blocks loading, the axial power profile has camel's humps and at those locations the bypass gap sizes are relatively small because of only thermal expansion of fresh fuel block without the irradiation shrinkage.

The nonuniform bypass gap distribution was obtained from the methodology developed in Task 2. It should be noted that the bypass gap size without core restraint mechanism (CRM) is determined by (1) the initial gap by block-installing tolerance, (2) the thermal expansion of core support plate, and (3) the net effect of graphite expansion and irradiation induced shrinkage/swelling. The gap in the CRM case changes with the disappearance of first and second effects, so there are no gap openings at the central and side reflector regions as well as the top and bottom ends of the active core.
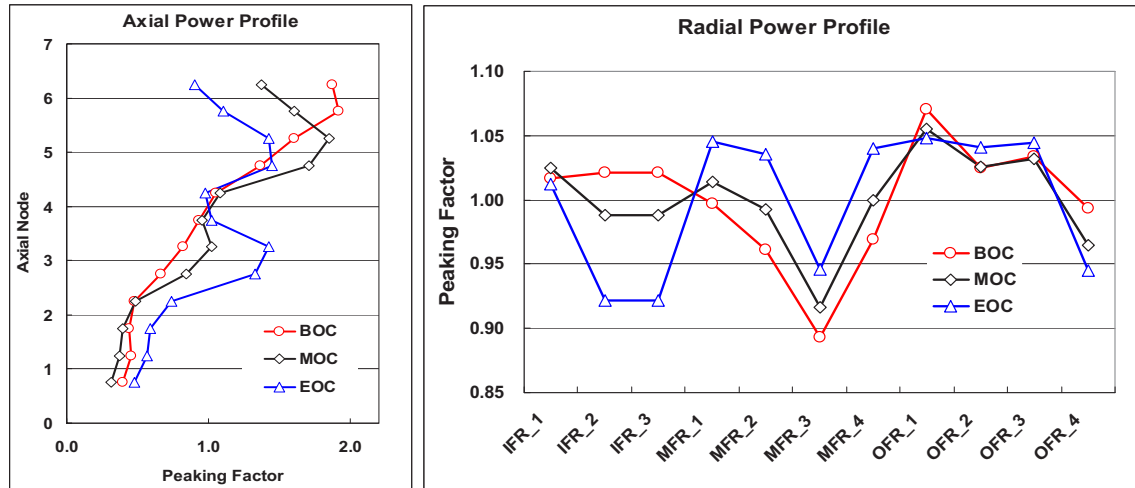
Figure 5-11. Axial and radial power profile for hot spot analysis of PMR200.

The calculation results for core bypass flow and hot spot analysis are summarized at Table 5-5. For the case of EC1 without CRM, the bypass flow reaches 31% of the total flow rate among which 26% enters into bypass gaps while 5% into the control rod channels. As the number of core cycle increases, bypass flow fraction amounts to 35% because of the bypass gap increase by the irradiation shrinkage of graphite blocks and the maximum fuel temperature reaches 1342°C. When CRM is introduced and thus bypass gaps are maintained in small, the bypass flow and the maximum fuel temperature can be reduced by about 15% and 130°C, respectively. The uniform gap results in similar bypass flow fraction of 12% but overestimates the maximum fuel temperature by 40°C. Therefore, it is advisable to select nonuniform gap distributions in the core hot spot analysis.

Table 5-5. Analysis cases and calculated major parameters.

Core Life Cycle	Cross Gap Size (mm)	Core-average Total Bypass Gap (mm)	Max. Kernel Temp. in Core (°C)	Bypass Flow Fraction (%)	
				Gap	Total
EC1(Cy07) without CRM	2.0	52	1333	26	31
EC1(Cy07) with CRM	2.0	17	1214	6	12
	1.0	17	1197	4.8	8.4
	0.5	17	1190	3.0	4.8
EC8(Cy14) without CRM	2.0	63	1342	30	35
EC8(Cy14) with CRM	2.0	27	1214	10	15
Uniform 2 mm Gap	2.0	63	1252	6	12

The influence of axial shuffling scheme and cross-flow gap size on the bypass flow is shown in Figure 5-12. Axial node number of 5 and 7 corresponds to fresh fuel block that the bypass gaps are relatively small, compared to the others. Thus, the bypass flow in those gaps is also small. Bypass flow in the CR/RSC channels increases as it flows from the top to the middle because of the cross flow. However, the bypass flow decreases as it approaches the bottom, which is blocked. These characteristics of bypass flow distribution disappears as the cross flow is diminished by the decrease of cross-flow gap size.
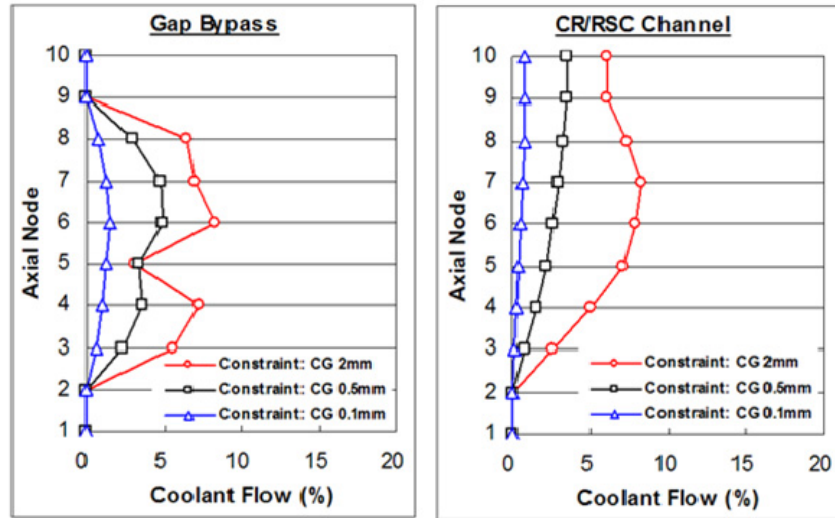
Figure 5-12. Bypass flow distribution in PMR200 core hot spot analysis.

The maximum kernel temperature profile shown at Figure 5-13 is proportional to the power-to-flow ratio. That means the temperature profile is strongly affected by bypass flow distribution at a given power distribution. Therefore the uniform bypass gap case is different from other cases. Generally the fuel blocks with CR/RSC holes show relatively high kernel temperatures because the coolant flow passing through the centre region is reduced by the bypass flow through CR/RSC hole.
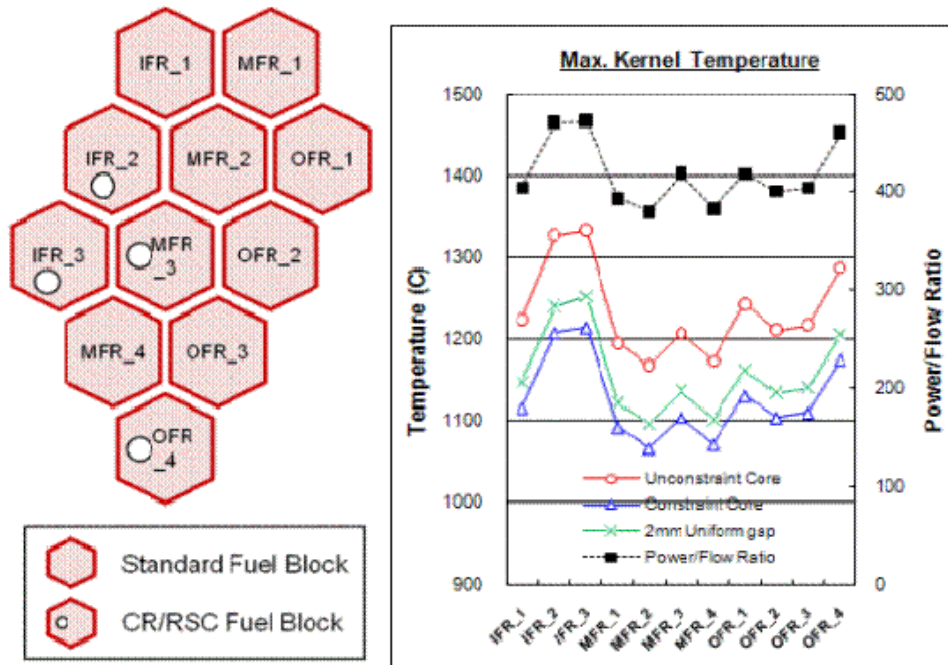
Figure 5-13. Maximum kernel temperature profiles.

5.5 CFD Benchmark Calculations for MIR Test (INL/KAERI)

5.5.1 CFD Analysis by INL

A scaled model has been developed for installation in the INL's MIR test facility. The scale is a factor of 2.016 greater than the actual geometry. The model is based on the MHTGR[14] prismatic reactor. Figure 5-14 gives a sketch of three adjacent prismatic blocks from a GA MHTGR. Because the focus of the standard problem is the gap flow, the model was chosen to center on the gap region between three blocks. The scaled model geometry is bounded by the thick red line in the figure. Only three standard coolant channels are included from each block in the model. The junction of the three gaps is the center of the scaled model.
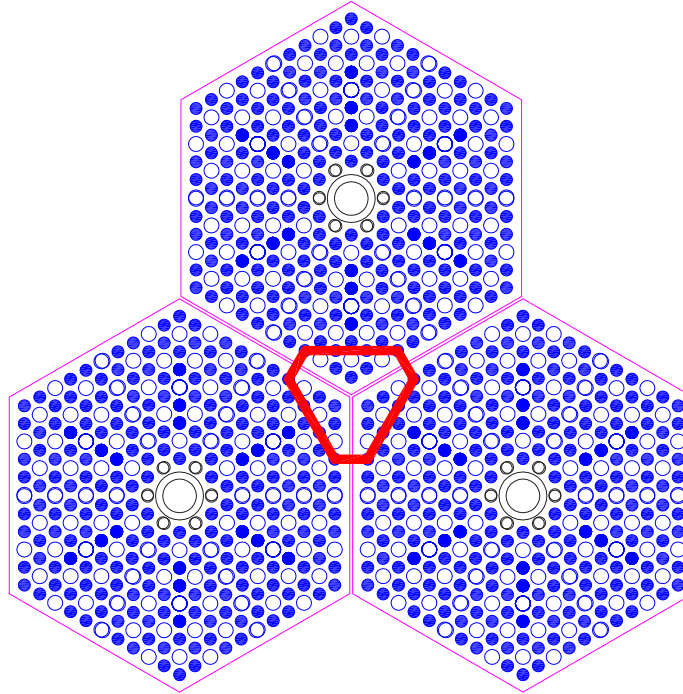
Figure 5-14. Three prismatic blocks from the MHTGR reactor and outline of test model geometry.

Figure 5-15 shows a close-up view of the source of the model geometry and a view that eliminates those things that are extraneous to the bypass model geometry. The lines parallel to the gap edges represent bevels machined in the graphite in the original MHTGR prismatic blocks. Three coolant channels are present for each block. Note that the flow in the bypass scaled model will be isothermal.

Figure 5-16 illustrates the primary components of the bypass flow model. These include the inlet annulus where the working liquid (mineral oil) enters and is then directed upwards, a hemisphere that redirects the flow downwards, an upper plenum, an upper fuel block, an adjustable horizontal gap, a lower fuel block, and two orifice plates that enclose screens in the channel and gap flow paths. The screens are intended to increase the pressure drop over the shorter lower fuel block to the same value as the upper fuel block. Also shown are the flow paths of the mineral oil along with the layout of the supported model as it will sit in the working section of the MIR test facility. The bypass model is designed to have adjustable gap widths. The vertical gaps visible in Figure 5-15 are adjustable from 2, to 6, to 10 mm, representing 1, 3, and 5 mm in the actual block size. The horizontal gap can be set to widths of either 2 or 10 mm.
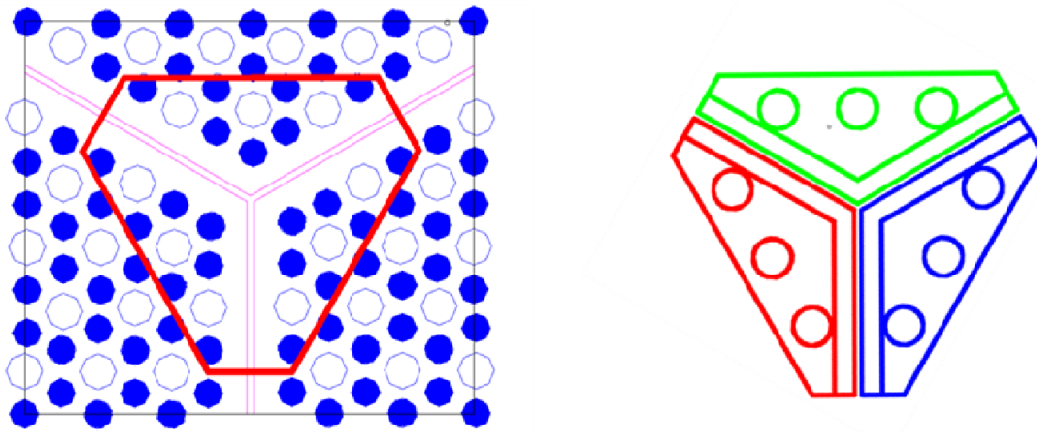
Figure 5-15. Close-up view of the origin of the bypass flow model and a cross-sectional view of the model.
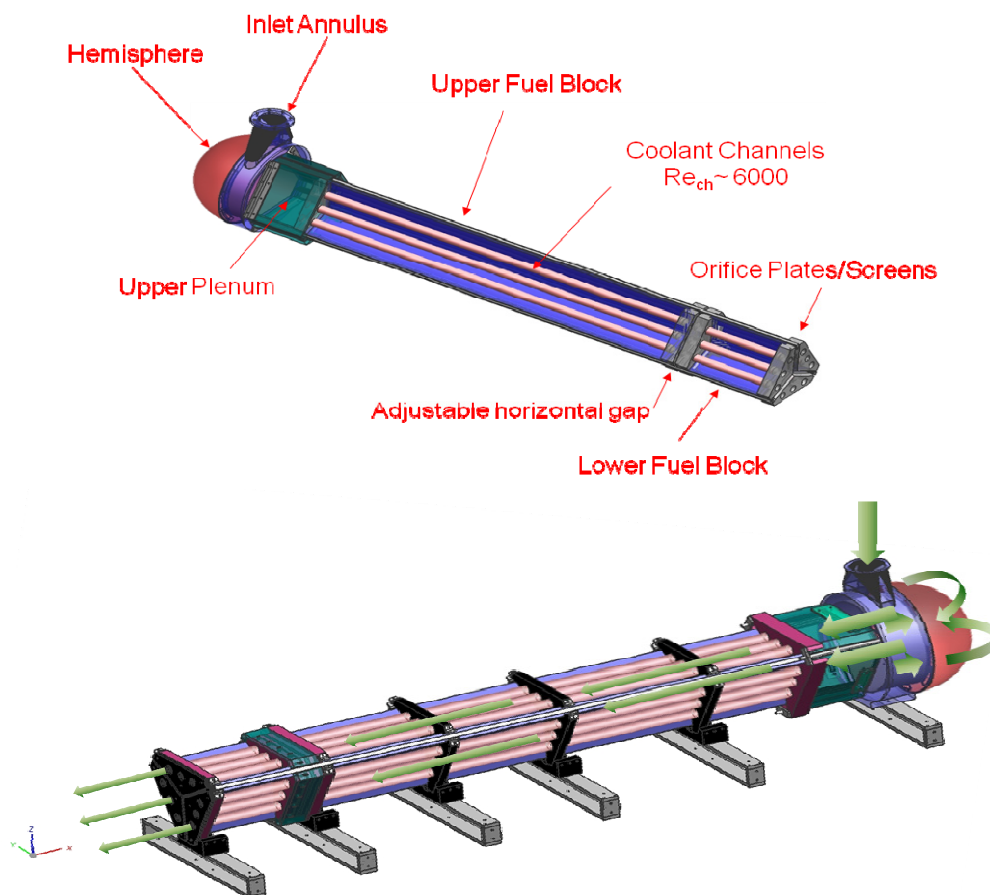
Figure 5-16. Schematics of the bypass model showing components and flow paths.

The CFD models used in the present study consist of a one-sixth section of the full geometry because of symmetry. Figure 5-17 shows a top view of the CFD grid, constructed using GAMBIT 2.4.6, which is bundled with CFD code FLUENT.[15] Also shown is the coordinate system; the axial coordinate Z is negative in the flow direction with zero datum at the inlet. Note that symmetry allows that only one-half of the gap is included in the CFD model.
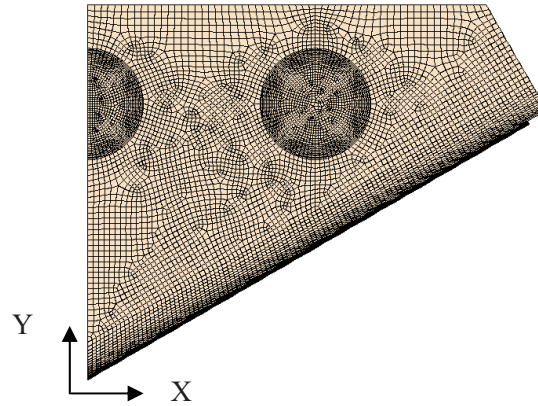
Figure 5-17. Plan view of the CFD model showing the mesh.

Figure 5-18 shows two views of the CFD model, including an isometric view of the whole model and a close-up view of the inlet and upper plenum. Because the MHTGR graphite blocks are beveled around their faces, the model includes this bevel. The close-up view of the upper plenum shows the beveled entrance into the gap region; the thin gap region extends downward from the bevel. The bottom of the upper fuel block and the top of the lower fuel block are also beveled.
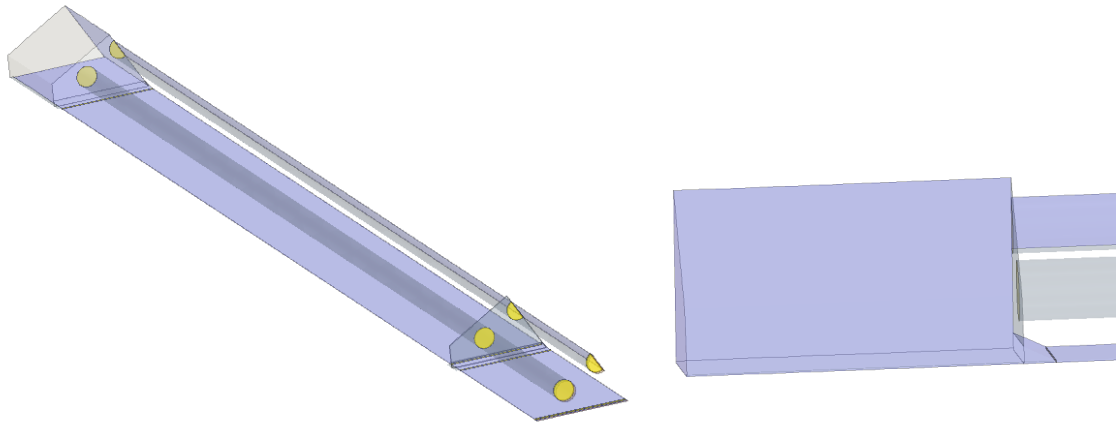
Figure 5-18. Overview of CFD model and close-up of upper plenum of model.

The upper plenum of the bypass apparatus is 178 mm long; the channels have 32 mm diameters; the first block is 1,599 mm long; the second block is 326 mm long; the channels are located 28.4 mm from the top wall and are 65.6 mm apart; the span from the origin to the top of the block is 107 mm; the distance from X = 0 to the first corner at the top of the block is 115 mm; the width of the angled edge to the right of said corner is 35 mm; the bevel is 17 mm deep and 8.3 mm wide.

The inlet condition for the CFD models is set to a constant mass inflow for the one-sixth section. The mass inflow that can be pumped through the apparatus by the MIR facility pump is estimated to be 2.84 kg/sec for the one-sixth sector. However, it was found that this flow rate resulted in laminar flow for all of the configurations, so a mass flow of 8.0 kg/sec was also specified for two of the cases for comparison purposes. A flow rate of 1.34 kg/sec was also used to represent the first MIR test data set; the lower flow is to ensure that the structure of the quartz model remains intact. The three outlet conditions (for the full and half channels and the gap) are set to pressure outlet at 0 Pa. The density and dynamic viscosity of the mineral oil are set to constant values of 831.1 kg/m^3 and 0.011685 Pa-sec.

The commercial code STARCCM+[16] is used for the computations. The flow in the upper plenum and the horizontal gap are assumed to be turbulent flow. The standard k-ε two-layer turbulence model using the all y+ wall treatment is used. This turbulence model and wall treatment have been shown in companion studies to yield wall shear stress that is within 5% of several published friction factor coefficients for y+ values in the 2 to 11 range. The y+ values for the nominal grids used herein are between 2 and 3. The turbulent inlet conditions are specified as turbulent kinetic energy = 0.01 J/kg and dissipation rate = 0.1 J/kg-sec.

STARCCM+ allows the suppression of turbulence in regions where the flow is expected to be laminar. When the gap flow for the present calculations is found to be laminar, the turbulence is suppressed in the region of the vertical gaps, not including the wider region where the bevels are located (at both ends of the first block and the front end of the lower block). Finally, as described above, it is intended that screens be positioned near the outlets of the gap and channels to increase the pressure drop such that the drop across the second block is about the same as across the first block. Inasmuch as no screen has yet been specified to do this, the screen sections are left as open flow regions in the present CFD models.

The segregated solver is used in STARCCM+ along with second-order differencing for the convection and diffusion terms. The solutions are iterated to residuals below 1.0×10^{-4} for STARCCM+, which has been found to be sufficient for iterative convergence in previous studies[17,18] or until they do not converge further, as noted below. All walls are no-slip walls. No artificial diffusion is added.

The grids used in the present study contain a nominal 4.19 million cells. To determine if the mesh is sufficiently fine, a finer mesh was constructed by increasing the node count by 1.25 along the edges of the faces used to create the grid. The refined mesh contains 8.73 million cells. Results are obtained for the case of 2 mm vertical and 2 mm horizontal gaps for both the nominal and refined grid. Figure 4-18 plots axial pressure profiles through the center of the full channel and the center of the gap for the two cases. As can be seen, the profiles for the two cases are very close. In fact, the maximum variations in pressures for the channel and the gap are slightly less than 1%, leading to the conclusion that the nominal grid is sufficiently fine.
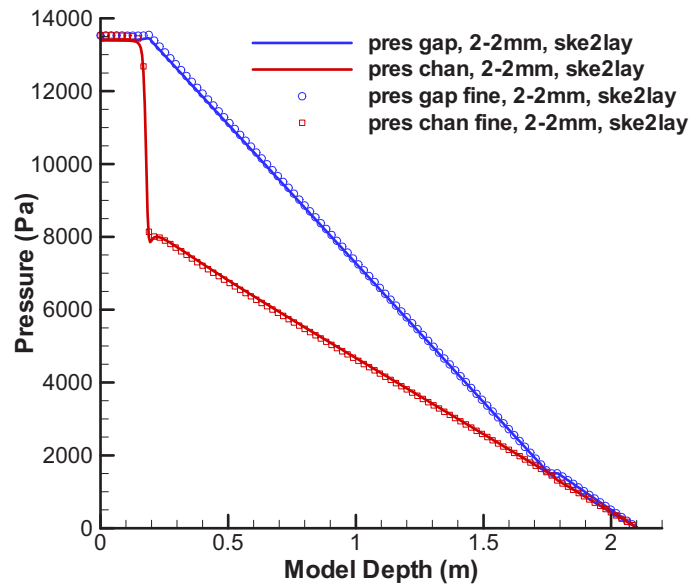
Figure 5-19. Axial pressure profiles in the full channels and gaps.

5.5.2   Results and Discussion

CFD calculations are made for seven different cases for the bypass flow. These include the 2 mm vertical gap with 2 and 10 mm horizontal gaps and the 6 mm vertical gap for the same two horizontal gaps for inlet mass flow 2.84 kg/sec. Also, an extra-low-flow case was performed as a pretest calculation for the first dataset that will be taken at a lower flow rate. This case is for the 6 mm vertical/2 mm horizontal gap cases with a flow rate of 1.34 kg/sec. Two additional simulations are made for the 6 and 10 mm vertical gap, both with 2 mm horizontal gap, for an inlet mass flow of 8.0 kg/sec. It was found that this flow rate yields transitional flow in the 6 mm vertical gap and turbulent flow in the 10 mm vertical gap configurations. The residuals for all cases are below 2×10^{-4}, except for the 6-2 mm/low flow (LF) case (6 mm vertical/2 mm horizontal gaps/low flow) whose residuals flattened out below 5×10^{-4}.

Table 5-6 summarizes the seven cases. Quantities shown above the double horizontal line are inputs; those below are outputs. The Reynolds numbers of the coolant tubes, based on tube diameter, and those of the gap, based on full gap width, are given. It shows that flow in the coolant tubes is turbulent for all cases except the 6-2 mm/extra low flow (XLF), which is transitional; this case is shown in gray. However, the same turbulent flow model is used for the 6-2 mm/XLF case in the coolant channels as for the other cases. For the gap flows, reference is made to Patel and Head,[19] who measured skin friction in pipes and channels (between parallel plates, not to be confused with the present tubular coolant channels). For a Reynolds number based on channel width 'h', they indicate that laminar flow occurs for Reh < 1300, and fully turbulent flow for Reh > 2800; flow in between is transitional. It is seen that the gap flow for the lower mass flow rate cases is laminar. The gap flow for the 6-2 mm/high flow (HF) case is transitional. The flow for the 10/2 mm/HF case is in the turbulent zone. For these last two cases, the standard k~ε turbulence model is used for entire flow field. While a transitional flow model is available in STARCCM+, it requires knowledge of turbulence levels at the inlet; these are not yet available. Hence, the flow computed in the gap for the 6-2 mm/HF case is somewhat suspect. Also, the flow computed in the coolant channels for the 6-2 mm/XLF case is suspect as the flow is also transitional.

Table 5-6. Summary of flow results for the seven cases.

Vertical gap (mm)	2		6				10
Horizon. gap (mm)	2	10	2	10	2	2	2
Total mass flow(kg/s)	2.84 LF	2.84 LF	2.84 LF	2.84 LF	8.0 HF	1.34 XLF	8.0 HF
Re$_{chn}$ (1st sec) flow regime	6387 turbulent	6387 turbulent	5440 turbulent	5400 turbulent	15024 turbulent	2710 transitional	12362 turbulent
Re$_{gap}$ (1st sec) flow regime	31 laminar	32 laminar	524 laminar	543 laminar	1668 transitional	175 laminar	3192 turbulent
Total press. drop (Pa)	13560	13720	10420	10600	64798	3086	45334
Gap fraction 1st sec. (%)	0.97	0.97	15.6	16.2	17.3	10.8	31.9
Gap fraction 2nd sec. (%)	0.61	0.65	13.4	12.4	14.9	9.5	29.9

The overall pressure drop is seen to be higher for the 2-mm vertical gap cases than for the 6-mm vertical gap cases for the lower mass flow rates. This is because the former present a smaller flow area,

but with the same resistance to flow (that is, the same wall area) relative to the latter. For the lower mass flow, the flow in the 6-mm gaps is about 15-times that of the 2-mm gaps, though the flow area is only 3-times greater. This is a result of the increased flow area with no increase in flow resistance. This underscores the point that both flow resistance as well as the flow area that control the relative flows in the coolant channels and bypass gaps.

It is seen that the flow fraction in the gaps in the second section is somewhat less than that in the first sections in all cases, though the difference is less as the vertical gap width increases. This is probably because of the fact that the momentum of the flow in the upper plenum coming into the first section gap is higher than is the momentum in the vicinity of the gap in between the two sections. However, this effect is diminished as the vertical gap width increases and the momentum in the gap also increases. Finally, note that the percent of mass flow fractions in the gaps for the 6-2 mm/HF case are close to those for the 6-2 mm/LF case, even though one is turbulent and the other is laminar. This is the case because, even though there is a variation in wall friction between laminar and turbulent flow, the difference between flow resistances in the coolant tubes versus the gap is far greater.

Figure 5-20 shows a contour plot for the streamwise velocity at a point 55 mm from the inlet for the 2-2 mm/LF case, the 6-2 mm/XLF case and for the 6-2 mm/LF case. Note that the contour plots and profiles shown herein are smoothed by the CFD code. The maximum velocity magnitude is seen to be along a region parallel to the outer wall from where it drops to zero at the wall and drops slightly toward the three-gap junction for the 2-2 mm/LF case. The contours for the two 6-2 mm cases are similar to the 2-2 mm/LF case except that the ridge of high velocity magnitude is concentrated near the upper right corner. Results for the other cases are similar. The velocity scale is different for each case.
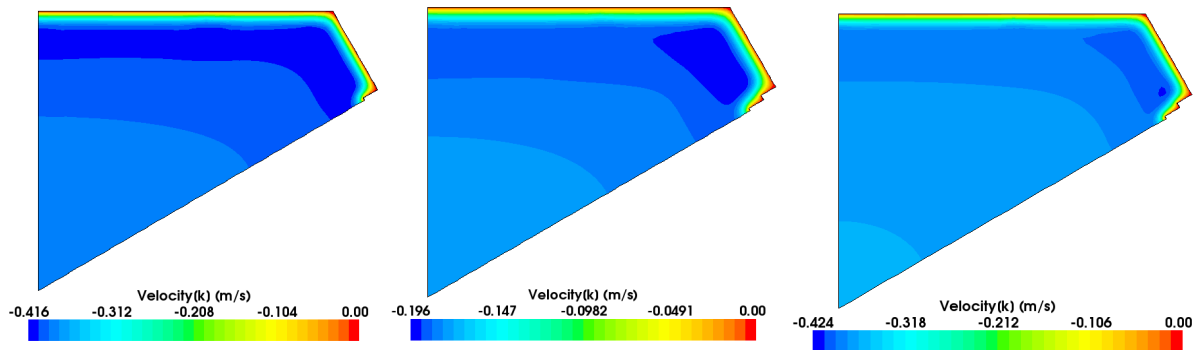
Figure 5-20. Axial velocity contours at 55 mm for 2-2 mm/LF, 6-2 mm/XLF and the 6-2 mm/LF cases.

Figure 5-21 shows a side view of the velocity magnitude in the upper plenum and initial parts of the coolant channel and gap for the 2-2 mm/LF case, 6-2 mm/XLF case, 6-2 mm/HF case, and 10-2 mm/HF case, respectively. The view plane cuts through the center of the full channel. As can be seen, the velocity changes little except near the wall at the top for at least half the length of the upper plenum. The increase in the gap width is obvious in the four graphics. The ranges of the velocity magnitude are between the minima and maxima for each case. Even though the first two cases are for lower flow and the second two cases are for high flow, it is obvious that the velocity in the gap increases relative to the maximum velocity as the gap width increases. Also note that the flow in the channel for the wider 10-2 mm/HF case is lower than for the 6-2 mm/HF case because the gap flow is higher.

Figure 5-22 provide contours of the turbulent to (molecular) viscosity ratio for 6-2 mm/LF and 10-2 mm/HF cases in the upper plenum and block entrance. While the turbulent quantities are constant at the inlet, there is large variation of the turbulent viscosity in the upper plenum. It remains to be seen what the actual levels will be in the data. Turbulence can be detected in the gap for the 10-2 mm/HF case.
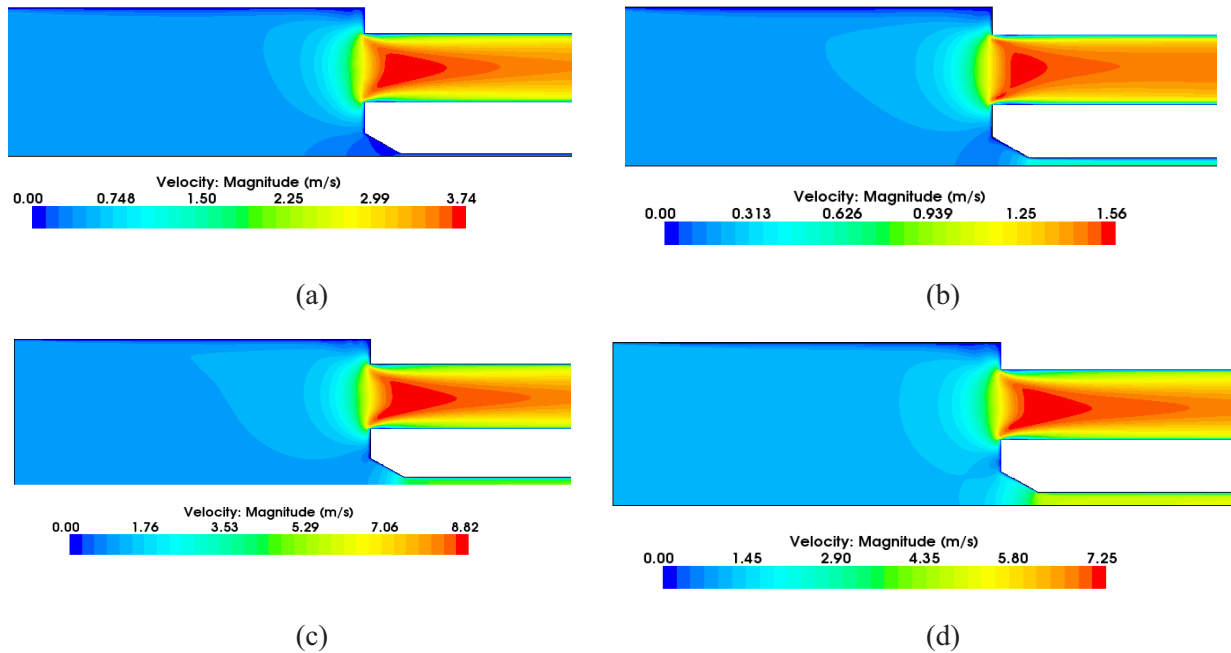
Figure 5-21. Velocity magnitude for (a) 2-2 mm/LF, (b) 6-2 mm/XLF, (c) 6-2 mm/HF, and (d) 10-2 mm/HF cases.
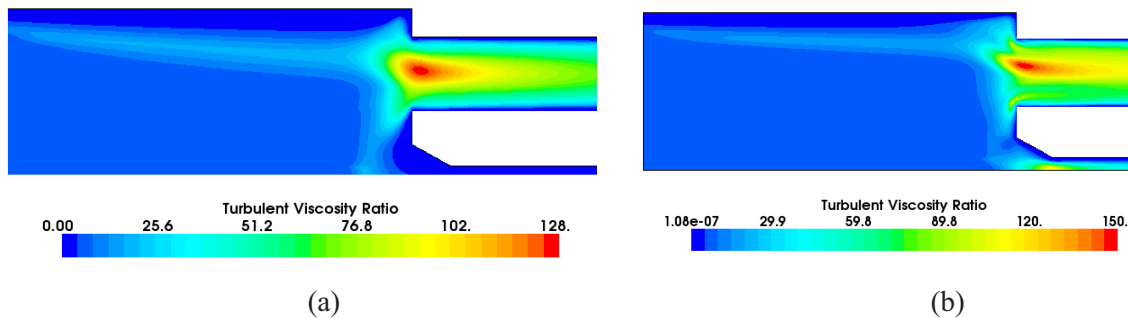
Figure 5-22. Turbulent to molecular viscosity ratio for 6-2 mm/LF and the 10-2 mm/HF cases.

An important aspect of the flow is the associated pressure drop. Figure 5-23a plots axial profiles of the pressure for the four low flow cases along the center of the gap, that is, centered between the right and left ends. The pressure drop for the two 2-mm vertical gap cases is much higher than for the 6-mm cases. This is expected because the narrower gaps present greater resistance. The width of the horizontal gap appears to make little difference on the overall pressure drop. There is, however, a slight bump in pressure at the horizontal gap, which starts at $Z = 1.776$ m for the 6-2 and 6-10 mm cases.

Figure 5-23b plots the axial pressure profiles for the four low flow cases along the centerline of the full channel. The pressure drop decreases in the channels as the vertical gap width increases; this is because there is a lower flow rate in the channels for the 6mm vertical gap cases. Figure 5-24 gives axial pressure profiles for the extra low flow case and for the two high flow cases for gaps and channels. The pressure needed to drive the HF cases is much higher than for the lower flow rates. The difference in pressure for 10-2 mm/HF is less than for 6-2 mm/HF because flow resistances are closer between gap and channel.
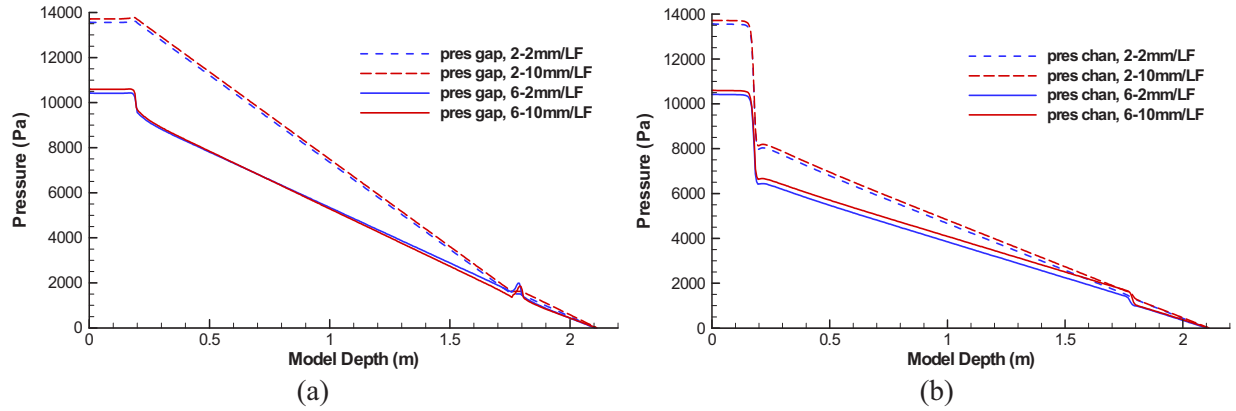
Figure 5-23. Axial pressure in (a) the gaps and (b) the full channel for low flow cases.
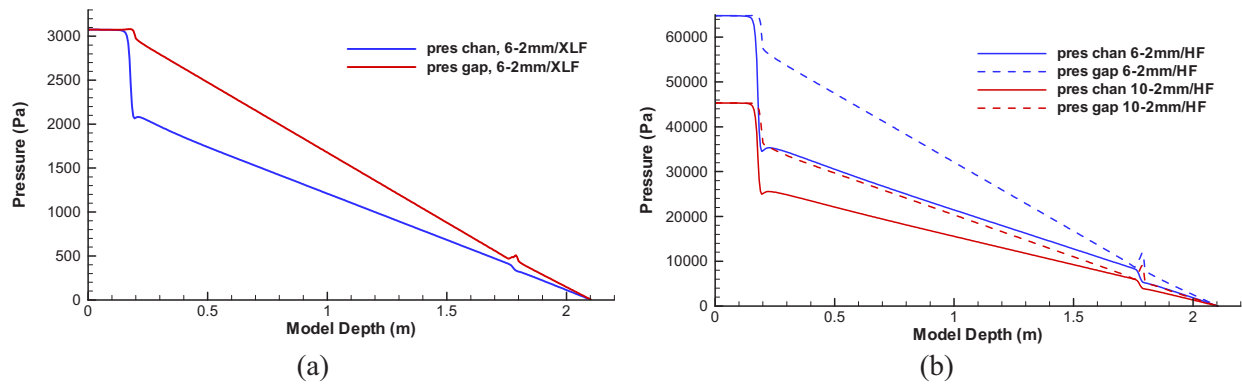
Figure 5-24. Axial pressure profiles for (a) the extra low flow case and (b) the high flow cases.

Figure 5-25 plots radial velocity profiles at four axial locations in the full channel in the first block at 0D, 25D, 45D, and 48D (diameters) from the channel entrance for the 2-2 and 6-2 mm/LF cases. Note that the channel is 49.95D long in the first block. As shown, the turbulent flow appears to be fully developed by 25D, as it doesn't change beyond this location. The profiles for the 6-2 mm/LF case are similar to the 2-2 mm/LF case, but with a lower bulk velocity. Figure 5-26 plots the radial profiles of the mean axial velocity for the XLF case and for the two HF cases. The velocity is much lower for the XLF case and much higher for the HF cases than for the LF cases of Figure 5-21. The velocity is higher for the 6-2 mm/HF case than for the 10-2 mm/HF because more flow goes into the bypass gap for the latter case.

Velocity profiles are provided in Figure 5-27 for the flow in the gaps for the LF cases. The profiles are taken at the same depth as for the 45D channel location, which is over 700 gap widths for the 2 mm vertical gap cases. Turbulence has been suppressed for the gap flows in the LF cases, making it laminar. The computed profiles are each compared to the theoretical profiles computed from the analytical solution for fully developed laminar flow in a channel. The analytical profiles are based on the maximum flow velocity, which comes from the CFD calculations. The flow profiles conform very closely to the analytical laminar solutions. Note that the gap coordinate is a local coordinate normal to the gap wall; h/2 is the gap half-width. Figure 5-28 shows the gap profiles at the same axial location for the one XLF case and the two HF cases. The XLF case is modeled as laminar flow while the HF cases are both modeled as turbulent flow. The gap coordinate is used for Figure 5-28. The parabolic nature of fully-developed laminar flow is seen to characterize the shape of the velocity profile of the XLF case. Note that the gap computed is only one-half of the actual gap because of symmetry considerations as discussed earlier.
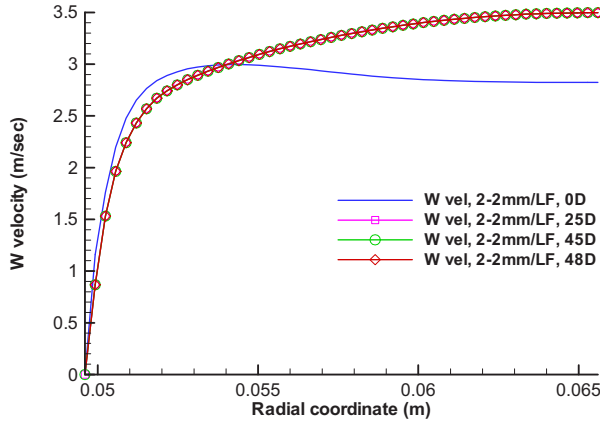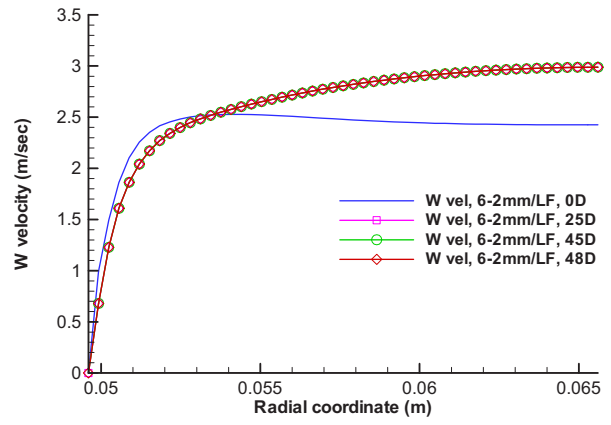
(a)   (b)

Figure 5-25. Radial velocity profiles in the channel for 2-2 and 6-2 mm/LF cases.
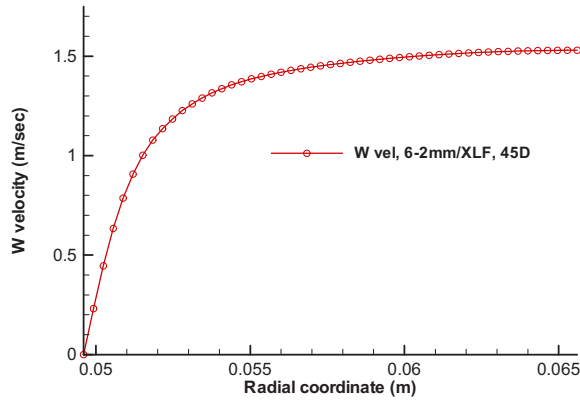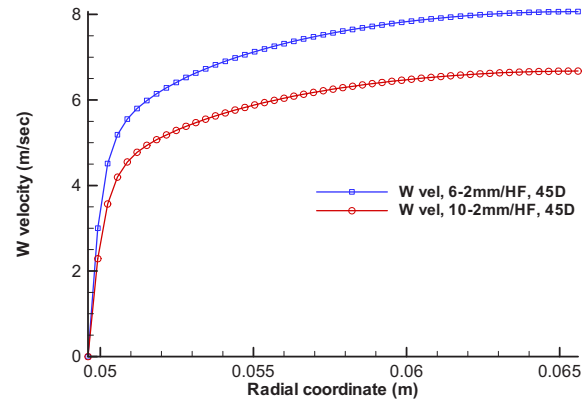
(a)   (b)

Figure 5-26. Radial velocity in the channel for (a) the 6-2 mm/XLF case and (b) the two HF cases.
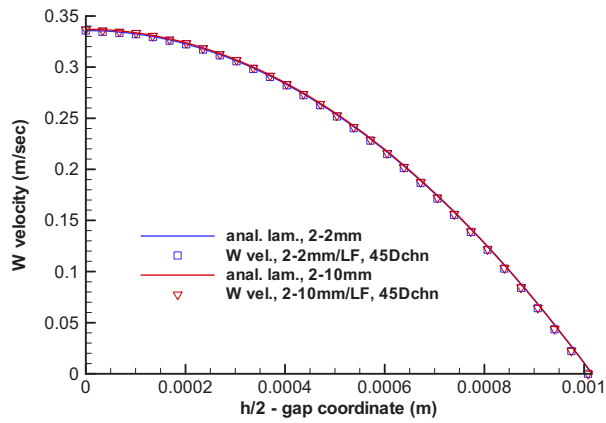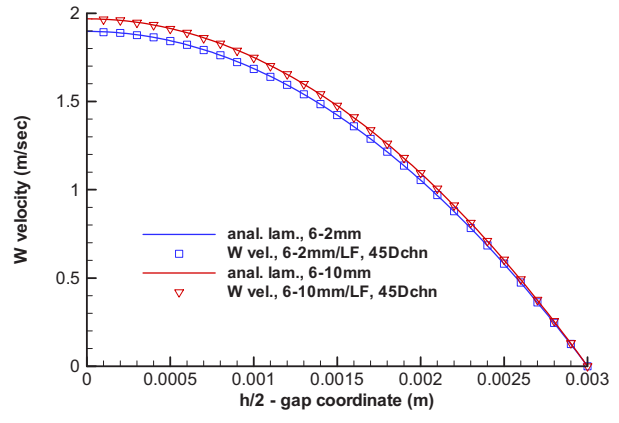
(a)   (b)

Figure 5-27. Radial velocity profiles for the 2 and 6 mm vertical gap cases vs. the analytical solutions.
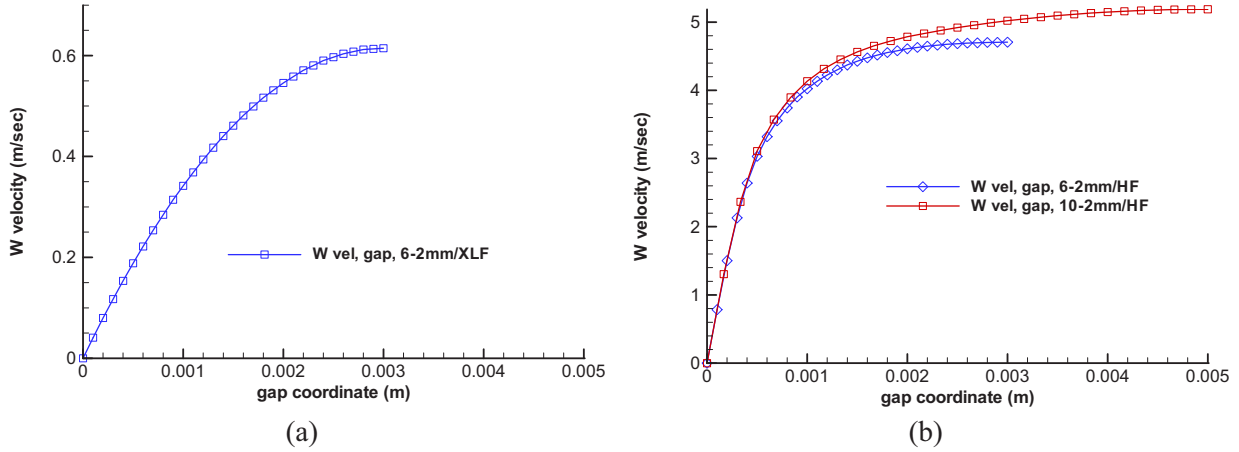
Figure 5-28. Lateral velocity profiles for (a) XLF cases and (b) two HF cases in the gap.

An interesting feature of the bypass flow is the junction of the three vertical gaps at the center of the apparatus as shown in Figure 5-13. The junction is a region of low flow resistance. Figure 5-29 show contour plots of the gap junction for 2, 6, and 10 mm vertical gaps in the first block. The velocity is a maximum at the junction centers, but the region of higher velocity is small, making this effect insignificant.
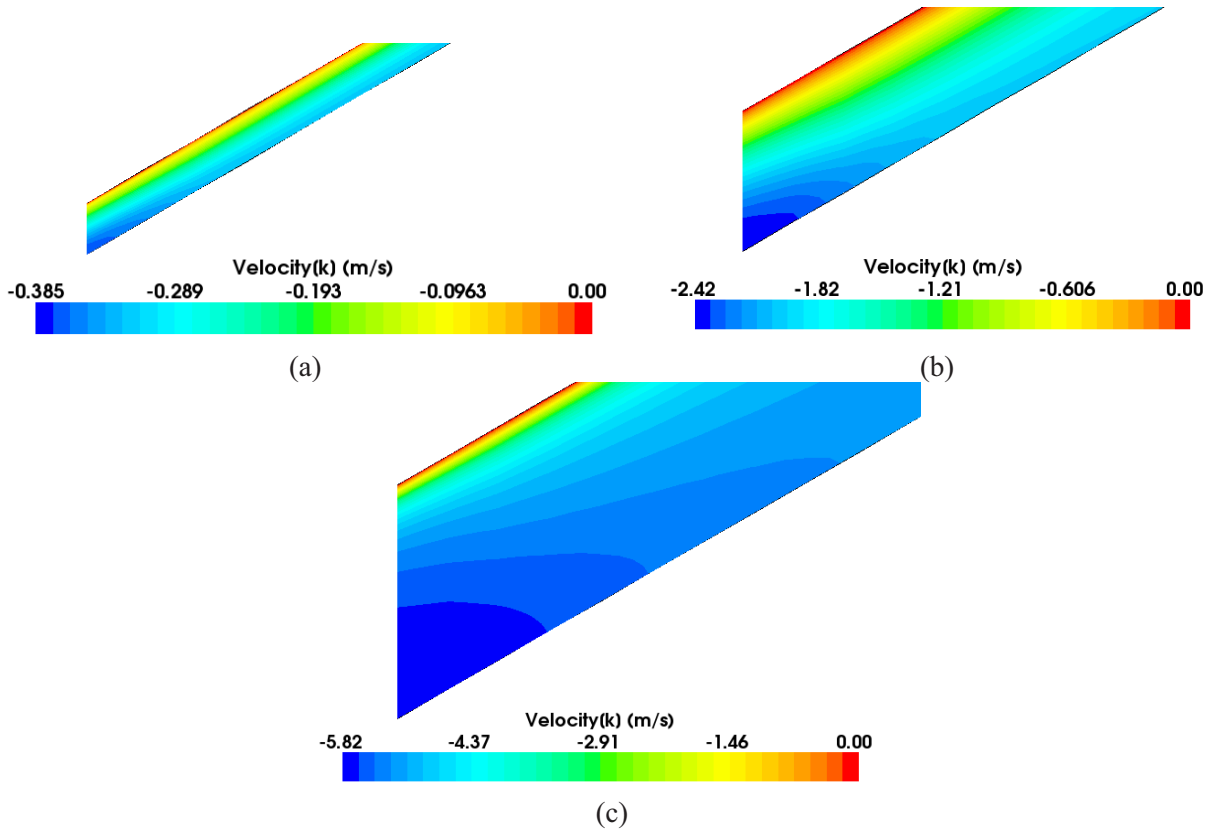
Figure 5-29. Axial velocity at the gap junction for the (a) 2-10 mm/LF, (b) 6-10 mm/LF, and (c) 10-2 mm/HF cases.

68

Figure 5-30 plots the vertical velocity for cases 2-10 mm/LF, 6-10 mm/LF, and 10-2 mm/HF from the center of the junctions along the plane of symmetry at axial location 45D. The flow velocity is significantly higher in the high flow 10 mm case than the other cases as expected. The extent of the velocity increase along the plane of symmetry is greater the larger the gap. Nevertheless, the extent of the region of increased velocity is small relative to the whole lateral gap span. Note that the distance along the gap in Figure 5-26 extends from the junction center to the midpoint of the span of the gap in the CFD model; the gap span of the model is only about one-third of the total gap span. (See Figure 5-13.)

It is interesting to examine the pressure distribution in the horizontal gap between the two blocks. Figure 5-30 plots pressure contours in the horizontal gaps at planes half-way between the two blocks for four cases. Figure 5-31 shows pressure contours for three 2 mm horizontal gap cases: 2-2 mm/LF, 6-2 mm/XLF, and 10-2 mm/HF cases. An increase in pressure is seen to occur in each case from the coolant channels towards vertical gap along the diagonal edge. The lateral pressure gradient has mostly to do with the flow resistance present because of the narrowness of the horizontal gap. The one 10 mm horizontal gap case shown, Figure 5-31(d), for the 2-10 mm/LF case, shows no lateral pressure gradient except near the channels where it shows a series of peaks and valleys, which are related to a vortex ring in the gap. The vortex ring is evident in Figure 5-32, where velocity vectors are plotted and shown from a side view of the horizontal gap.
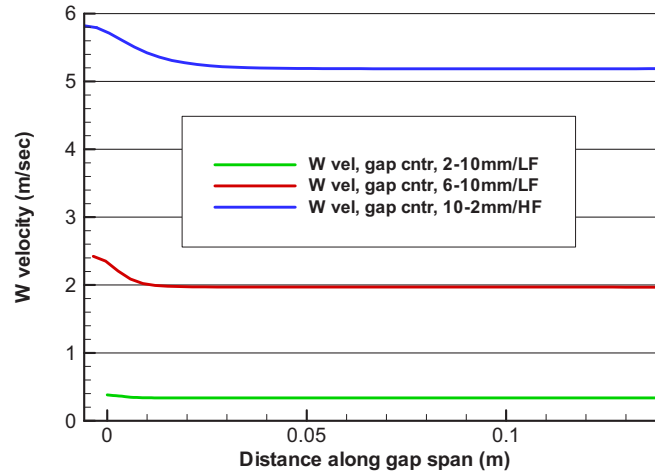
Figure 5-30. Velocity for gap span center for the 2-10 mm/LF, 6-10 mm/LF, and 10-2 mm/HF cases.

(a)   (b)

(c)

(d)
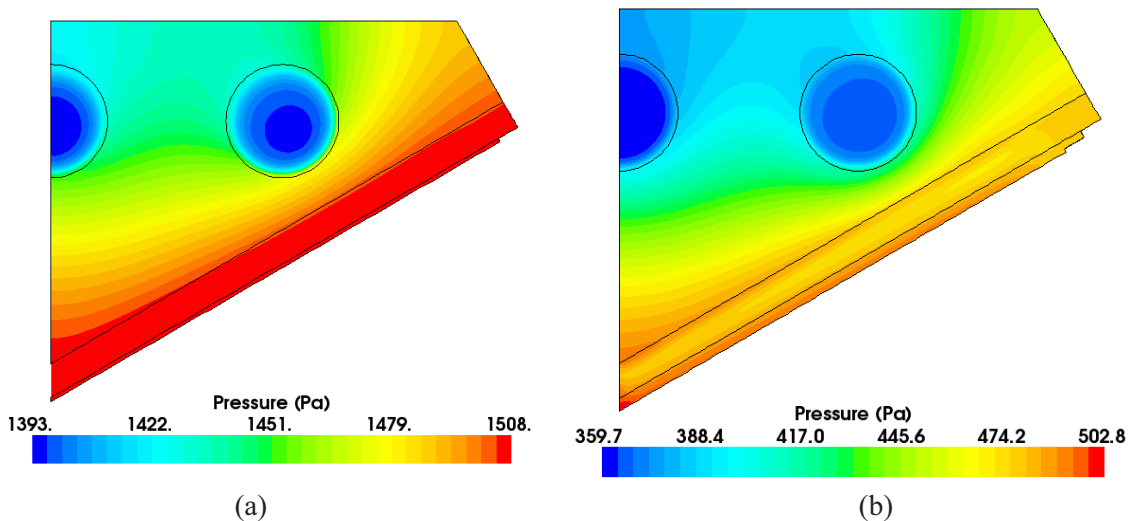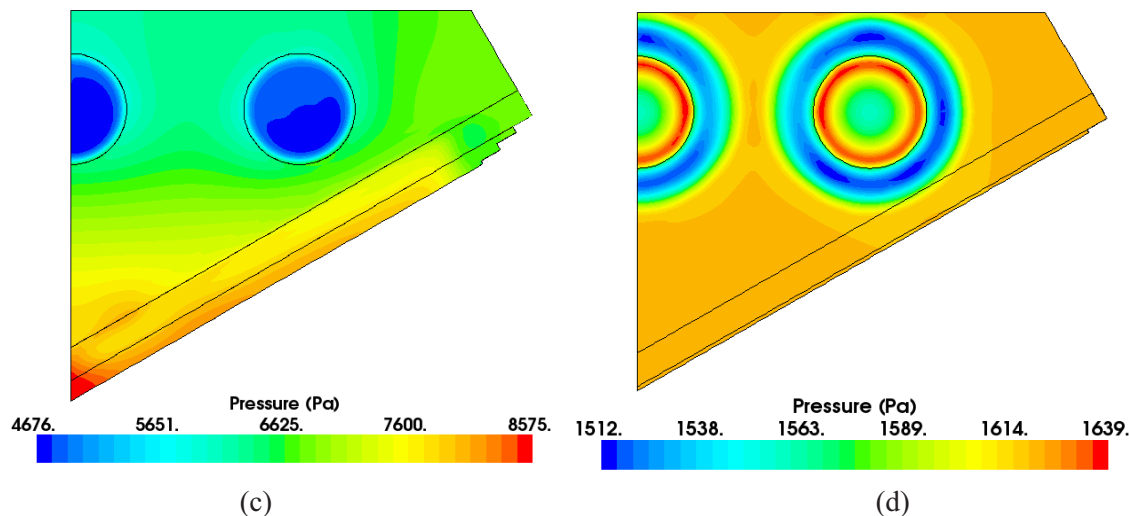
Figure 5-31. Pressure contours in the center of the horizontal gap for the (a) 2-2 mm/LF case, (b) 6-2 mm/XLF case, (c) 10-2 mm/HF case, and (d) 2-10 mm/LF case.
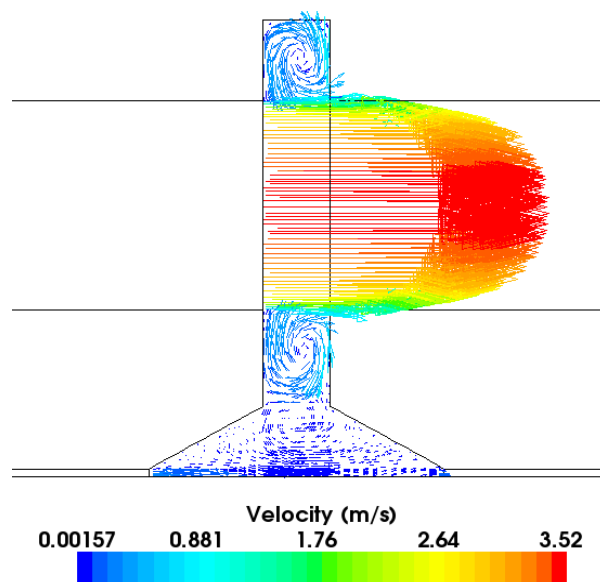
Figure 5-32. Velocity vectors in the horizontal gap for the 2-10mm/LF case showing a vortex ring.

Figure 5-33 provides contour plots of the velocity magnitude at the half-way point in the horizontal gap for the 2-2 mm/LF, 6-2 mm/XLF, 6-2 mm/LF, and 10-2 mm/HF cases. Results for the cases with wider horizontal gaps are similar to those for the narrower gaps. While the velocity magnitude for the channels is the greatest, it can be seen that the velocity in the 6- and 10-mm gaps is relatively greater than in the 2-mm gap for the LF cases. This emphasizes that the resistance to flow has a primary influence in the bypass flow, not just the size of the flow opening. In other words, the amount of wall (resistance) per unit of flow area is a significant factor in determining the flow rate of the bypass (and all) flow.

In summary, quantitative results have been provided to describe the isothermal flow in six configurations of the MIR bypass flow apparatus. Velocity and pressure profiles and contours are presented that may be compared to eventual experimental data. Of course, the inlet flow conditions may be somewhat different in the actual experiments.

70
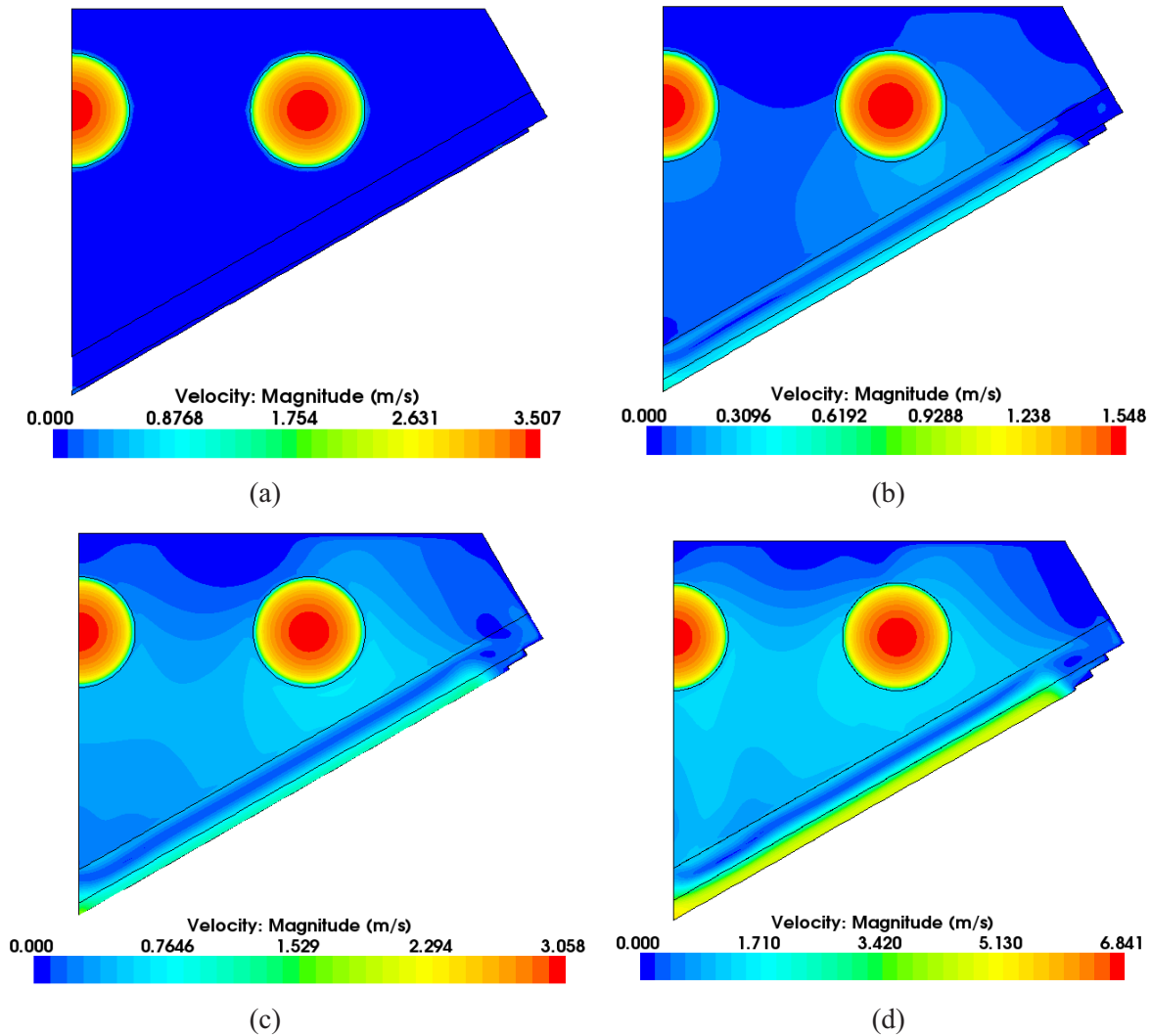
Figure 5-33. Velocity magnitude in horizontal gap for the (a) 2-2 mm/LF case, (b) 6-2 mm/XLF case, (c) 6-2 mm/LF case, and (d) 10-2 mm/HF case.

Flow in a bypass apparatus that includes both coolant channels and bypass flow gaps, representative of a graphite block in a prismatic HTGR, has been modeled using CFD. Vertical gaps that occur laterally between blocks vary from 2, to 6, to 10 mm. Horizontal gaps between blocks vary between 2 and 10 mm. Inasmuch as the scale is a factor of 2 greater than actual scale, these gaps are twice those that would occur in the reactor. Flow in the gaps is laminar for the five lower flow cases and transitional and turbulent for the two high flow cases. The coolant channel flow is fully turbulent in all cases, except for the extra low flow case, where it is in the transitional regime. It was also found that while the velocity in the center of the junction of three converging gaps is higher because of lower resistance, the effect is rather insignificant. It was found that the flow in the vertical gap increases nonlinearly with an increase in gap width, that is, the gap flow increases by a factor of at least 15 while the gap flow area only increases by a factor of 3. This indicated the fact that the flow is a factor of both flow area and flow resistance (wall friction). Note that most of the information presented in this section is the subject of Johnson.[20]

5.5.3   CFD Analysis by KAERI

To develop a CFD model for analyzing the bypass flows through a prismatic core, CFD analyses have been performed for the bypass flow experiments scheduled at the INL's MIR test facility.

A CFD model has been constructed and used to perform preliminary computations of flow in the MIR scaled model. Because of the symmetry, the CFD model includes only one-sixth of the test section. The grid structures of the CFD model are shown in Figure 5-34, constructed by using ICEM CFD Version 11.0.[21] The grid on the inlet plane (Figure 5-34(a)) was extruded down to the outlet with deactivated solid regions. Figure 5-34(b) shows a side view of the grid structure with a magnified view on the bevel region. The bypass gap with fine meshes lies along the bottom edge and ends with steps that represent a gap controller in the MIR test section. The number of meshes at the narrowest gap was up to 30 to resolve laminar velocity profiles near the walls. Overall, the CFD model contains 7–10 millions cells, depending on the cases.
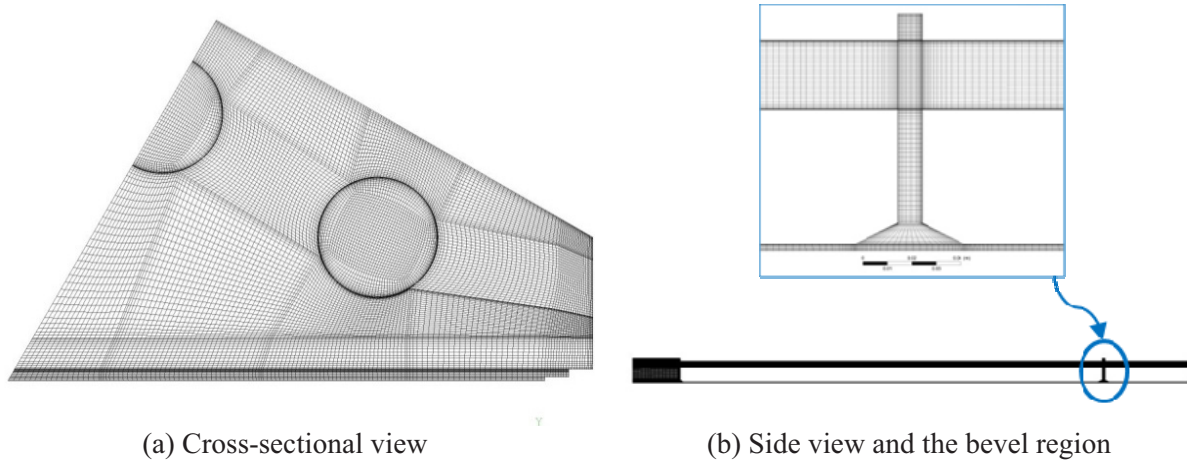
(a) Cross-sectional view   (b) Side view and the bevel region
Figure 5-34. Grid structures for one-sixth symmetric sector of 6-10 mm case.

Major flow characteristics of this geometry are the contractions at the coolant channel entrances and the narrow bypass gaps. It has been reported that the k-ω based turbulence models show better predictions for a flow with a sudden change of flow configurations than the k-ε based turbulence models. Among several k-ω turbulence models provided in the ANSYS CFX release 13.0,[22] the shear-stress transport (SST) k-ω turbulence model was selected because of its capability to properly predict the onset and amount of flow separation near entrances.

Since the bypass flow in the narrow bypass gaps (2 or 6 mm) is definitely laminar, it is necessary to suppress turbulence in those regions. For this purpose, a transition model with a specified intermittency (γ) was adopted, associated with the SST turbulence model. The laminar model was applied to the bypass gaps by specifying turbulent intermittency value as 0, while the turbulent model was applied to the other regions with the intermittency of 1 as shown in Figure 5-35.

The near-wall mesh node in the k-ω based turbulence model is assumed to be in the sublayer region, and a fine grid with y^+ values less than 2 is recommended. Figure 5-36 shows the y^+ distribution of the first nodes near walls. For all cases, y^+ values for the SST turbulence models were maintained below 1, except for some local regions in the inlet plenum.

The inlet mass flow was set to be 2.841 kg/sec for the one-sixth sector of the test section, based on the flow that can be obtained in the MIR facility using the current pump. Pressure outlet boundary conditions are used for the channel and gap outlets. The mineral oil fluid properties used are a constant density of 831.1 kg/m^3 and a constant dynamic viscosity of 0.011685 Pa-sec.
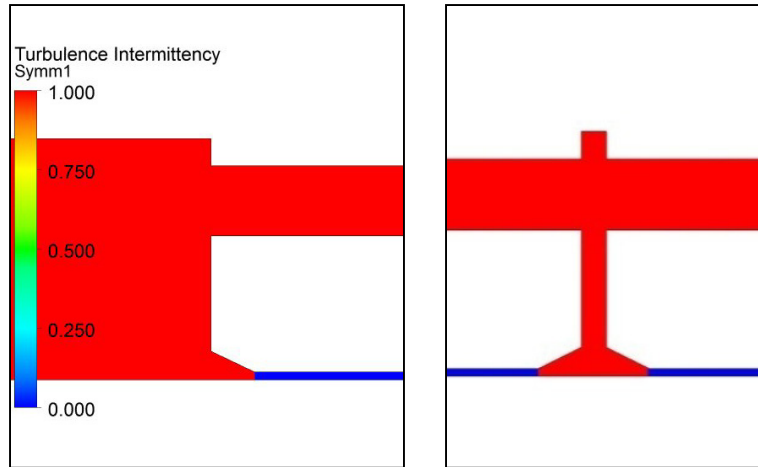
Figure 5-35. Intermittency setting.
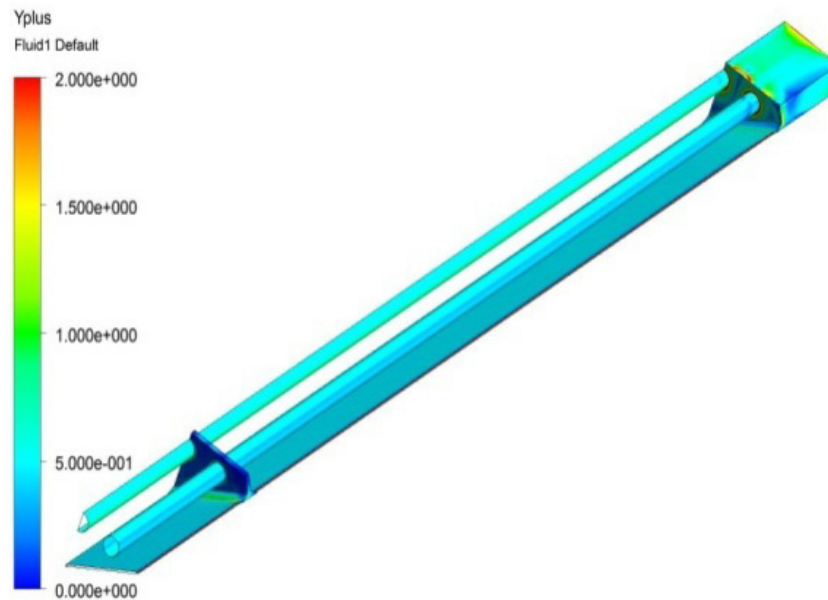
Figure 5-36. Wall distance (y⁺) distribution.

Figure 5-37 shows axial velocity profiles across the coolant channels in the upper fuel block at the locations of 0D, 25D, 45D, and 48D from the channel entrance. The velocity profiles show that the flow is essentially fully developed at the location of 45D. The maximum velocity at the centerline for the 2-2 mm case, which has a 2 mm bypass gap with a cross-flow gap of 2 mm, is higher than that of the 6-10 mm case, because the bypass flow rate increases with increasing bypass gap width.

Figure 5-38 plots the pressure drop across the test section through the bypass gap and whole coolant channel for a 6 mm bypass gap case with a cross-flow gap of 10 mm. The pressure values were obtained along the center axis of the coolant channel and along the plane of symmetry of the gap in its center. The pressures on the two data extraction lines are required to be the same at the inlet and outlets. As shown in the figure, the pressure near the entrance of coolant channels drops significantly (*vena contracta*), recovers, and then shows a lower gradient than seen for the gap region. In the second section, the pressure gradient is still steeper in the gap than in the coolant channel, but less steep than in the first section. This implies that the gap mass flow rate in the second section is less than in the first section.

(a) 2-2 mm case   (b) 6-10 mm case
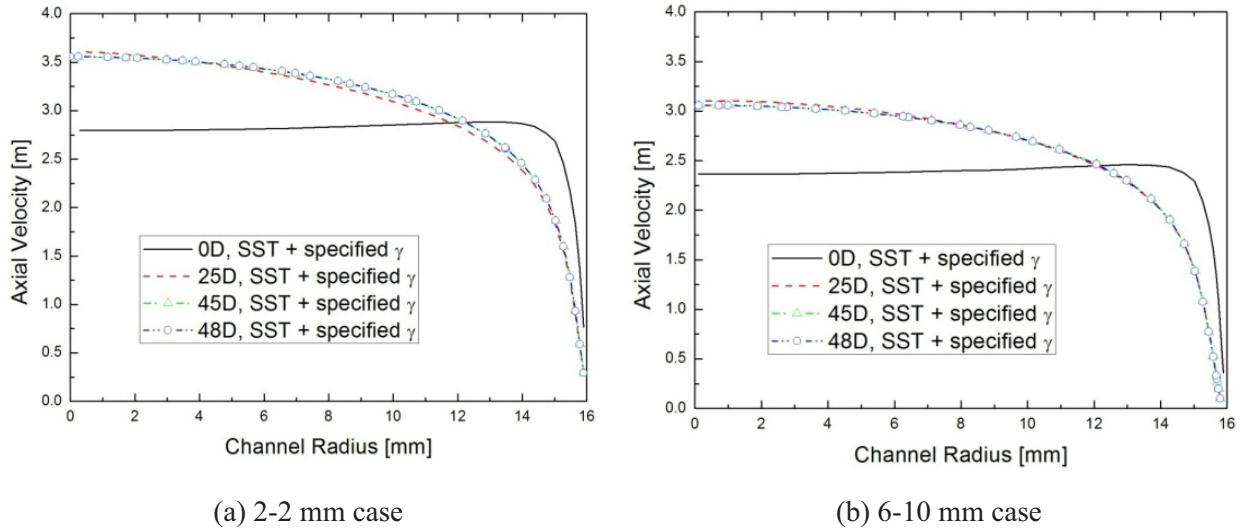
Figure 5-37. Axial velocity profiles of coolant channels.
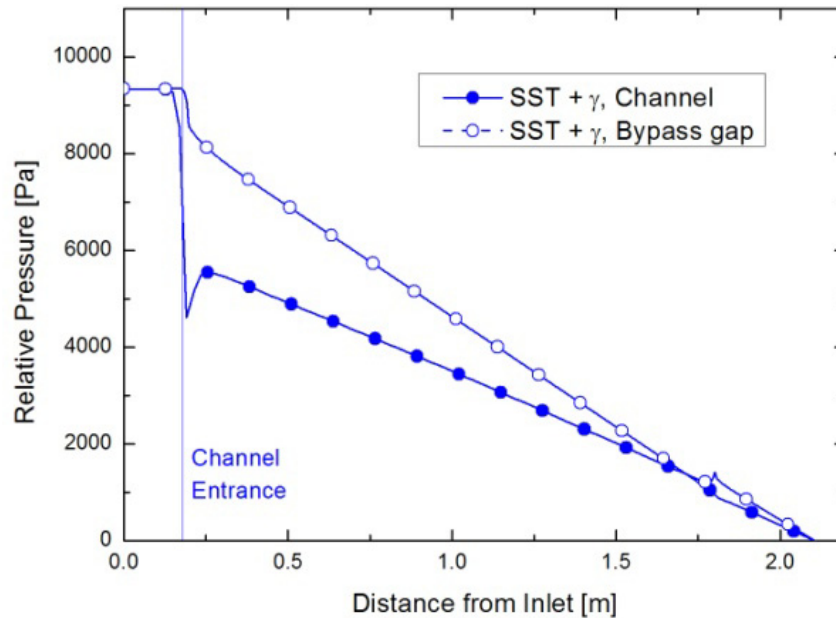
Figure 5-38. Pressure drop along stream-wise distance: 6-10 mm case.

Figure 5-39 and 4-40 show velocity and pressure contours for the 2-2 and the 6-10 mm cases respectively. Figure 5-39(a) show the velocity magnitude contours in the upper plenum. Velocity magnitudes at the channel entrance are not symmetric across the center line because of the influence of the bypass flows on the bottom. Figure 5-39(b) show a contour plot of the pressure at the mid-plane of the cross-flow gap for the 2-2 mm case. The pressure near the bypass gap is somewhat higher than near the coolant channels. This implies that lateral (cross) flows exist in the cross-flow gap from the bypass gap toward the coolant channels. In Figure 5-39(d) and 4-40, the maximum axial velocities in the bypass gap outlets appear at the junction of the three blocks.
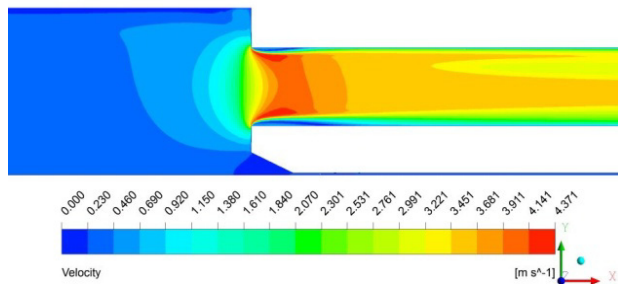
(a) Velocity magnitude in upper plenum
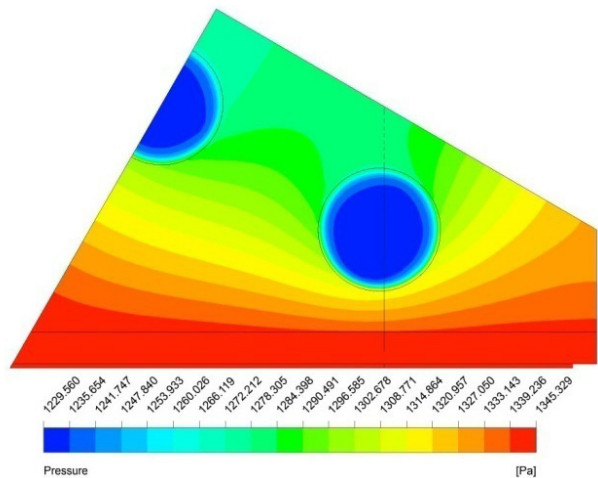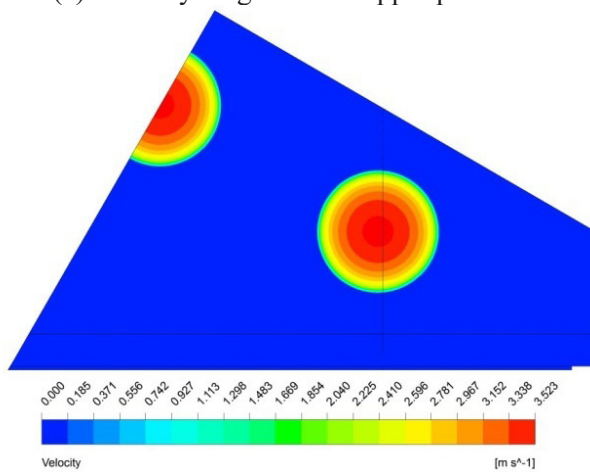
(b) Pressure at the mid-plane of cross-flow gap

(c) Velocity at the mid-plane of cross-flow gap
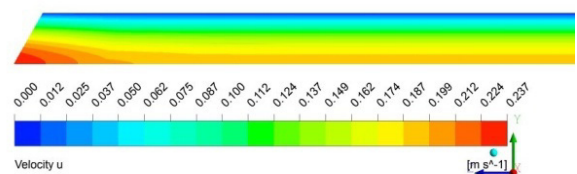
(d) Axial velocity at the bypass gap outlet

Figure 5-39. Results for 2-2 mm case

(a) Velocity magnitude in upper plenum
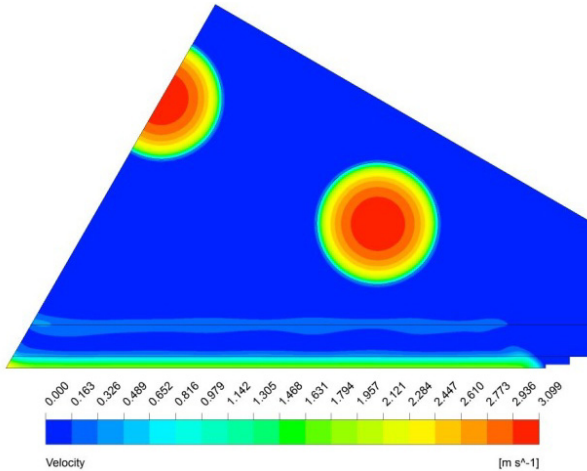
(b) Pressure at the mid-plane of cross-flow gap

75
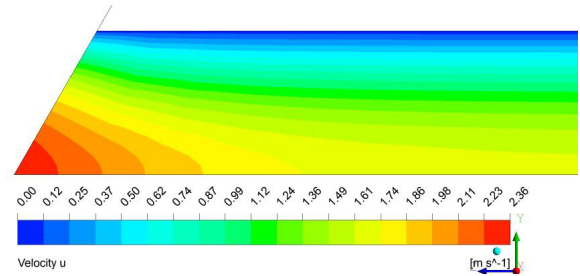
(c) Velocity at the mid-plane of cross-flow gap   (d) Axial velocity at the bypass gap outlet

Figure 5-40. Results for 6-10 mm case.

5.5.4   Code-to-Code Comparison

Before the MIR experimental data available, a blind benchmark comparison is made between CFD analyses of INL and KAERI. Commercial CFD codes used are STAR-CCM+ by INL and ANSYS CFX13 by KAERI. Table 5-7 summarizes CFD methods selected by both. The four cases of gap size combination considered were 2-2, 2-10, 6-2, and 6-10 mm. The former digit means bypass (vertical) gap and the latter is for cross (horizontal) gap.

Table 5-7. Comparison of CFD methods used in KAERI and INL calculations.

	KAERI	INL
CFD code	ANSYS CFX 13	STARCCM+ v. 5.02.009
Turbulence model	SST model with automatic wall function method	K-ε model with 2-layer wall function method
Laminar treatment	Turbulence intermittency control in gap regions	Turbulence suppression in gap regions
Mesh number	5.2–6.6 million cells	4.2 million cells
y+ at channel wall	<1	<1

Pressure distributions along the centerline of full coolant channel and gap channel are compared in Figure 5-41. The similar magnitude of pressure drop occurs at the full coolant channel entrance. The KAERI's pressure ripple at the entrance shows the existence of Vena Contracta by flow separation, but not INL. Similar magnitude of pressure difference between the channel and gap is observed.

Figure 5-42 compares velocity profiles plotted according to the law-of-the-wall at the location of 48D from the channel entrance at which the flow is fully developed. In the viscous sublayer ($Y^+ < 11$), the INL result shows very good agreement with the analytic profile as Y+ decreases. The KAERI result deviates from it slightly. In the log-layer (Y+>11), the velocity profile should follow the universal log-law as Y+ increases. The profile shapes in the log region differ from each other. The change of velocity profile from the viscous sublayer to the log-layer occurs more quickly in INL than in KAERI, making the earlier decrease of INL velocity slope in the region where Y+ > 100.
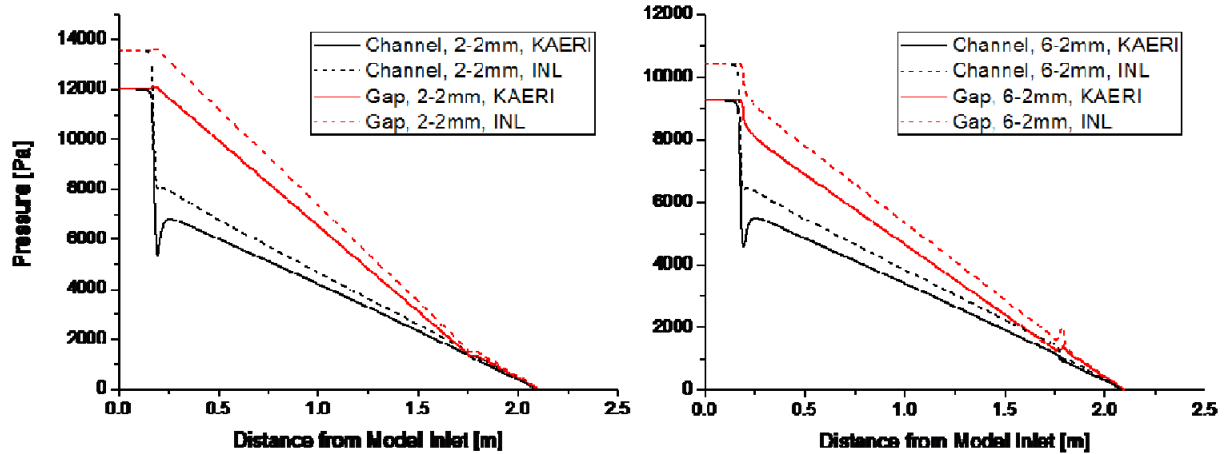
Figure 5-41. Pressure distributions along the centerline of full channel and gap.
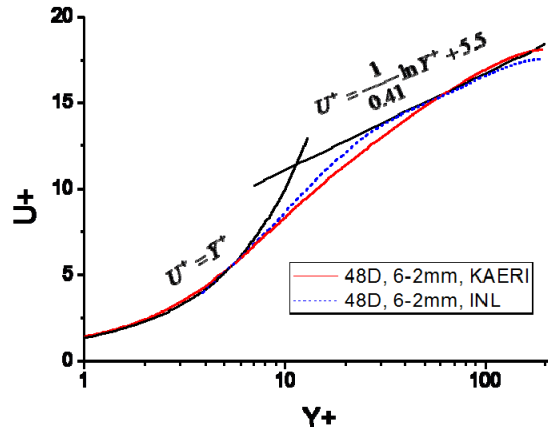
Figure 5-42. Comparison of the law-of-the-wall velocity profile in fully developed region

Table 5-8 compares and summarizes critical parameters for bypass flow prediction. The calculated Re numbers for all cases indicate that the flow is surely turbulent in the coolant channels and laminar in the gap channel. The INL model predicts higher total pressure drop across the CFD domain than the KAERI model. The reduction of gap flow fraction from the first gap to the second one implies that there is cross flow from the gap to the coolant channel. Larger cross flows are predicted in the INL results for the 6 mm bypass gap case.

Table 5-8. Comparison of critical parameters.

	2-2 mm		2-10 mm		6-2 mm		6-10 mm	
Cases	KAERI	INL	KAERI	INL	KAERI	INL	KAERI	INL
Mass flow (kg/s)	2.841	2.841	2.841	2.841	2.841	2.841	2.841	2.841
$Re_{channel}$ 1st block	6399	6387	6380	6390	5446	5440	5435	5400
Re_{gap} 1nd block	29	31	33	31	511	524	520	543
Total pressure Drop (Pa)	12023	13560	12227	13560	9257	10420	9257	10600
Gap flow 1st block (%)	0.88	0.97	1.00	0.96	15.4	15.6	15.7	16.2
Gap flow 2nd block (%)	0.56	0.61	0.65	0.65	14.4	13.4	14.1	12.4

5.6   GAS-NET Code and Others (ANL)

The work performed at ANL during the project focused on the development and validation of models for the GAS-NET computer code. This code solves the mass, momentum, and energy equations in a network formulation for the prediction of temperatures and flows in the prismatic gas-reactor core.

5.6.1   Gas-Net Model Development and Validation—First Two Years

The work performed at ANL focused on the development and application of the GAS-NET computer code for the prediction of temperatures and flows in the prismatic gas-reactor core. There were two main activities relevant to the I-NERI: adding to the capability of GAS-NET and validating models in GAS-NET by comparing calculations with experimental data. Each of these activities is summarized in the subsequent paragraphs.

5.6.1.1   New Features and Capabilities of GAS-NET

During the first year of the project the conservation equation specification and the numerical solution scheme for the GAS-NET code were complete. During the second year, a number of features and capabilities were added to improve the ease with which the user is able to set up a problem for solution and the ease with which the solution can be evaluated. Some of the code models were also refined and updated for wider applicability to gas reactor design work.

5.6.1.2   Input File Template Generator

An input file template generator was developed to facilitate user preparation of his input deck. The user defines the size of his problem (number of rows of columns and number of blocks in a column) and the generator produces a text file with cell tokens inserted in the correct place and numeric placeholders for all cell variable value fields. This includes the fields associated with the specification of block dimensions, dropped cells, and cell boundary condition flags and process variable values. The numeric placeholders in the resulting template are edited by the user to reflect the core dimensions and boundary conditions specific to his particular problem. The template generator takes advantage of regular input file format structure to minimize what is otherwise an error prone and time consuming process of assembling an input file.

5.6.1.3   Output Visualization

Even small simulation problems with a few prismatic columns of blocks yield a solution with thousands of process variable values. A 3-D visualization capability was therefore developed to facilitate the analysis of such large output files. This capability makes use of the VISIT[23] software to view the solution. A post-processor was added to GAS-NET to prepare a vtk-formatted file that can be read by VISIT. This file contains a prismatic mesh as shown in Figure 5-43 and process variable values on the mesh.

Presently only graphite temperatures can be written to the vtk-formatted file. The code computes a single graphite temperature for each block, whether it be a fuel, fueled-control, reflector, or reflector-shutdown element. The user has the option of displaying graphite temperature as a zonal field where each block appears as a single temperature color or as a nodal field where smoothing and interpolating between blocks produces a temperature color field that varies in a continuous manner. In the nodal case, all twelve vertices of a block are assigned a temperature equal to the single temperature of the graphite block. At each vertex, which abuts up to five other vertices, the temperatures of all vertices are averaged to give a single temperature for the point of intersection.
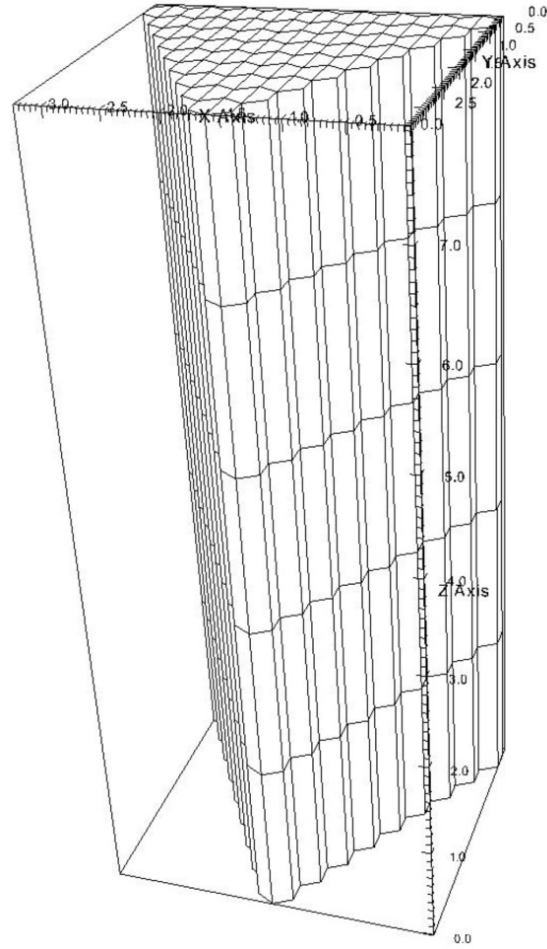
Figure 5-43. Mesh for prismatic reactor core 60-degree symmetry section.

5.6.1.4   *Pressure Loss Correlations*

The pressure loss correlations were reviewed in the light of experiments that were to be simulated this fiscal year. On the basis of this review the modeling of axial gap losses, entrance and exit losses, and cross flow losses was revised. The resulting implementations are described below.

With respect to the axial gap losses, the axial gap is now modeled as a thin rectangular duct compared to its earlier representation as a circular tube with the equivalent hydraulic diameter. The correlation of Idelchik[24] for a rectangular duct is used.

With respect to entrance and exit losses, the coolant flow exiting either an element coolant hole or an interelement gap into a plenum region encounters an abrupt change in channel area and an associated pressure loss. If the channel cross-sectional flow area in the channel is A_1 and the plenum is A_2, the pressure loss is given by Streeter[25] as

$$\Delta P = \left(1 - \frac{A_1}{A_2}\right)^2 \frac{1}{2} \rho v_1^2$$

(1)

where v_1 is the average coolant velocity in the channel.

A simplifying assumption is made in calculating local expansion coefficients. The area of the holes (gaps) is assumed to be the fractional area occupied times the total plenum area. Thus, if the holes and gaps occupy areas

$$A_{1-hole} = \sum_{i=1}^{n_{col}} n_{hole-col\,i}\, A_{hole-col\,i} \quad \text{and} \quad A_{1-gap} = \sum_{i=1}^{n_{gap}} A_{gap\,i}$$

(2)

respectively, then the plenum area associated with the holes is

$$A_{2-hole} = \left(n_{col} A_{col} + A_{1-gap}\right)\left(\frac{A_{1-hole}}{A_{1-hole} + A_{1-gap}}\right)$$

(3)

and with the gaps is

$$A_{2-gap} = \left(n_{col} A_{col} + A_{1-gap}\right)\left(\frac{A_{1-gap}}{A_{1-hole} + A_{1-gap}}\right).$$

(4)

At any particular hole or gap the entrance pressure loss is calculated from

$$\Delta P = K_e\, w^2.$$

(5)

where from above

$$K_e = \left(1 - \frac{A_1}{A_2}\right)^2 \frac{1}{2\rho A_1^2}$$

(6)

and where A_1 and w are specific to the local hole and gap. A similar development is used to represent contraction losses at the entrance to the core.

With respect to the cross-flow losses, at any axial level, a pressure gradient can exist between the element coolant channels and the neighboring interelement gaps. If a gap is present between stacked elements, a leakage flow will occur between these two locations. The magnitude of the leakage flow is a function of the pressure drop characteristics of the flow path. The geometry of the path is complex but has the general form of an abrupt contraction, followed by a channel, and finally an abrupt expansion. Two correlations exist in the open literature for estimating this pressure loss. It is important to note that each correlation is specific to a fuel element of specific dimensions. Both correlations were implemented in the GAS-NET code.

The pressure loss correlation by Groehn[26] was evaluated for use in modeling lateral leakage between stacked blocks. In the Groehn experiments, coolant was drawn laterally from an infinite plenum into a wedge-shaped opening at the top of a fuel element and down the length of the element coolant holes. While the basic features of the gap between two stacked elements in the Groehn experiment match those experiments of interest (air at near standard conditions and a gap opening of the size of a few mm in the SNU Multi-Block Test Facility), other features differed (wedge rather than plane gap geometry, different element dimensions, and flow from gap to channel rather than the reverse). The data in Groehn did, however, cover several gap thicknesses and gap flow areas. The loss coefficient correlation is

$$\xi = \frac{\Delta P}{1/2\rho u^2} = 3.58\left(\frac{a}{D}\right)^{-2.3} 6.33\left(\frac{A_{gap}}{a \cdot l}\right)^{-1.68}$$

(7)

80

where ρ is the coolant density, a is the nominal gap size, D is the coolant channel diameter, A_{gap} is the uncovered area along the perimeter of the wedge shaped gap, and l is the length along an edge of a block. The two parameters on the right are (1) the ratio of gap size to coolant hole hydraulic diameter and (2) the ratio of total gap area to the gap of a single face.

There is some uncertainty associated with the second term in the above equation. The second term in the body of Groehn is referred to as the pressure drop divided by the dynamic pressure of the mass flow rate. However, in the nomenclature section, the denominator of the second term is shown to be linear in u. The latter is assumed to be a typographical error since the former translates as shown above.

The above correlation is incorporated in the code as follows. A momentum balance for flow in the horizontal gap between the axial coolant channel node and the gap node ignoring acceleration and entrance and exit loss terms gives

$$0 = P_{ax-chan}^{I_{ic-faces-gap.col}(i_{face}),k} - P_{ie-gap}^{I_{ic-faces-gap.gap}(i_{face}),k} - K_{leak\text{-}gap}^{i_{face},k}\, w_{leak\text{-}gap}^{i_{face},k}\, \left| w_{leak\text{-}gap}^{i_{face},k} \right| \tag{8}$$

where K is a channel friction-loss term whose functional dependence we derive. Since

$$\Delta P = \zeta\, 1/2\, \rho\, v^2 = \zeta\, \frac{w^2}{2\rho A^2} = K\, w^2 \tag{9}$$

then

$$K = \zeta\, \frac{1}{2\rho A^2}. \tag{10}$$

Kaburaki[27] also proposes an expression for the pressure loss in the cross-flow gap. This correlation is fundamentally better parameterized than that of Groehn so may, in the future, be more easily adapted for conditions other than those in Kaburaki's work. The pressure drop is given by

$$\Delta P = K\, \frac{1}{2\rho}\left(\frac{w}{A}\right)^2 = \frac{1}{2\rho}\Lambda\, w^2, \quad \Lambda = \frac{K}{A^2} \tag{11}$$

which appears as Eq. (4) in Tkizuka and Kaburaki,[28] where

$$\Lambda = \frac{1}{\delta^2}\left(\frac{C_1}{\delta\, \mathrm{Re}} + C_2\right) \qquad \text{and } \mathrm{Re} = \frac{4w}{\mu\, L} \tag{12}$$

and where w is the mass flow rate in the cross-flow gap, δ is the cross-flow gap thickness and L is the wetted perimeter of the gap. Kaburaki determined the values of constants C_1 and C_2 for a parallel gap from experiment data ($C_1 = 0.67$ m^{-1}, $C_2 = 3.13$ m^{-2}).

5.6.1.5   Thermal Models by Element-Type

The structure thermal models were refined this fiscal year to include models specific to fuel, fuel-control, reflector-shutdown, and reflector elements. The heat transfer models are described in Vilim.[29] A description of the nodalization of each element type is given below.

With respect to a fuel element, the temperatures in a fuel element at full power are primarily a function of the mass flow rate in the coolant holes. If coolant hole flow rate is uniform across the element, as is the case when there is no lateral leakage, all coolant holes will have the same flow rate; then the graphite and fuel temperatures should be uniform across the element. In this case the temperatures in the repeating region shown in Figure 5-44 on the left-hand side should be largely independent of location

within the element. When this is the case, the temperature in the fuel and in the graphite can be modeled by a single node that represents an average graphite and fuel temperature. While there is heat transfer at the outer faces of the block by convection to the interelement gap and by radiation to the neighboring block face, this heat rate is of the order only a few percent of block power. It is not expected to introduce a skewed temperature profile across the fuel element. This heat rate from the face of the element is modeled below using the element average graphite temperature as the driving potential.
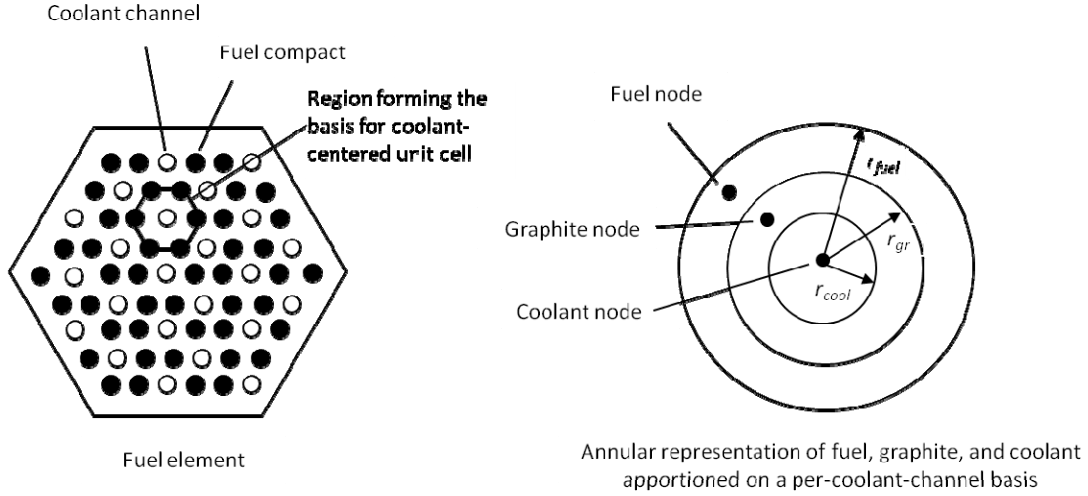
Figure 5-44. Fuel element transformed to coolant-centered unit cell.

The average temperatures are obtained by transforming the element with its 2-D array of coolant holes and fuel holes into the 1-D annular geometry shown in Figure 5-44 on the right-hand side. The Figure shows a coolant-hole-centered *unit cell* defined such that it is representative of the average fuel and graphite temperature in an element.

In the annular model, the radii of the coolant, graphite, and fuel regions are selected to preserve the areas in the 2-D fuel element matrix and where the number of such identical unit cells is equal to the number of coolant holes. The unit cell radii are defined through the following relations. The area of each of the distinct regions in the fuel element is

$$A_{hex} = \frac{3\sqrt{3}}{2} t^2 ,$$ (13)

$$A_{fuel} = n_{fuel} \pi r_{fuel-0}^2 ,$$ (14)

$$A_{cool} = n_{cool} \pi r_{cool-0}^2 , \text{ and } A_{gr} = A_{hex} - A_{fuel} - A_{cool}$$

where A is area, t is element face width, n is number, r is radius, and subscripts *hex*, *fuel*, *cool*, and *gr* represent hexagon, fuel, coolant, and graphite respectively, and the subscript *0* denotes a dimension before the transformation.

In the transformed geometry, the number of unit cells (annular pins) is set equal to the number of coolant holes while the radii of the coolant, graphite, and fuel annuli are chosen to conserve the respective areas in the original hexagonal fuel element. The radii of the three annular regions are then given by

$$n_{cool} \pi r_{cool}^2 = A_{cool} ,$$ (15)

$$n_{cool} \pi r_{gr}^2 = A_{gr} + A_{cool} , \text{ and } n_{fuel} \pi r_{fuel}^2 = A_{fuel} + A_{gr} + A_{cool}$$

where the radii on the left-hand side are those in the transformed geometry.

With respect to a reflector-shutdown element, the control element is assumed to be located in a reflector region and cooled by a single coolant hole. It is possible a significant temperature gradient can exist across the element if it is located in the outer reflector. The modeling of the reflector element below therefore takes this possibility into account. The element is nodalized as shown in Figure Figure 5-45. The six graphite nodes are assumed to be at the same temperature. But in determining the heat rate through the faces, each face is assumed to interact thermally with only the adjacent gap and block. In this way if the element is located in a region of the core with a significant temperature gradient, the effect of this gradient on heat transfer to the block is represented.
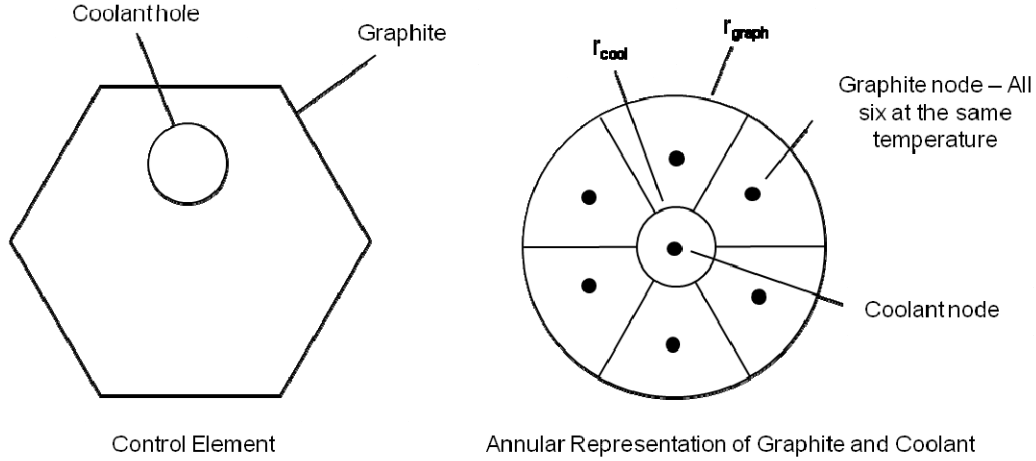
Figure 5-45. Geometry of transformed reflector-shutdown element.

In Figure 5-46 the radii are given, in analogy with the fuel element treatment above, by

$$A_{cool} = \pi r_{cool-0}^2 \tag{16}$$

$$A_{gr} = A_{hex} - A_{cool} \tag{17}$$

$$\pi r_{cool}^2 = A_{cool}$$

$$\pi r_{gr}^2 = A_{cool} + A_{gr} .$$

With respect to a reflector element, it is assumed to be a block of graphite as shown in Figure 5-46. The nodalization is analogous to the control element except that there is no coolant hole. Each graphite node interacts thermally with the gap adjacent the associated block face in a manner whose underlying basis is the same as described above for the control element. The graphite radius graphite in the transformed geometry is

$$\pi r_{gr}^2 = A_{hex} . \tag{18}$$
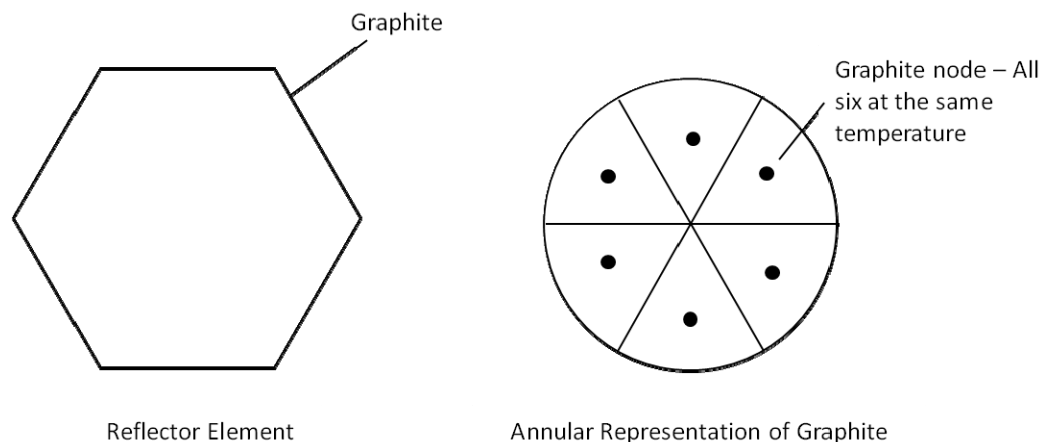
Figure 5-46. Geometry of transformed reflector element.

5.6.1.6   Validation

Validation studies were performed using data from a set of experiments performed at the Seoul National University Multi-Block Test Facility. The data permitted individual study of GAS-NET axial and cross-flow pressure drop estimates. The analysis, however, was complicated by several factors including test assembly entrance and exit losses in excess of coolant-hole losses and a dearth of pressure measurements for precisely allocating overall pressure loss amongst these individual losses.

5.6.1.7   SNU Facility and Experiments

The Seoul National University Multi-Block Test Section experiments[30] were used for an initial validation of the GAS-NET code. These experiments were performed in a scale facility with air at room temperature and pressure. The experiment test section consists of 11 parallel hexagonal columns, each consisting of three stacked elements. Figure 5-47 shows the test section viewed upstream of the inlet and from the side. The hexagonal sections seen in the view of the test section inlet contain holes (not shown) for coolant flow. The quantities measured were: mass flow rate out of each of the 11 columns, total mass flow rate through the test section, the inlet plenum pressure, and the pressure axially at six points along an intercolumn gap at the edge of the test section. These latter points appear as red dots in Figure 5-47.

Two experiment data sets were used for the comparison with GAS-NET. Both used an intercolumn gap of 2 mm as shown in Figure 5-48. In the first experiment, the cross-flow gap was blocked. Coolant flowed from the inlet plenum to the outlet plenum through the element coolant channel holes and the interelement gaps. In the second experiment, the stacked elements were separated to create a planar cross-flow gap of thickness 2 mm. Figure 5-47 shows a 1 mm gap.
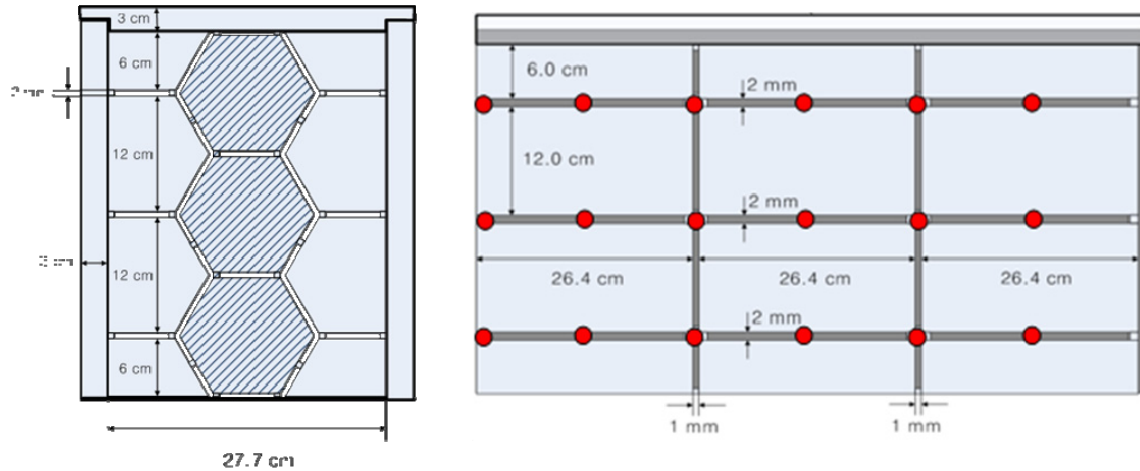
Figure 5-47. Seoul National University multiblock test section.

5.6.1.8   *GAS-NET Results*

The test section nodalization from the simulations is shown in Figure 5-48. The experiment test section was overlaid on a 60-degree section reference template. The solid black line in the Figure indicates the boundary of the test section. Only those cells mapping into the region within the solid black line were enabled. Boundary conditions were the mass flow rate measured at the outlet of each column, an average gap outlet mass flow rate computed from the difference of the total mass flow rate and the sum of the individual column outlet flow rates, and a uniform inlet plenum pressure.
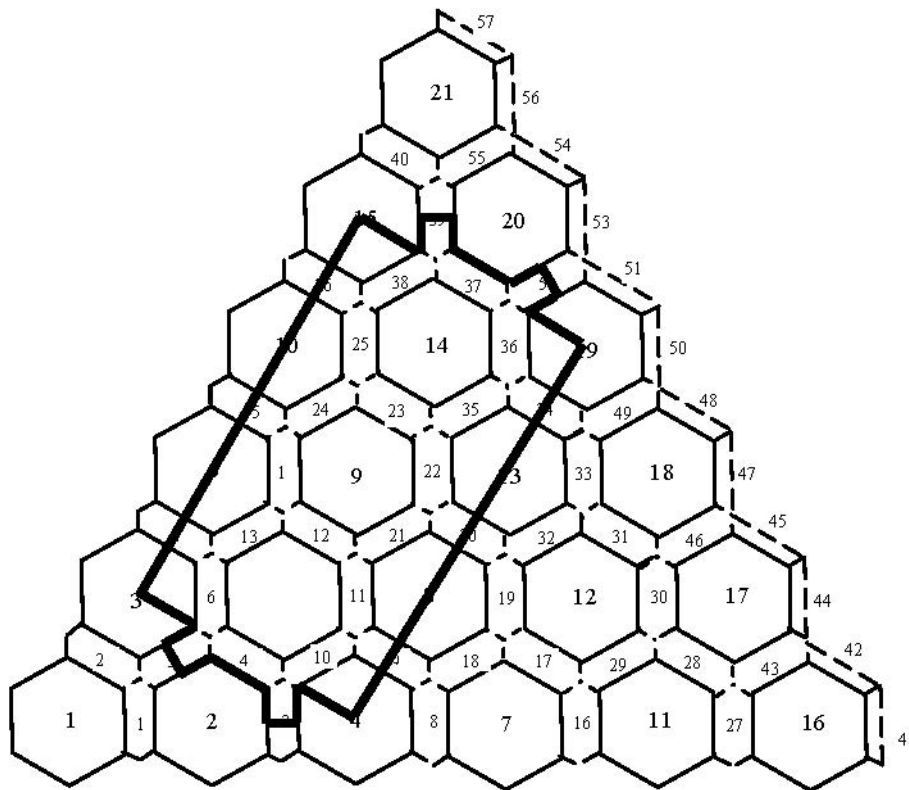
Figure 5-48. SNU multiblock test section overlaid on 60-degree core symmetry section template.

The code as run assumed zero form loss at the entrance to the gaps and holes in the columns. The particular set of boundary conditions selected obviated the need for use of the exit loss term in the simulation.

The predicted pressures in the instrumented gap for the first experiment (F3CG0) are shown along with measured values in Figure 5-49. The agreement is quite good and was obtained without an adjustment to the channel pressure loss correlations in the code.
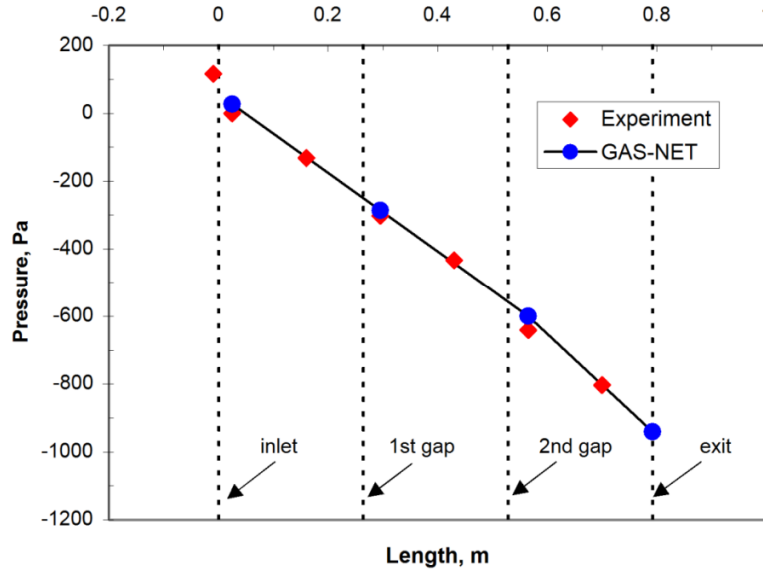
Figure 5-49. Edge-Gap pressure as a function of length for no stacked-element gap opening (Experiment F3CG0).

With good agreement obtained for axial pressure loss in the first experiment, the second experiment (F3CG2) represents a good test for the cross-flow gap correlations in the code. In this experiment, the pressure in the coolant channels at any axial location is greater than in the gaps resulting in an accumulating leakage flow from the former to the latter as one moves down the length of the test section. The predicted pressure drop along the instrumented side gap compared with experiment data provides an indirect measure of how well this flow has been predicted. The code was run first with the cross flow correlation of Groehn and then with that of Kaburaki. However, the agreement of predicted gap pressure with experiment was poor. The pressure drop in the first case was under predicted and in the second case it was over predicted. Figure 5-50 shows the result after the Groehn cross flow pressure loss correlation was adjusted by a single multiplicative factor in an attempt to achieve agreement with the data. The code is able to reproduce this data quite well. The relative magnitudes of the predicted cross-flow mass flow rates at the stacked-block gaps are shown in Figure 5-51.

These comparisons of experiment data suggest that neither the Groehn nor the Kaburaki cross flow correlations represent well the flow resistance of the 2 mm gap in the SNU test section, which is not unexpected because the flow field in the gap depends in a complex way on the specific geometry and dimensions of the element (number and diameter of coolant channel holes, and flat-to-flat width). Each of the Groehn and Kaburaki correlations are based on element geometry and dimensions different than those of the SNU Multi-Block test section. More generally, there is large experimental uncertainty in the pressure loss at the entrance to the gaps and holes in the columns at the inlet plenum. The pressures in this region were not extensively measured. But these losses establish the pressure differential developed along the length of the test section between holes and gaps. The inlet losses indirectly drive the cross flow. Until these losses can be estimated with greater confidence, we cannot be confident of the predicted cross flow.
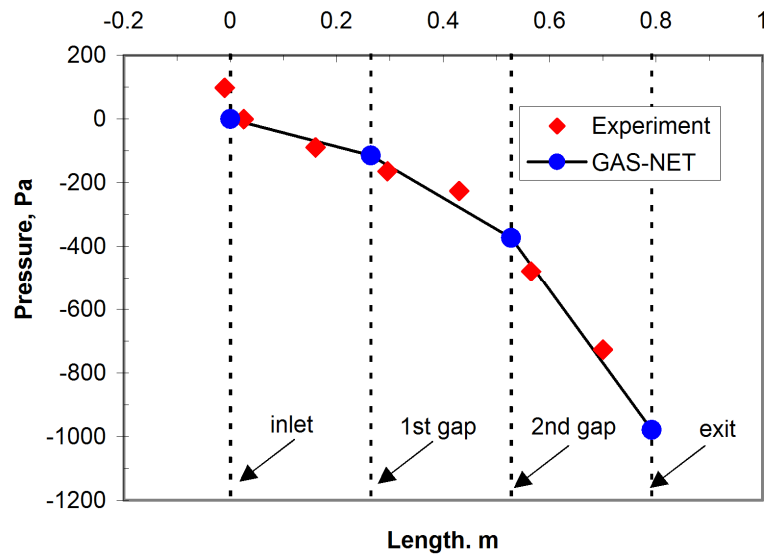
Figure 5-50. Edge-gap pressure as a function of length for stacked-element gap opening of 2 mm (Experiment F3CG2).
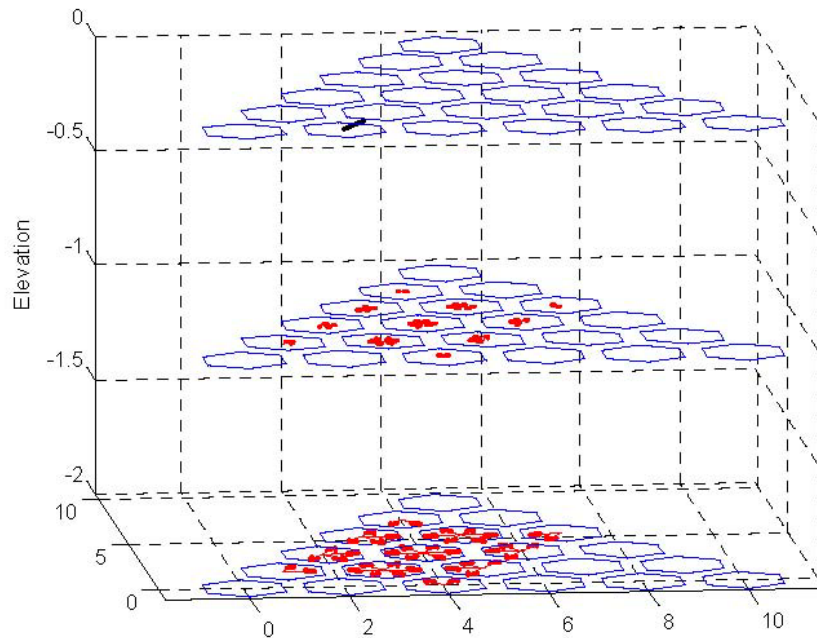
Figure 5-51. View of cross flow leakage in 60 degree symmetry section from GAS-NET as a function of length for stacked-element gap opening of 2 mm. Inlet at top.

A measure of how well the Groehn and the Kaburaki cross flow correlations represent the data is provided by comparing the value of $K' = \Delta P/(1/2\,\rho\,v^2)$ obtained from Groehn and Kaburaki with the value of K' obtained by forcing GAS-NET to fit the data as described above. The latter had a value of 16. The value from Groehn was 2000 (which is ballpark in agreement with his Figure 2) and 0.016 from Kaburaki.

5.6.2   Summary and Conclusions

The work performed at Argonne National Laboratory during the first 2 years of the project focused on the development and application of the GAS-NET computer code for the prediction of temperatures and flows in the prismatic gas-reactor core. There were two main activities: adding to code capability and validating models in the code by comparison with experiment.

Capability was added to facilitate ease of use of the code and to improve on existing models in the code. This work included the following. An input file template generator was created to semiautomate the process of preparing an input deck. The code output capability was extended to include the writing of a file in a format for display of temperatures using the VISIT 3-D visualization software. The structure thermal models were refined to include models specific to fuel, fuel-control, reflector-control, and reflector elements. This included addressing the geometry-specific heat transfer and pressure drop. Pressure drop correlations were updated for axial channel flow, cross flow, and entrance and exit losses.

Validation studies were performed for GAS-NET using data from a set of experiments performed at the Seoul National University Multi-Block Test Facility. The data permitted individual study of GAS-NET axial and cross-flow pressure drop estimates. The analysis was complicated by several factors, including test assembly entrance and exit losses in excess of coolant-hole losses and a dearth of pressure measurements for precisely allocating overall pressure loss amongst these individual losses. Despite these weaknesses, it appears gap pressure loss is predicted to within 10%. It also appears that neither the Groehn nor Kurbaki cross-flow correlations do an acceptable job in predicting the loss for the experiment-specific geometry. The results indicate that the cross-flow leakage loss is highly dimension and geometry-specific.

5.6.3   Gas-Net Model Development—Final Year

R&D focused on both extending the models related to fluid flow and heat transfer. In addition, a number of validation calculations were performed. The work associated with these activities is summarized below.

5.6.3.1   Fluid Flow

The channel loss correlation in GAS-NET was extended from a single Blasius-type model for all channels to a model specific to each of the four channel types and at each block level. The channel types are block coolant hole, axial flow in intercolumn gap, lateral flow in intercolumn gap, and lateral leakage flow between two stacked blocks. For each of these channels and at each axial level, a fit of the Darcy friction factor $f = C/Re^n$ to the Zigrang-Sylvetser correlation at a given surface roughness can be selected. The analytic fit to the Zigrang-Sylvetser correlation is plotted in Figure 5-52 for several representative values of the surface roughness parameter, ε/D. The fit has an average error of about 1% and a maximum error of 4.5% over the range $3000 < Re < 50,000$.

Losses other than channel losses can now be specified through a loss coefficient, K. The specification of three such losses is achieved through the GAS-NET input deck. They are (1) the loss associated with leakage from coolant holes at the edge of a block into the intercolumn gap, (2) the axial contraction/expansion loss in an intercolumn gap at the elevation where two stacked blocks meet and where the intercolumn gap width changes from top to bottom block, and (3) the loss associated with the mixing of flows at this same location where axial intercolumn flow and cross flow intersect. Figure 5-53 presents a simplified representation of these losses that is in a form that could be easily incorporated in a network code.
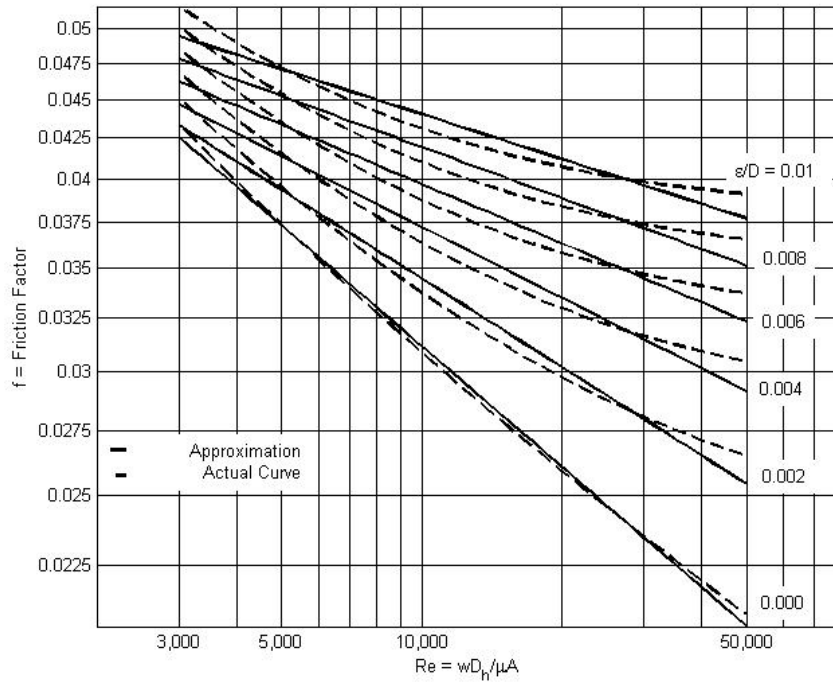
Figure 5-52. Darcy friction factor approximation to the zigrang-sylvetser correlation as a function of surface roughness.
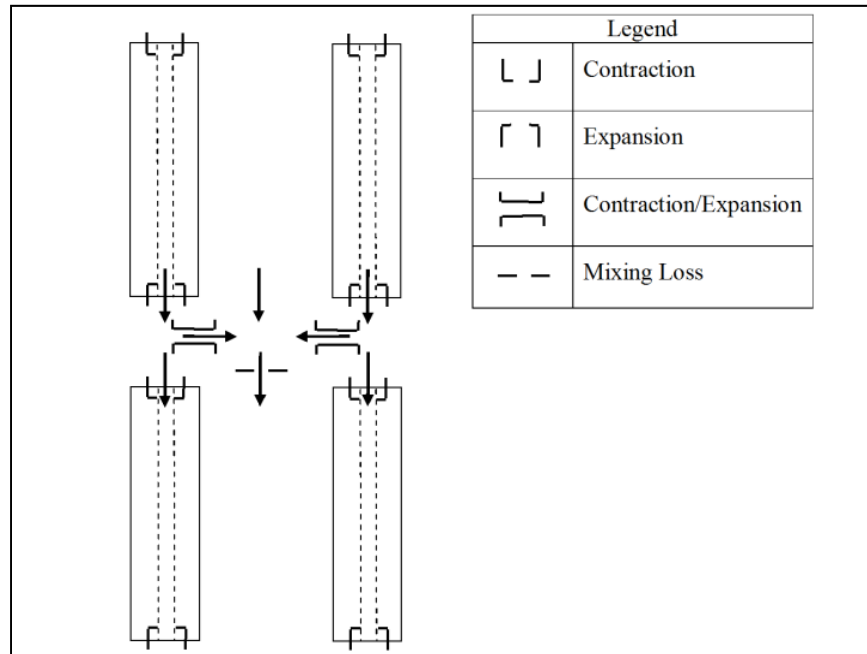
Figure 5-53. Simplified representation of mixing, contraction, and expansion processes among stacked blocks.

89

One possibility for including these losses in an assembled GAS-NET network is shown in Figure 5-54. The concept shown uses two code axial "levels" to represent the losses associated with a single layer of blocks in the prismatic core. A level is a layer of horizontal GAS-NET cells, while a cell is a basic modeling unit described in earlier work. Figure 5-54 illustrates how two layers of blocks stacked one on top of the other might be represented. Each layer of blocks is represented by a "physical" layer of cells on top of a "fictitious" layer of cells. The upper layer of cells is used to represent losses in coolant holes and intercolumn gaps in the block layer. The lower layer of cells is used to represent the entrance and exit losses associated with coolant holes and intercolumn gaps, the loss associated with leakage flow between stacked blocks, and the mixing loss at the junction of this leaked flow with inter-column gap flow.

The network concepts of Figure 5-54 were used to represent a multiblock fluid flow experiment performed at Seoul National University. The comparison of code results with this experiment is described later in this section.
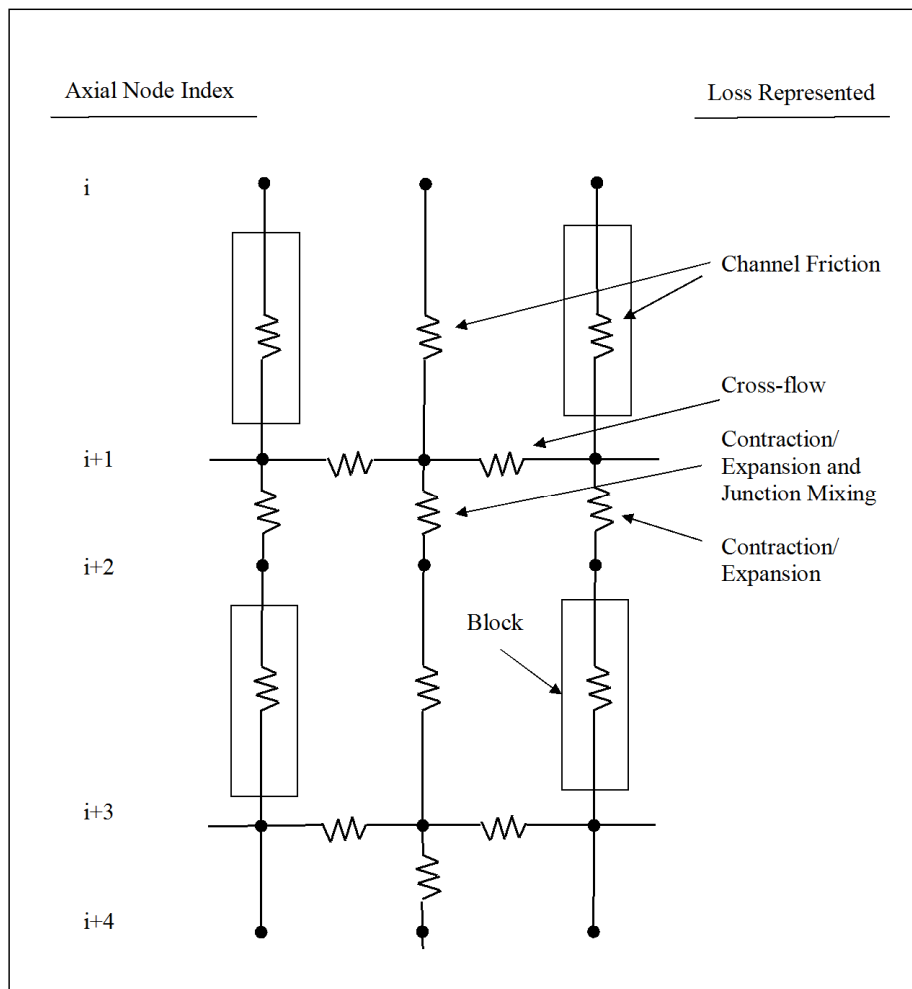
Figure 5-54. Network representation of losses for two layers of stacked prismatic blocks.

5.6.4   GAS-NET Model Development—Heat Transfer

In the prismatic-core gas reactor two types of graphite blocks make up the core. There are fueled blocks where the dominant heat transfer phenomena are internal heat generation and conduction of this heat to the block outer surface. There are then non-fueled blocks where the dominant phenomenon is

conduction of heat through the block in the radial direction. In the GAS-NET code a capability has been added to model these two heat transfer modes at the individual block level. The user specification for each block in the code input determines the heat transfer mode selected. The treatment of both types of heat transfer is described below.

In the case of a block with internal heat generation, the single 1-D annular construct shown in Figure 5-55 is used to calculate fuel, graphite, and coolant temperature. Temperature in the fuel and in the graphite of an element are each modeled by a single node that represents an average temperature This average is obtained by transforming the element with its 2-D array of coolant holes and fuel holes into a 1-D annular geometry. This defines a *unit cell* in such a way that it is representative of the average fuel and graphite temperature in an element. The radii of the three regions in the annular model are selected to preserve the areas in the 2-D fuel element matrix and where the number of such identical unit cells is equal to the number of coolant holes.
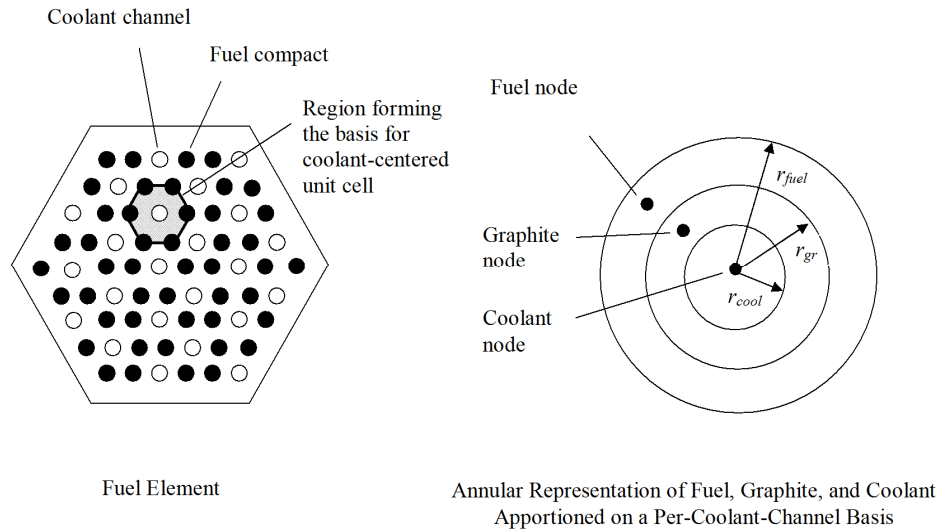
Figure 5-55. Transformation from block with internal heat generation to 1-D representation.

In the case of a block where radial conduction is dominant compared to internal heat generation an effective block thermal conductivity is derived. There are two cases. The first is where the block is in isolation. In this case the block interacts with the six neighboring faces through a nodalization shown in Figure 5-56 and effective graphite thermal conductivity derived from the 1-D radial heat transfer equation.
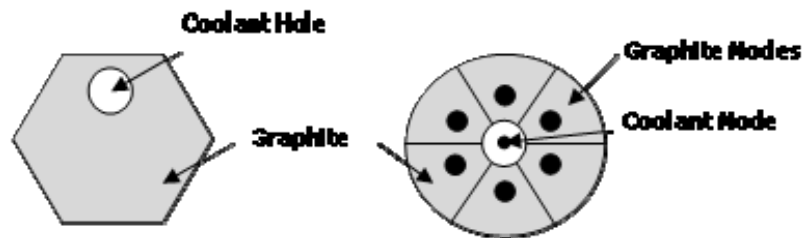
Figure 5-56. Transformation of isolated block to 1-D representation.

The second case is where the core layout is such that a region of blocks appears in a ring. In this case the blocks are transformed into the annular geometry of Figure 5-57.

In this case the flow of heat through an inner hex face, $q_{hexface}$, is related to the heat flux at the inside surface of the ring, q''_{ann}, by

$$q''_{ann} \, 2 \, \pi \, r_i \, L = 2 \, n \, q_{hexface}$$

and the inner surface temperature of the ring is given by

$$T_i = T_o + \frac{q''_{ann} \, r_i \, \ln\left(r_0 / r_i\right)}{k}$$

where r is radius, l is block length, n is number of blocks in the ring, k is thermal conductivity, and subscripts i and o represent inner and outer radius respectively.
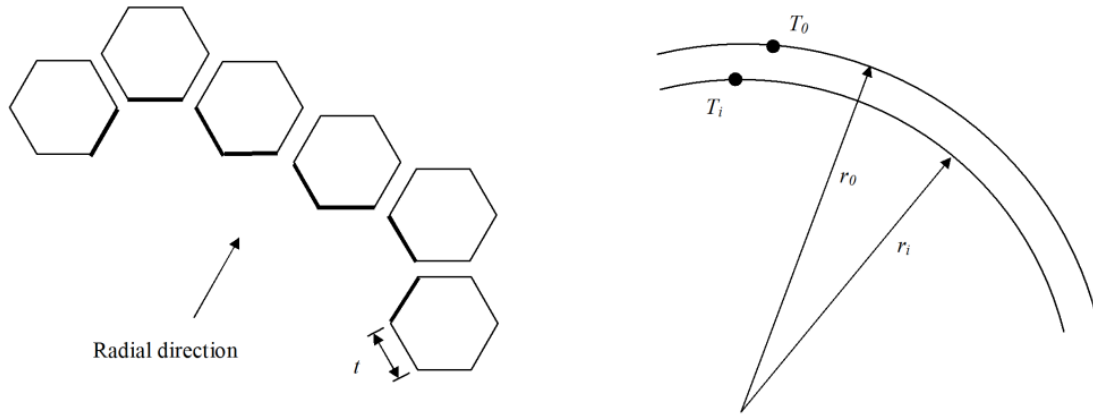
Figure 5-57. Transformation of a ring of blocks to a 1-D annulus representation.

5.6.5 GAS-NET Model Validation

Validation studies were performed for fluid flow models and for heat transfer models. The first study compared code predictions of bypass flow rates with data for an isothermal experiment performed in the Multi-Block Air Test Facility at SNU. An important phenomenon in this experiment was stacked block gap leakage driven by axial pressure gradients related to bypass gap size that varied by block axial elevation. The second study compared GAS-NET code predictions with RELAP results for temperatures in the MHTGR core at full power conditions. This activity began in FY10. In FY11 the comparison was refined with respect to the treatment of flow allocation boundary conditions and with respect to heat transfer modeling the in fuel and reflector blocks.

5.6.6 Validation of Fluid Flow Modeling

Validation studies were performed using data from the Multi-Block Air Test Facility located at Seoul National University. This is a scale facility with air at room temperature and pressure. Block dimensions are summarized in Table 5-9. Figure 5-58 shows the test section viewed from the side. The experiment test section consists of seven parallel hexagonal columns each consisting of four hexagonal stacked elements. The edge of a hexagonal element is shown in Figure 5-59. The quantities measured were: mass flow rate out of each of the seven columns, total mass flow rate through the test section, and the pressures in coolant holes and intercolumn gaps at a number of axial points along the test section.

Table 5-9. Block dimensions in SNU Multi-Block Test Facility.

Diameter of holes, m	0.008
Number of holes	90
Flat-to-flat distance, m	0.18

Edge length, m	0.104
Block length, m	0.4
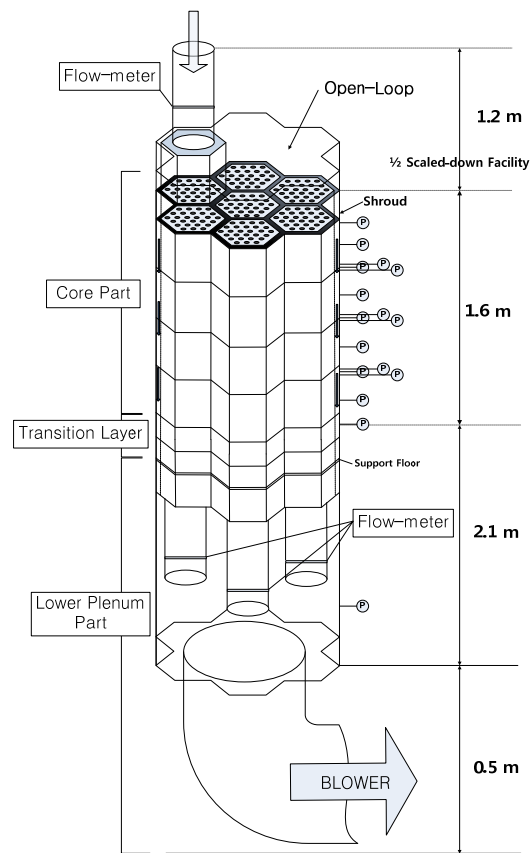
Figure 5-58. The Seoul National University Multi-Block Air Test Facility.
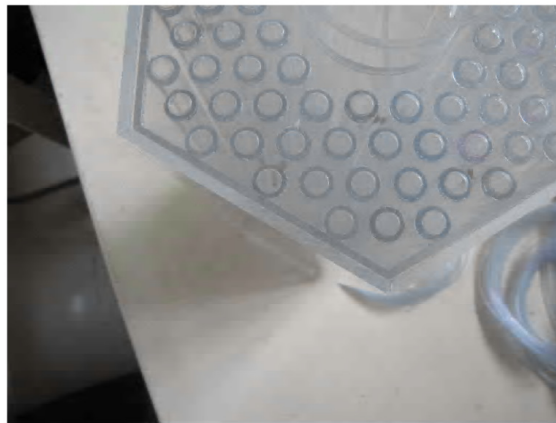
Figure 5-59. View of the edge of an hexagonal element.

Data was made available by Seoul National University for experiment BG6242-CG2. In this experiment the intercolumn gap size was varied with axial elevation. This variation leads to a pressure loss in the intercolumn gap at each stacked block interface level that varies by level and is significant compared to the channel friction loss. The loss is a combination of mixing and expansion/contraction

losses at the junction. As such, it represents a good test simultaneous test of the loss models for gap and hole axial flow, gap lateral leakage flow, and the loss models for contraction, expansion, and mixing at block interfaces. In this particular experiment coolant was permitted to leak from the bottom of the intercolumn bypass gap into the plenum area below. The vertical intercolumn gaps between stacked blocks were nominally 6, 2, 4, and 2 mm (top to bottom) intended to simulate the effect of change in block flat-to-flat distance over life and with shuffling of blocks during refueling. The horizontal gap between stacked blocks was 2 mm.

The "as assembled" gap widths as a function of block elevation are shown in Table 5-10. These values were deduced from measurements taken on the test section hardware. Figure 5-60 identifies the two gap types referenced in Table 5-10.

Table 5-10. Thickness of Inter-Column Gap by Block Number for Experiment R2-BG6242-CG2 Ordered top to bottom.

Block	Interior Gap (m)	Outmost Gap (m)
1	0.00602	0.00611
2	0.00209	0.00287
3	0.00430	0.00528
4	0.00215	0.00261
Transition	0.00212	0.00298
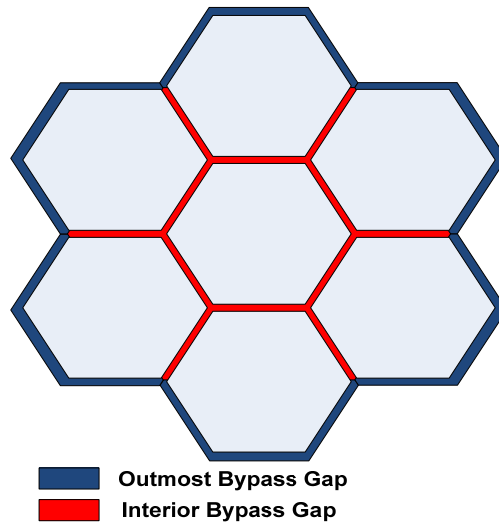
Figure 5-60. Definition of Bypass Gaps in Test Section.

In experiment R2-BG6242-CG2 two of the seven hexagonal columns contained no coolant holes and were meant to represent reflector blocks found in the prismatic core. The arrangement of the two column types is shown in Figure 5-61.
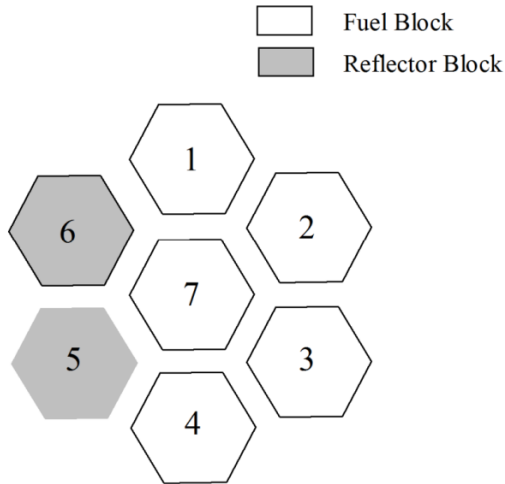
Figure 5-61. Plan view of test section columns in experiment BG6242-CG2.

A GAS-NET input deck was assembled to model experiment BG6242-CG2. The unique combination of gaps and columns was represented by overlaying the plan view of the test section over a 60-degree section reference template as shown in Figure 5-62. The solid black line in the Figure indicates the boundary of the test section. Those hydraulic cells mapping into the region within the solid black line were enabled. The test section axial nodalization is shown in Figure 5-63. The nodalization follows the scheme defined for GAS-NET and matches that of Figure 5-54. In Figure 5-63 the odd level index numbers represent physical layers and the even level index numbers represent the fictitious layers.
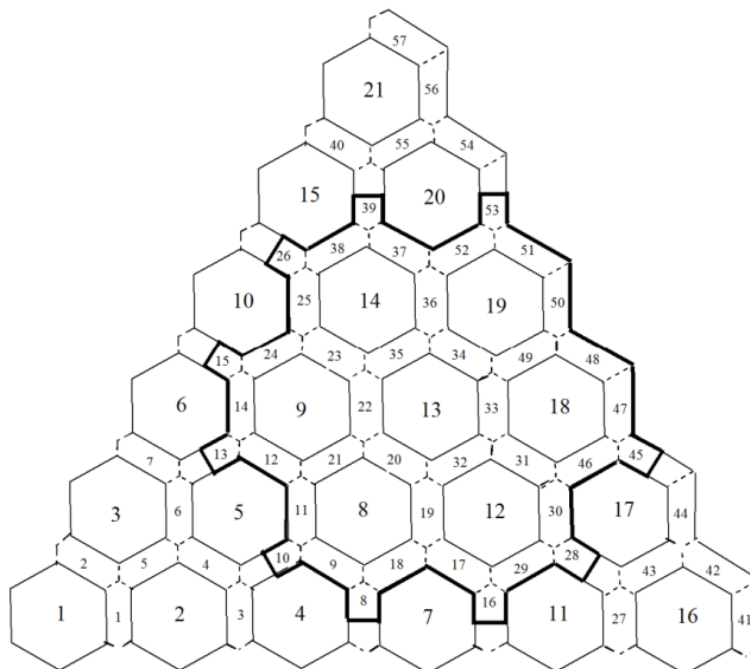
Figure 5-62. GAS-NET nodalization for Experiment BG6242-CG2.
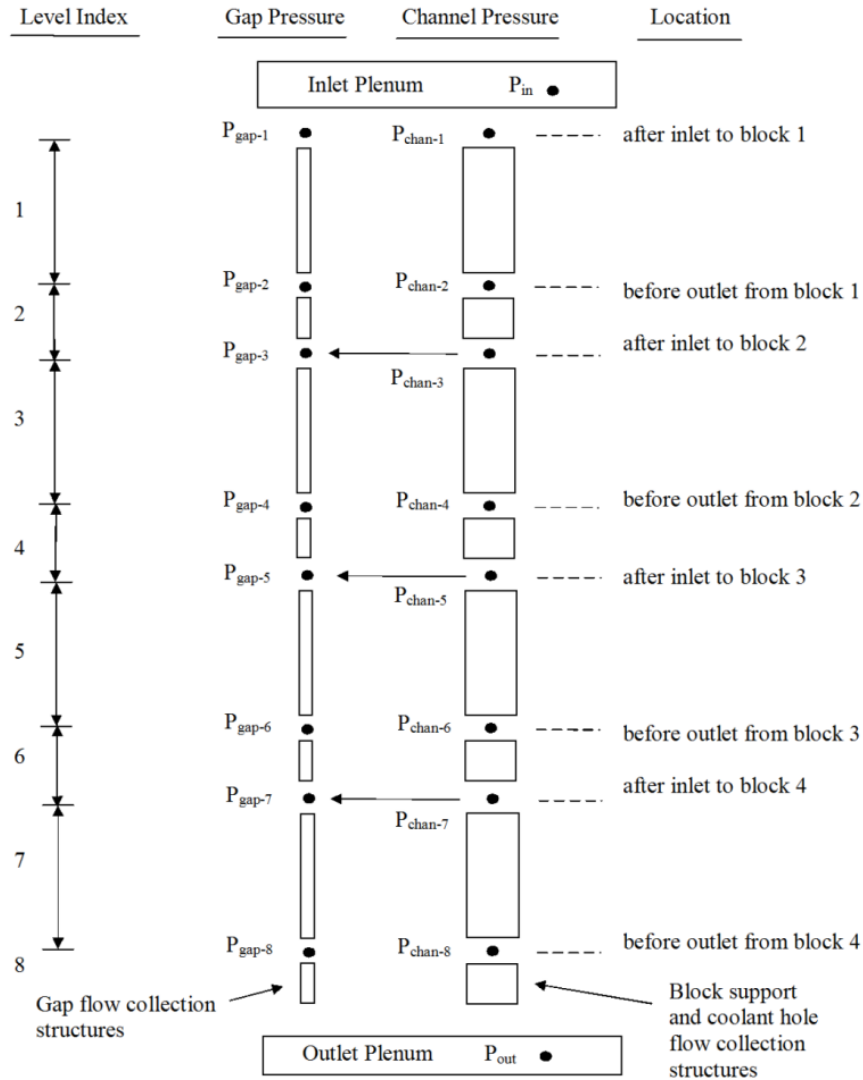
Figure 5-63. Axial gap and block hole pressures in network.

Boundary conditions in the GAS-NET simulation were the mass flow rate measured at the inlet to each column, an average gap inlet mass flow rate computed from the difference of the total mass flow rate and the sum of the individual column inlet flow rates, and a uniform inlet plenum pressure. The flow rates measured in the experiment are shown in Table 5-11.

The types of cells and models used to represent losses in the GAS-NET simulation for experiment R2-BG6242-CG2 are summarized in Table 5-12. The loss expressions are shown in Table 5-13. The corresponding values for the loss coefficient, K, are shown in Table 5-14.

Table 5-11. Measured mass flow rates for Experiment R2-BG6242-CG2.

Region		Inlet		Outlet	
Columns	1	0.15065		0.19230	
	2	0.14932		0.19587	
	3	0.14971		0.19295	
	4	0.15230		0.19187	
	5	-		-	
	6	-		-	
	7	0.14473		0.19327	
	Subtotal	0.74671	(67.7 %)	0.96626	(87.6%)
Gap Bypass*	Per channel	11.9e-3		4.57e-03	
	Subtotal	0.35658	(32.3%)	0.13703	(12.4%)
Test Section	Total Inlet	1.10329	(100%)	1.10329	(100%)

* Difference between test section inlet flow rate and sum of individual
column flow rates

Table 5-12. Pressure loss model by hydraulic cell type.

		Axial Friction Loss		Axial Contraction/ Expansion Loss		Mixing Loss at Gap Junction		Cross Flow Loss
		Axial Inter-Column Gap Cell	Axial Coolant Hole Cell	Axial Inter-Column Gap Cell	Axial Coolant Hole Cell	Axial Inter-Column Gap Cell	Axial Coolant Hole Cell	Stacked Block Leakage Cell
Axial Level	Block 2i-1 (physical)	$f = C/Re^n$	$f = C/Re^n$	NA	NA	NA	NA	NA
	Stacked block interface	NA	NA	NA	NA	NA	NA	No cross flow, cell disabled
	Block 2i (fictitious)	NA	No loss so $f = C/Re^n = 0$	K from Streeter	NA	NA	NA	NA
	Stacked block interface	NA	NA	NA	NA	K from Idelchik	NA	K from Kaburaki

Table 5-13. Pressure loss model expressions.

Loss type	Reference	Expression
Gap junction mixing	Idelchik	$K = 0 - 0.5$ for 90° Tee
Cross flow	Kurabaki	$K = l^2 \left(\dfrac{C_1}{\delta \, Re} + C_2 \right)$
Axial expansion	Streeter	$K = \left(1 - \dfrac{A_1}{A_2} \right)^2$
Axial contraction	Weisbach	$K = \left(\dfrac{1}{C} - 1 \right)^2$, $C = 0.63 + 0.37 \left(A_2 / A_1 \right)^3$

Table 5-14. Loss Coefficient Values for Experiment R2-BG6242-CG2.

Loss Mechanism		K	Notes
Leakage Cross Flow		3.0	
Gap Junction Mixing		0.5	
Gap Stacked-Block Contraction/ Expansion (top to bottom)	1	0.31 (6 mm to 2 mm)	peripheral gap
	2	0.25 (2 mm to 4 mm)	peripheral gap
	3	0.23 (4 mm to 2 mm)	peripheral gap
	4	1.0 (2 mm to exit)	peripheral gap
Sum of Gap Stacked-Block Contraction/Expansion and Junction Mixing	1	0.81 (=0.5+0.31)	interior gap
	2	0.75 (=0.5+0.25)	interior gap
	3	0.73 (=0.5+0.23)	interior ga
	4	1.0	interior gap)

The GAS-NET predictions for experiment R2-BG6242-CG2 are shown in Figure 5-64 and Figure 5-65 and Table 5-15. The data markers in Figure 5-64 and Figure 5-65 are located at elevations just after the entrance to a block and just before the exit from a block. In general, the correct trend among variables is observed. Figure 5-64 shows the block averaged pressure drop is in reasonable agreement. Figure 5-65 shows the intercolumn gap averaged pressure drop. The code under-predicts the pressure drop and fails to capture some of the features associated with pressure drop across the block gaps. The fraction of coolant bypassed at the outlet is predicted to be 15.3% compared to a measured value of 12.4%.
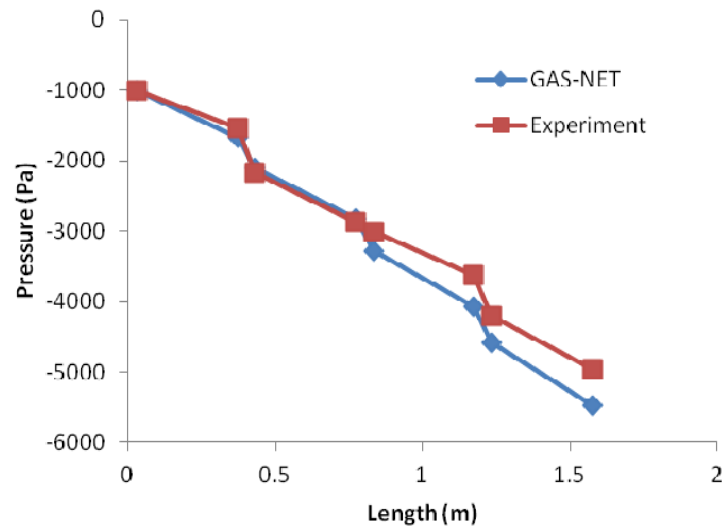
Figure 5-64. Average block coolant hole axial pressure distribution.
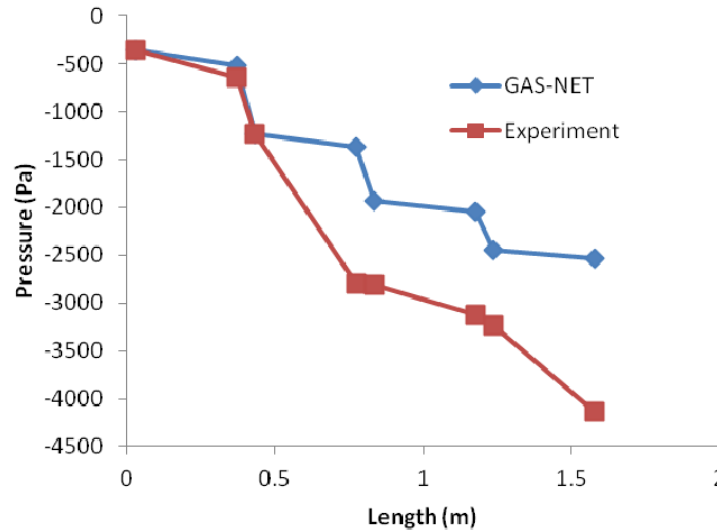
Figure 5-65. Average intercolumn gap axial pressure distribution.

Table 5-15. Fraction of coolant bypassed at inlet and outlet of test section.

		Experiment	GAS-NET
Inlet	Flow Rate (kg/s)	0.3566	–
	Fraction	32.3%	–
Outlet	Flow Rate (kg/s)	0.1370	0.1687
	Fraction	12.4%	15.3%

However, the above results must be properly qualified. Initial code calculations were performed with the loss coefficient values of Table 5-14. These proved to yield very poor agreement with the experiment data. The results described above were instead obtained by tuning the values of code loss coefficients to match the experiment data pressure drop values. This process was performed manually in an iterative fashion. The results are hardly converged as Figure 5-65 and Table 5-15 suggest. The tuned loss coefficients in the GAS-NET code for Experiment R2-BG6242-CG2 are characterized in rough by the following values: $K=0.2$ for the loss encountered in exiting a block and entering the next block; $K=21$ for the loss encountered between coolant exiting holes, leaking through the horizontal gap between stacked blocks, and then exiting into an intercolumn gap; and $K=5$ for the loss where an intercolumn gap flow merges with a stacked block leak flow and the combined flow moves on towards the next gap.

The following conclusion is drawn from the analysis of Experiment R2-BG6242-CG2. Significant future effort will be needed to generate loss coefficient values for network codes if these codes are to reliably predict the pressure losses encountered in prismatic cores.

5.6.7   GAS-NET Validation of Heat Transfer Models

The RELAP code has been applied to obtain best estimates for the MHTGR full-power, steady-state core temperatures and the transient response over many hours for the conduction cooldown accident. The MHTGR core layout is shown in Figure 5-66. The RELAP core thermal-hydraulics model, a 2-D cylindrical representation of the core lattice, provides a good approximation to the actual geometry as seen in Figure 5-67. Local effects that the code is not able to explicitly represent include the appearances of individual reflector and fuel shutdown elements and block-to-block heat transfer at the level of the individual block where the geometry is hexagonal faces rather cylindrical slabs.
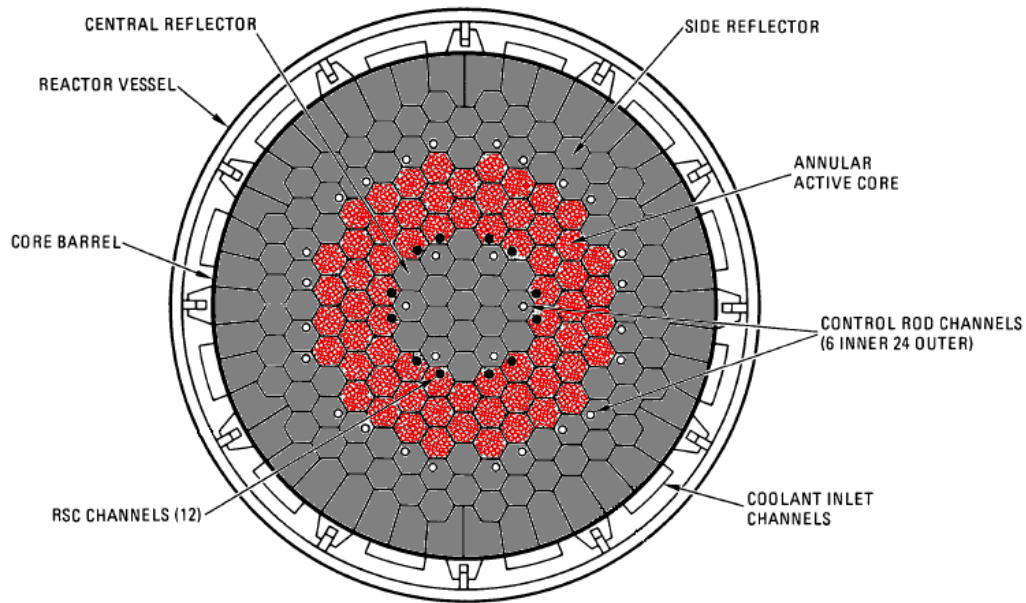
Figure 5-66. MHTGR core layout.
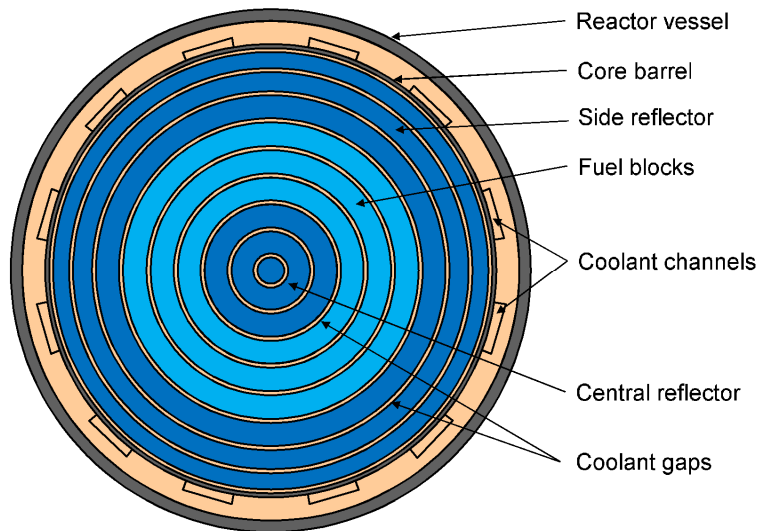
Figure 5-67. Annular representation of the MHTGR core layout.

The above local dependencies were evaluated and characterized using the GAS-NET code, which provides for a more detailed block-by-block representation of the core. The code was also used to examine the role of the following phenomena in the core temperature distribution:

- radiation heat transport between neighboring blocks, particularly in regions of high temperature gradients

- radial conduction through graphite block in regions of high temperature gradients

- convection heat transfer and its dependence on bypass gap size

- gamma heating in reflector regions

- laminar versus turbulent flow in thin intercolumn gaps or low flow control rod holes.

100

The comparison of GAS-NET against RELAP5 represents a validation of sorts as any differences must be understood and accounted for.

The MHTGR core operating conditions are nominal. The core dimensions and element counts together with the layout of the MHTGR core were taken from the preliminary safety information document at normal operational conditions. The configuration is shown Figure 5-48. The individual column powers were derived from the core nominal conditions. The derivations assume a single fuel column power and a single reflector column power. The reflector column power represents gamma heating and is taken on a unit volume basis (where volume is entire element volume as opposed to some subset of element materials) equal to 0.01 of fuel column power.

The core layout is well represented by the 60-degree symmetry section of Figure 5-68, given the periodic symmetry seen in Figure 5-66. This symmetry section reproduces the core layout exactly on a column-by-column basis. An exception occurs at the outer-most ring of reflector elements where a more regular arrangement of elements has been used in this work compared to the arrangement in the preliminary safety information document where the arrangement is dictated by the cylindrical shape of the core barrel. Also shown in Figure 5-68 are the individual columns that make up each of the nine RELAP column rings.
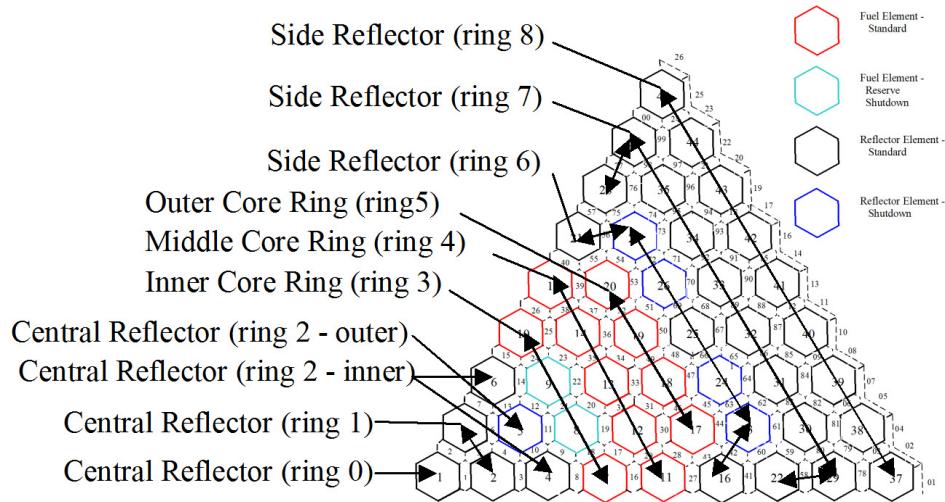
Figure 5-68. GAS-NET individual elements and RELAP ring definitions.

A main point of comparing results between the two codes was to characterize solution differences that arise as a result of the cylindrical core geometry assumed in RELAP5 as opposed to the individual block representation in GAS-NET. To facilitate the comparison of the role of multidimensional column-to-column heat transfer, the energy equation was solved for identical gap and coolant hole flow rates between the two codes as described in the previous section. No adjustment to the film heat transfer coefficient was made to account for surface roughness.

A flow boundary condition that matched RELAP as described above was used to decouple the thermal solution from the hydraulics in the GAS-NET runs. In general GAS-NET solves the mass, momentum, and energy equations simultaneously.

A temperature boundary condition was used to simulate the presence of the core barrel structure opposite the last row of reflector columns in Figure 5-68. A surface temperature of 295°C gave a core barrel heat rate of 730 kW, which was the value calculated by RELAP5.

The boundary conditions in the columns along the zero and 60-degree axes in Figure 5-68 were set to produce a zero heat flux across the vertical planes of these symmetry axes.

The axial power profile in the fuel and reflector elements was assumed uniform with height. A RELAP5 calculation showed that the graphite temperatures at the outlet were insensitive to the shape of the power profile. However, prediction of graphite temperatures along the axial length of the core requires use of a more representative power profile. All fuel columns were assumed to have the same power as were the reflector columns. The power in a reflector column, which is meant to represent gamma heating, was zero for the comparison between codes. The sensitivity of reflector temperatures to gamma heating was then later examined in separate GAS-NET runs.

The core was divided into 10 axial zones. The same nodalization ensured that the nodes used in comparing graphite temperatures between codes were identically sized, hence, the node temperatures were consistent spatial averages. Gap thicknesses were set equal between the two codes (inner reflector at 1.0 mm, fuel at 1.5 mm, outer reflector at 1.0 mm, and outer reflector/core barrel at 3 mm) for comparable convection heat transfer.

Generally good agreement was obtained between the two codes for the coolant flow distribution. To facilitate the comparison of the role of multidimensional column-to-column heat transfer, the energy equation was solved for the case where both codes used the same allocation of coolant among coolant holes and intercolumn gaps. The difference in column graphite temperature at the exit of the core in RELAP5 compared to GAS-NET is shown in Table 5-16 where the temperature rise along the axial length of the graphite column in RELAP5 is compared against GAS-NET. The fractional difference in the RELAP5 result with respect to GAS-NET is shown in the right-most column of the table. Generally good agreement on graphite temperature was obtained, except in the outer reflector region. This region at full power accounts for removal of roughly 3% of the total reactor power. Through a process of radial conduction of heat outward from the outer ring of fuel columns, heat entering this region is removed by convection in the intercolumn gaps and by conduction into the core barrel wall. GAS-NET is presently over estimating the resistance to outward radial heat flow through the outer reflectors compared to what RELAP5 predicts.

Table 5-16. Mapping of GAS-NET columns onto RELAP column rings and comparison of graphite temperatures.

RELAP Core Region	GAS-NET Column Numbers	Graphite Inlet to Outlet Temperature Rise		
		RELAP (°C)	GAS-NET (°C)	RELAP Difference (%)
Inner Reflector				
Ring 0	1	346	358	-3
Ring 1	2-3	375	368	2
Ring 2A (inner)	4,6	423	457	-7
Ring 2B (outer)	5	449	356	26
Active Core				
Inner Ring	7-10	521	544	-4
Middle Ring	11-15	532	534	-1
Outer Ring	17-20	488	497	-2
Outer Reflector				
Ring 6	16,21,23-27	371	320	16
Ring 7	22,28,29-36	242	147	64
Ring 8	37-45	122	56	116

A validation study of the original GAS-NET block element energy equation model was performed separate from the above MHTGR analysis. This study, described below, led to the distinction between the

heat transfer in a reflector element and in a fuel element and the associated development of corresponding heat transfer models.

The original GAS-NET model and a RELAP5-type annular ring model were evaluated by applying them to a simple conduction problem and comparing the solutions against a finite difference solution. For the single unheated block element in Figure 5-69, heat flux and temperature boundary conditions are imposed on the two inner faces. The resulting temperature distribution solved using a 2-D finite difference method is shown in Figure 5-70. The temperature on the two outside faces is compared among models in Table 5-17. The RELAP5-type model better approximates the finite difference model and led to development of a separate heat transfer model for unheated elements.
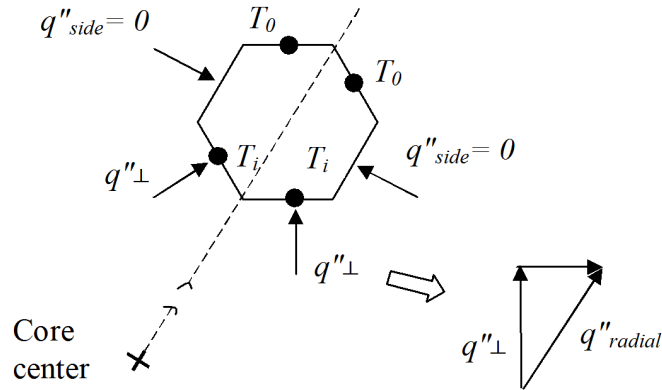
Figure 5-69. Heat conduction validation test problem.
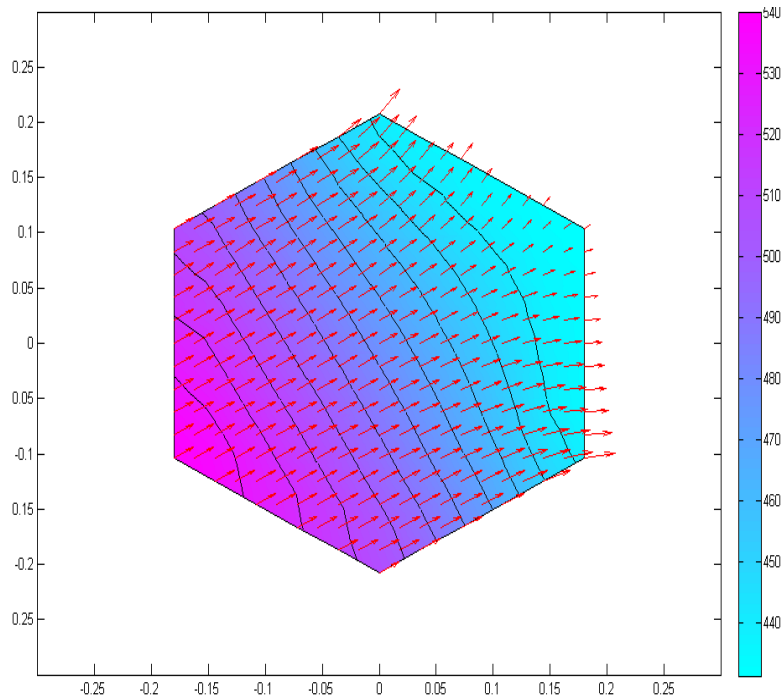
Figure 5-70. Finite difference solution to test problem.

Table 5-17. Comparison of solutions to test problem

Code Model	Boundary Conditions			Predicted	
	T_o (°C)	q''_{side} (W/m^2)	q''_{radial} (W/m^2)	T_i (°C)	$\Delta T = T_i - T_o$ (°C)
2-D Finite Diff	430	0	10^4	515	85
GAS-NET	430	0	10^4	458	28
RELAP	430	0	10^4	497	67

$k = 30$ W/m $T_o = 430$ °C $q''_{side} = 0$ W/m^2 $q''_{radial} = 10^4$ W/m^2

4. Planned activities

   None

5. Issues/concerns

   None

6. TASK 5

1. Task title and responsible lead

   Identification of Bypass Flow Reduction Measures and Their Experimental and Analytic Assessment, KAERI/ANL

2. Brief description of objectives

   Develop measures for bypass flow reduction with consultation from ANL. Test and analyze the identified measures by the air test facility and the thermal-fluid analysis tools.

3. Task:

6.1   Technical Status Overview (KAERI)

KAERI issued the technical state-of-the-art report on the bypass and cross-flow study.[a] The report reviewed 10 reference papers and summarized the following classified contents: (a) the reactor core fluctuation data for the first identification of the importance of the bypass and cross flow; (b) the cross flow test and evaluation data; (c) the flow test and evaluation data of the seal mechanism to prevent the leakage flow; and (d) the reactor core thermal-fluid analysis and evaluation data. The review results are summarized as discussed below. The reactor core thermal fluid analyses were not included because they are specific for HTTR reactor.

As the first identification of the importance of the bypass and cross flow, Fort St. Vrain experienced the reactor core signal fluctuation events in October 1977. Through a 3-year investigation, it was concluded that the apparent cause of the fluctuations was movements of core components (fuel columns) accompanied by periodic change in bypass flow and cross flow of primary coolant helium. To eliminate fluctuations, 84 region constraint devices (RCDs) were installed in a plane above the top plenum surface. After installation of the RCDs, no change in core performance was noted.

According to the cross-flow test and evaluation data, the prediction of the main coolant flow reduction was determined by the pressure gradient in the bypass gap that drove the cross flow. Based on the cross-flow tests of various interface types (parallel & wedge-shaped), the cross flow loss coefficient factor was obtained.

As the seal mechanism at the bottom core blocks, the seal element with triangular cross section and V-shaped seal seat suggested by JAEA was highly effective in preventing leakage flows as compared with the plate-type seal mechanism. It was learned that most of the leakage flow occurred at the seal element end-gaps. The pressure loss coefficient factor of the seal mechanism could be predicted with the use of the effective flow area of the end-gaps.

6.2   Identification of Bypass Flow Measure (KAERI/SNU)

According to the review of the state of the art, seal elements on the bottom core blocks were the only devices applied for the reduction of bypass flow. Therefore, the seal elements were considered as the first option for the bypass flow reduction in the air test. The conceptual diagram for the seal elements in the air test facility is shown in Figure 6-1. A number of V-shape seal elements will be installed between the bypass gaps on the top surface of the transition blocks.

---

a. State-of-the-art report for the bypass and cross flows in prismatic modular high-temperature gas-cooled reactor core, KAERI/AR-846/2010 (in Korean)
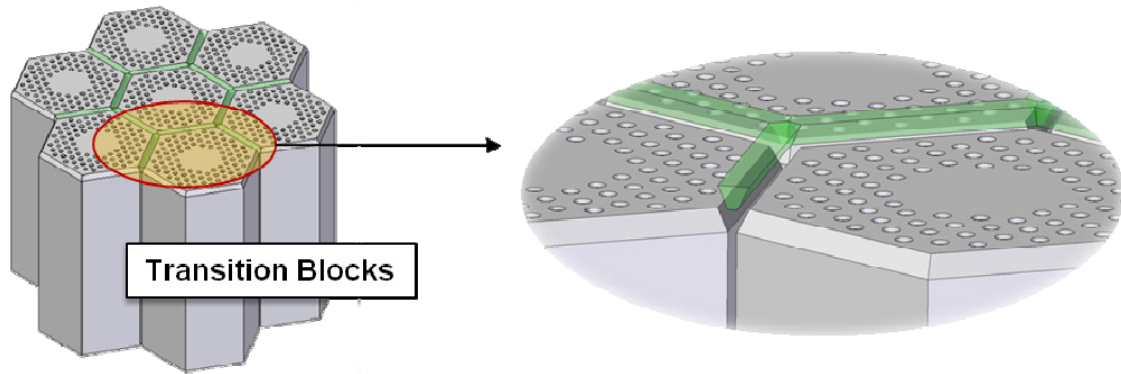
Figure 6-1. Concept for testing the seal elements in the air test facility.

Another measure for the bypass flow reduction is to introduce a staggered arrangement of transition blocks as illustrated in Figure 6-2. The transition blocks are divided into two layers where the blocks are installed in a staggered way to make the top surface of the transition blocks in the second layer block the bypass flow from the first layer.
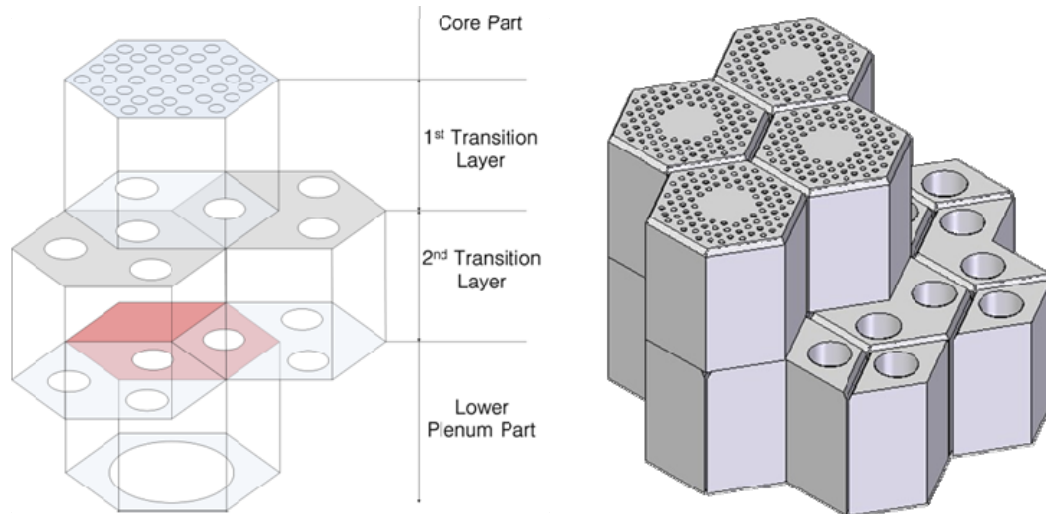
Figure 6-2. Staggered arrangement of the blocks in the transition layer.

From the preliminary analyses of the air test experiment, it was discovered that the presence of the reflector blocks increases the bypass flow. To reduce the bypass flow in the interstitial gaps between the reflector blocks, it is suggested that the configuration of the reflector are modified as shown in Figure 6-3. The side surface of reflector block was changed from a smooth one to a grooved one. The pressure drop coefficient can be increased by increasing the number of grooves or by changing their width and depth.
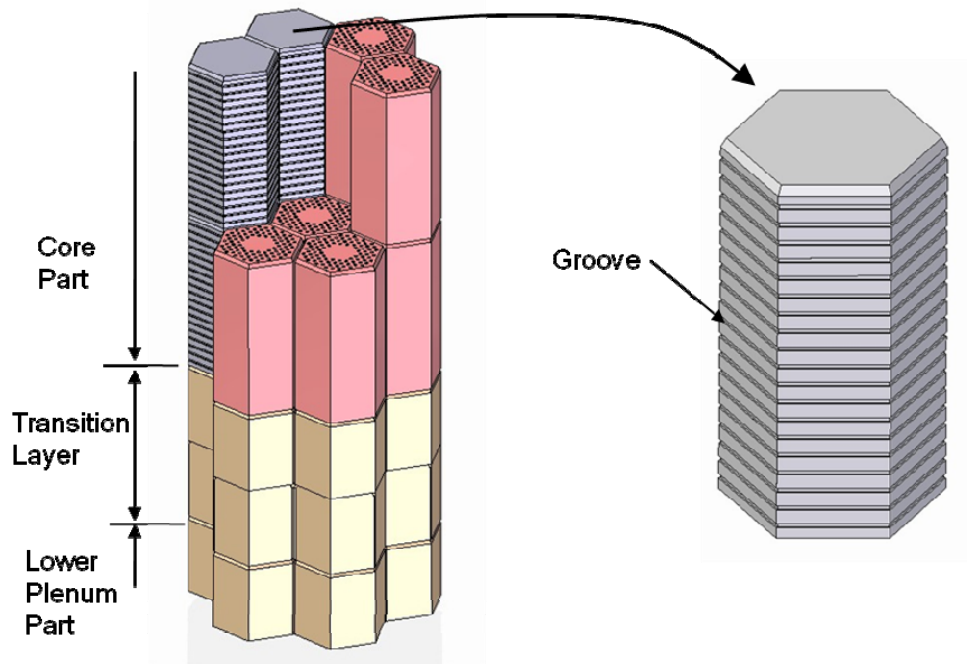
Figure 6-3. Configuration of reflector blocks with grooved side surfaces.

6.3 Design of Bypass Flow Reduction Measures (KAERI/SNU)

6.3.1 Staggered Arrangement of Transitional Blocks

In order to seal the bypass gap exit, a staggered arrangement of transitional blocks was suggested. To implement it into the experiment, the transitional region of test bocks were composed of two layers as shown in Figure 6-4 and Figure 6-5. The upper and lower side of the upper transitional blocks are connected to the fuel block and lower transitional blocks respectively. Thus, the air from the coolant holes in the fuel block is merged in the upper transitional block and it flows to the lower transitional block through three large holes of which diameter is 60 mm.

Figure 6-4. Design of transition block – upper layer.
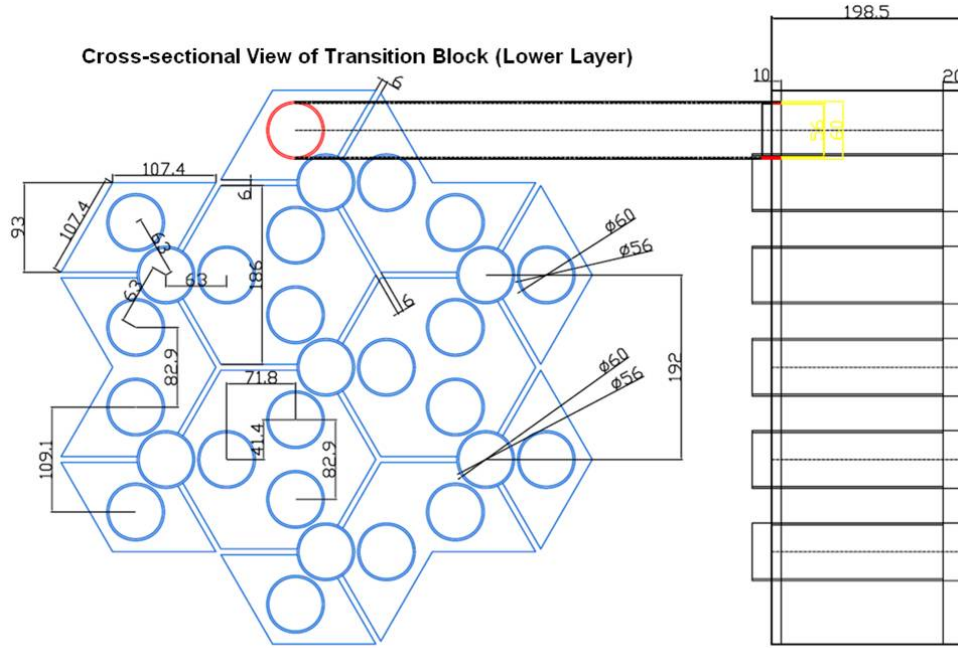
Figure 6-5. Design of transition block—lower layer.

6.3.2   Grooved Surface of Reflector Blocks

Labyrinth seal is one of the mechanical seals widely applied to the engineering field, such as the seal of the pump, the turbine, and so on. By adopting the labyrinth seal concept on the side walls of the reflector block, the flow resistance in the bypass gap adjacent the reflector block will be increased so that the bypass flow can be reduced. Equation 5-1 expresses the experimental correlation for the flow loss factor by the labyrinth seal.
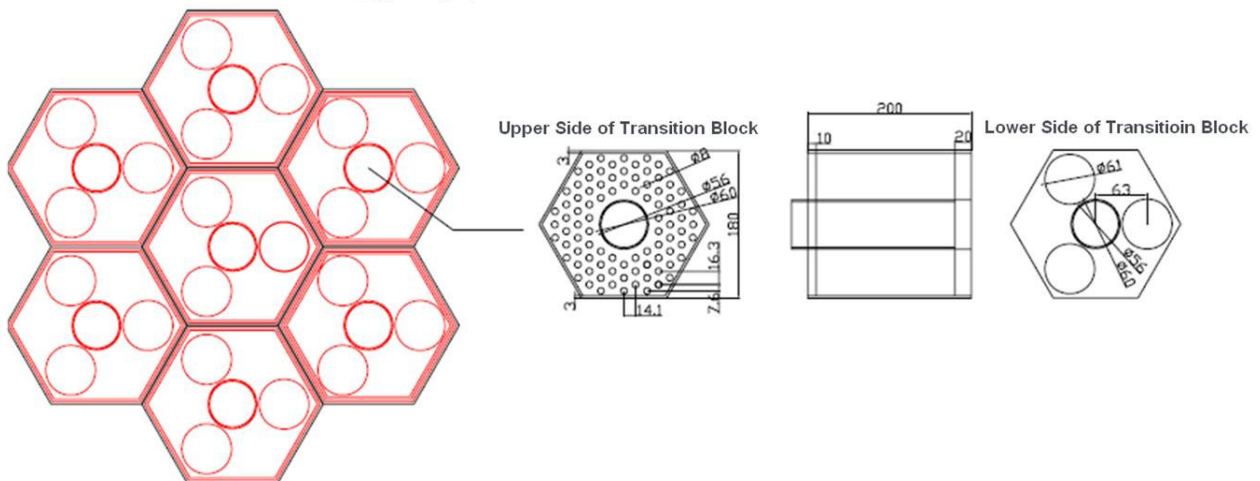
$$K = \frac{\Delta P}{\rho V_0^2 / 2} = 1.5 + z(a_1 + 0.5b_1 + K_{fr})$$

(5-1)

where z is the number of labyrinth cell, K_{fr} is frictional loss coefficient, a_1, b_1 is constant.

A basic geometry of the labyrinth seal was determined based on Eq. 5-1 to maximize the loss factor. After the sensitivity test and optimization for each parameter, the reflector wall structure was determined as shown in Figure 6-6. The rear part of the protrusion of labyrinth cell is designed diagonally because the flow loss coefficient increased with this structure. Parameters for the grooved reflector wall such as width and depth of cell was optimized by the shape optimization algorithm using a surrogate model. Figure 6-7 shows the drawing of the test blocks.

Figure 6-6. Design of grooved reflector wall.

Figure 6-7. Design of test block for the grooved reflector wall method.

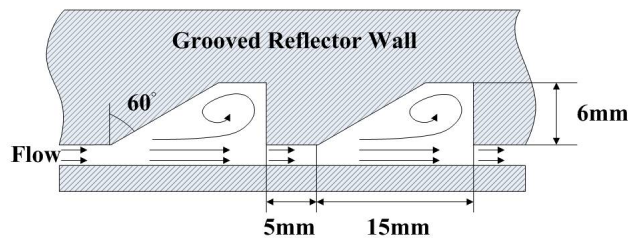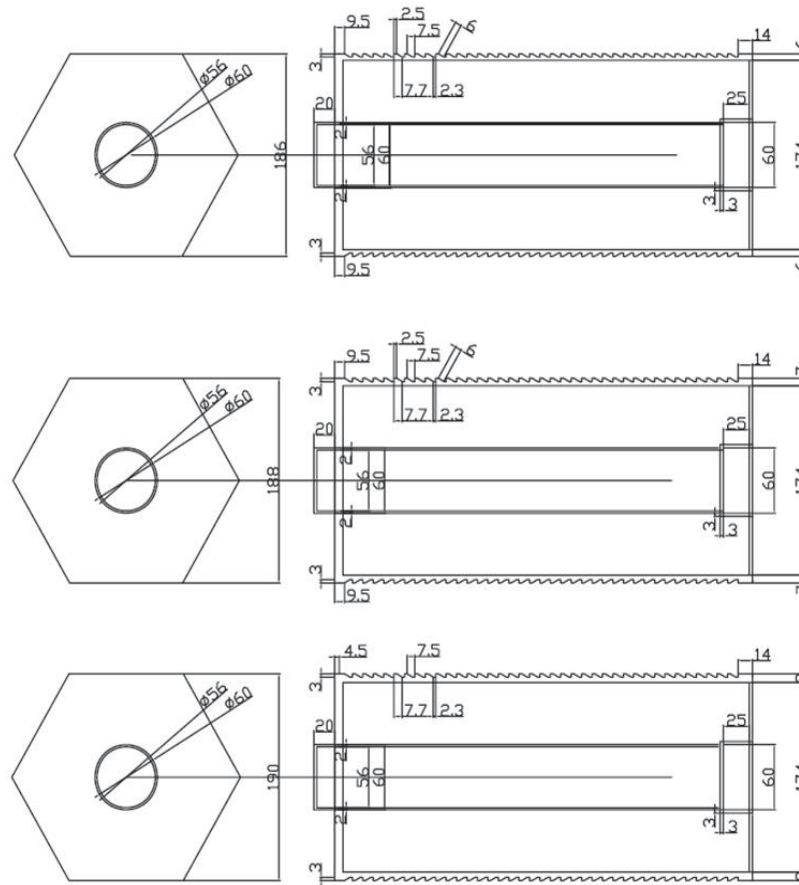## 6.4 Performance Test of Bypass Flow Reduction Measures (KAERI/SNU)

The performance test of bypass flow reduction measures was carried out based on the R2-BG6242-CG2 case. The experimental case for the staggered arrangement of transitional blocks was named STB-R2-BG6242-CG2, and that of the grooved reflector wall test was named GRW-R2-BG6242-CG2.

Table 6-1 and Table 6-2 show the performance test results for the bypass flow reduction measures. Staggered arrangement of transitional blocks increases the flow in the coolant holes significantly. The bypass flow at the exit is reduced to 1.48%, which means that the staggered arrangement of transitional blocks effectively prevents bypass flow at the bypass gap exit. The grooved reflector wall also shows good performance in reducing bypass flow that bypass flow ratio was reduced from 22 to 14% at the exit for the case without the grooved wall. The coolant flow increase at the inlet means that the grooved wall has an influence on the reduction of bypass flow throughout the layers.

Figure 6-8 and Figure 6-9 show the pressure distribution for each case. In STB-R2-BG6242-CG2 case, the stagnant region in the bypass gap occurred behind the middle cross-flow gap (CG2). Sudden pressure drop in the coolant hole occurred every cross-flow gap, meaning that the cross flow headed from the bypass gap to the coolant hole. In the GRW-R2-BG6242-CG2 case, the characteristics of pressure drop were similar to the R2-BG6242-CG2. However, the total amount of the pressure drop increased to approximately 5500 Pa. Since the flow loss adjacent to the grooved reflector wall increased, the total pressure drop also increased.

Table 6-1. Flow distribution of STB-R2-BG6242-CG2 case.
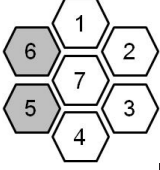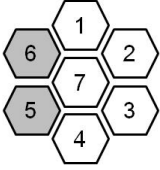
Number of Block Column		Experiment		CFD Analysis	
		Inlet	Exit	Inlet	Exit
	1	0.135637525	0.200463	0.144526	0.211522
	2	0.130762179	0.21208	0.144953	0.21801
	3	0.133762205	0.214636	0.144925	0.216695
	4	0.135305303	0.182115	0.144551	0.21199
	5	–	0.047055	0	0.013046
	6	–	0.046083	0	0.013651
	7	0.14031165	0.166213	0.143466	0.20779
Mass Flow Rate (kg/s)		1.084723071	1.084723	1.1	1.1
Bypass Flow Ratio (%)		37.70033286	1.48217	34.32543	0.66

Table 6-2. Flow Distribution of GRW-R2-BG6242-CG2 Case.

Number of Block Column		w/o grooved wall		w/ grooved wall	
		Inlet	Exit	Inlet	Exit
	1	0.150006	0.176025	0.159041	0.211213
	2	0.148723	0.195093	0.155217	0.216506
	3	0.149214	0.192195	0.158237	0.212149
	4	0.151646	0.191137	0.161084	0.208750
	5	–	–	-	-
	6	–	–	-	-
	7	0.144119	0.192482	0.156176	0.207624
Mass Flow Rate (kg/s)		1.220945	1.220945	1.237695	1.237695
Bypass Flow Ratio (%)		39.08759	22.44269	36.1914	14.66049

Figure 6-8. Pressure distribution of STB-R2-BG6242-CG2 case.

Figure 6-9. Pressure Distribution of GRW-R2-BG6242-CG2 case.

4. Planned activities

   None

5. Issues/concerns

   None

7. PROJECT MILESTONE/DELIVERABLE SUMMARY:

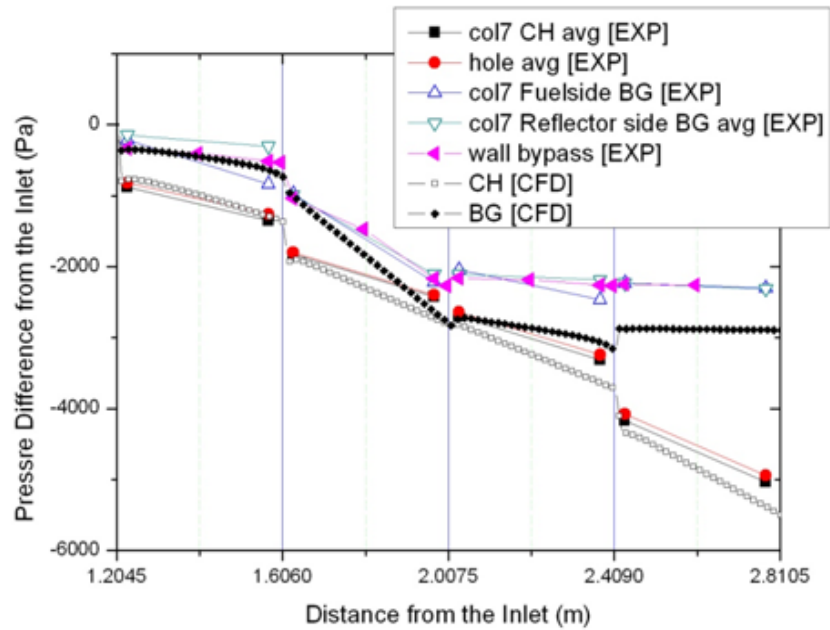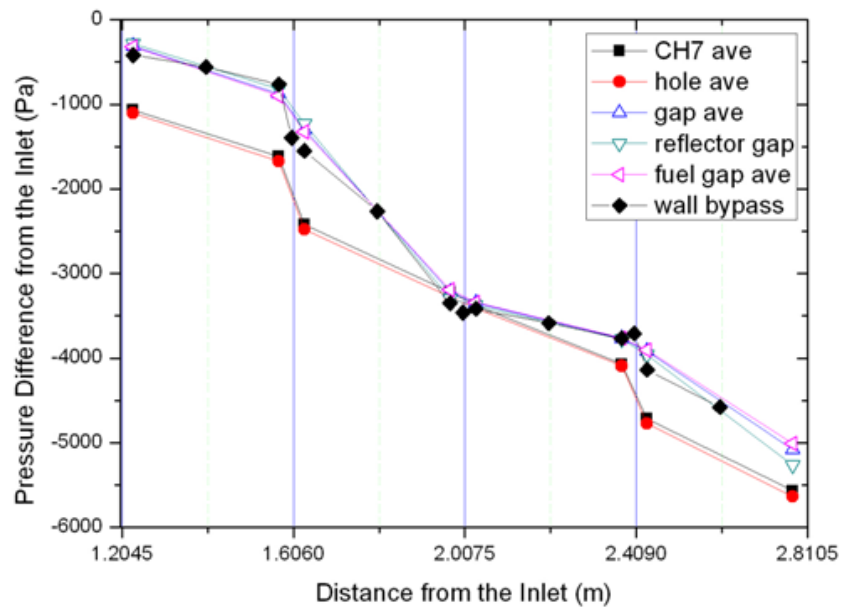| Milestone/Deliverable Description	Planned Completion Date	Actual Completion Date
CFD analyses to assist the development of the models (INL/KAERI/SNU)	09/30/09	09/30/09
Design of MIR test facility (INL)	09/30/09	09/30/09
Design of multiblock air test facility and procurements of components (SNU/KAERI)	08/31/09	08/31/09
Integration of GAS-NET code (ANL)	09/30/09	09/30/09
Determination of experimental conditions and measurement requirements (INL/KAERI/TAMU)	10/31/09	07/10/09
Annual Progress Report (ALL)	09/30/09	09/30/09
Construction of MIR test facility (INL)	03/31/10	12/31/10
Construction of multiblock air test facility (KAERI/SNU)	02/29/10	03/15/10
Construction of a small transparent bypass flow experiment (TAMU)	05/31/10	5/31/10
Development of measurement techniques (KAERI/SNU)	05/31/10	05/31/10
1st stage experimental data (INL/SNU)	07/31/10	09/30/10
1st stage assessment of thermofluid analysis tools (INL/KAERI/ANL)	08/31/10	08/10/10
Identification of countermeasures for bypass flow (KAERI/ANL)	10/30/10	15/10/10
Development of CFD models and comparisons (INL/KAERI/TAMU)	09/30/10	08/30/10
Annual Progress Report (ALL)	09/30/10	10/28/10
Final stage experimental data (INL/SNU/TAMU)	02/29/11	03/15/11
Final stage assessment of thermofluid analysis tools (ALL)	03/31/11	08/30/11
Proposal of models for system analysis tools and their assessment (ALL)	06/30/11	08/15/11
Experimental & analytical assessment of countermeasures (KAERI/SNU)	07/30/11	08/30/11
Final Report (ALL)	01/30/12	01/30/12

Activity Description	Year 1 (FY 2008)				Year 2 (FY 2009)				Year 3 (FY 2010)			
Design and Construction of Experimental Facility	▨	▨	▨	▨	▨							
Experimental conditions and Measurement Requirement/Techniques		▨	▨	▨	▨							
Testing and Interpretation of data					▨	▨	▨	▨				
Validation and Improvement TF analysis Tools					▨	▨	▨	▨	▨	▨		
Integration of System Level Analysis Tools	▨	▨	▨	▨								
Identification of bypass flow measures						▨	▨	▨	▨	▨		
Final Report												▨

8. REFERENCES

1. GA Technologies, Inc., 1992, "Preliminary Safety Information Document for the Standard MHTGR," HTGR-86-024, Rev 13.

2. J. E. Brocklehurst and B. T. Kelly, "Analysis of the Dimensional Changes and Structural Changes in Polycrystalline Graphite under Fast Neutron Irradiation," *Carbon*, Vol. 31, No. 1, pp. 155–178, 1993.

3. G. B. Engle and A. L. Pitner, *High-temperature Irradiation Behavior of Production-Grade Nuclear Graphite*, GA-9973, Gulf General Atomic Inc., 1970.

4. D. K. L. Tsang et al., "Graphite Thermal Expansion Relationship for different temperature ranges," *Carbon*, Vol. 43, 2005, pp. 2902–2906.

5. B. J. Marsden, et al, "Dimensional and Material Property Changes to Irradiated Gilsocarbon Graphite Irradiated between 650 and 750°C," *J. of Nuclear Materials*, Vol. 381, pp. 62–67, 2008.

6. M. H. Kim and H. S. Lim, "Evaluation of the Influence of Bypass Flow Gap Distribution on the core hot spot in a prismatic VHTR core," *Nuclear Engineering and Design*, Vol. 241, No.8, 2011.

7. Y. Hassan to R. Schultz, "Investigation on the Core Bypass Flow in a Very High Temperature Reactor" Figure 2.22, 2010.

8. J. O. Hinze, *Turbulence*, 2nd edition, McGraw-Hill, USA (1975).

9. R. L. Street, G. Z. Watters, and J. K. Vennard, *Elementary Fluid Mechanics*, 7th edition, Wiley, USA (1995).

10. G. Melese and R. Katz, *Thermal and Flow Design of Helium-Cooled Reactors*, American Nuclear Society, La Grange Park, Illinois, USA, 1984.

11. G. C Park, et al, *Fundamental Thermal-Fluid Experiment for Optimum Design of Very High Temperature Reactor*, KARI/CM-1127/2008, 2009.04.

12. I. E. Idelchik, *Handbook of Hydraulic Resistance*, 3rd Edition, Diagrams 7-20 and 7-37.

13. C. K. Jo, et al., "Preconceptual Designs of the 200MWth Prism and Pebble-bed Type VHTR Cores," PHYSOR 2008, Interlaken, Switzerland, Sept. 14–19, 2008.

14. GA Technologies, Inc., *Preliminary Safety Information Document for the Standard MHTGR,* HTGR-86-024, Rev. 13, 1992.

15. Fluent, ANSYS, Inc., 275 Technology Drive Canonsburg, PA 15317, 2010.

16. STAR-CCM+, Version 5.02.009, CD-adapco, 60 Broadhollow Road, Melville, NY 11747, 2010.

17. R. W. Johnson, "Examination of a Proposed Validation Data Set Using CFD Calculations," paper FEDSM2009-78317, Proceedings of FEDSM2009 ASME 2009 Fluids Engineering Summer Meeting August 2–5, Vail, CO, 2009.

18. R. W. Johnson, H. M. McIlroy, R. C. Johnson, and D. P. Christensen, 2010, "Undesirable Flow Behavior in a Proposed Validation Data Set," Paper ICONE18-29474, *Proceedings of the 18th International Conference on Nuclear Engineering (ICONE18), May 17–21, Xi'an, China.*

19. V. C. Patel and M. R. Head, "Some observations on skin friction and velocity profiles in fully developed pipe and channel flows," *J. Fluid Mech.*, Vol. 38, Issue 1, 1969, pp. 181–201.

20. R. W. Johnson, "Pre-test CFD Calculations for a Bypass Flow Standard Problem," paper IMECE2011-65831, *Proceedings of the ASME 2011 International Mechanical Engineering Congress, Denver, Colorado, Nov. 11–17, 2011*.

21. ANSYS ICEM CFD Ver. 11.0, ANSYS, Inc., 275 Technology De Canonsburg, PA 15317, 2007.

22. ANSYS CFX Ver. 13.0, ANSYS, Inc., 275 Technology De Canonsburg, PA 15317, 2010.

23. Lawrence Livermore National Laboratory, *VisIt User's Manual*, UCRL-SM-220449, October 2005.

24. I. E. Idelchik, *Handbook of Hydraulic Resistance*, 3rd edition, CRC Press.

25. V. L. Streeter, *Fluid Mechanics*, McGraw Hill.

26. H. G. Groehn, "Estimate of Cross Flow in High Temperature Gas-Cooled Reactor Fuel Blocks," *Nuclear Technology*, Vol. 56, February 1982.

27. H. Kaburaki, "Leakage Flow Characteristics of Highly-Effective Graphite Seal Mechanism for HTGR Core Support Blocks," *Journal of Nuclear Science and Technology*, Vol. 25, No. 1, pp. 92–99, January 1988.

28. T. Tkizuka and H. Kaburaki, "Research on Cross Flow in VHTR Core, (I) Two-Block Cross Flow Experiments," *Energy Society of Japan*, Vol. 27, No. 4, pp. 347–356, April 1985.

29. R. B. Vilim, *GAS-NET User's Manual*, in preparation, July 2010.

30. C. Y. Jin, S. J. Yoon, Y. J. Cho, G. C. Park, "Multi-Block Experiment for the Bypass Flow in VHTR Core," *American Nuclear Society, Winter Meeting, Washington DC, November 2009*.